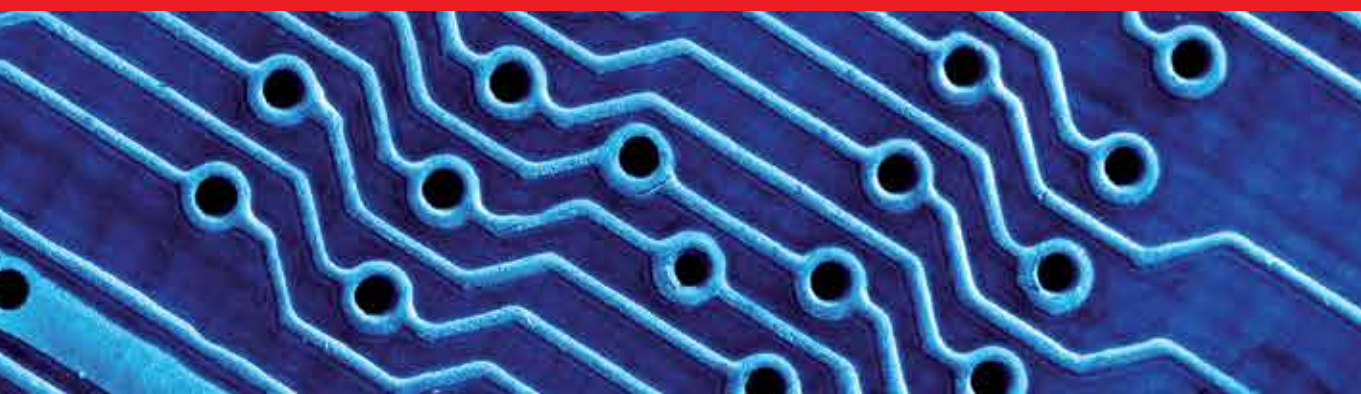# Printed Electronics
Current Trends and Applications

Edited by Ilgu Yun

PRINTED ELECTRONICS – CURRENT TRENDS AND APPLICATIONS

Edited by **Ilgu Yun**

Printed Electronics - Current Trends and Applications
http://dx.doi.org/10.5772/61800
Edited by Ilgu Yun

Contributors

Yuguo Tao, Keisuke Takano, Makoto Nakajima, Masanori Hangyo, Tatsunosuke Matsui, Izabella Krucinska, Wieslawa Urbaniak-Domagala, Ewa Skrzetuska, Miao Yuan, Mengzhi Qin, Xianghua Wang, Jian-Chiun Liou, Xiaojun Guo, Ilgu Yun

Notice

Statements and opinions expressed in the chapters are these of the individual contributors and not necessarily those of the editors or publisher. No responsibility is accepted for the accuracy of information contained in the published chapters. The publisher assumes no responsibility for any damage or injury to persons or property arising out of the use of any materials, instructions, methods or ideas contained in the book.

We are IntechOpen,
the world's leading publisher of
Open Access books
Built by scientists, for scientists

3,700+
Open access books available

116,000+
International authors and editors

119M+
Downloads

151
Countries delivered to

Our authors are among the
Top 1%
most cited scientists

12.2%
Contributors from top 500 universities

Interested in publishing with us?
Contact book.department@intechopen.com

Numbers displayed above are based on latest data collected.
For more information visit www.intechopen.com

Meet the editor

Ilgu Yun received BS degree in electrical engineering from the Yonsei University, Seoul, South Korea, in 1990, and MS and PhD degrees in electrical and computer engineering from the Georgia Institute of Technology, Atlanta, USA, in 1995 and 1997, respectively. He is working as a full-time professor at the Department of Electrical and Electronic Engineering and as an associate dean of the Office of University Planning and Development in Yonsei University. His research interests include material characterization, process monitoring, and modeling and simulations of semiconductor processes, devices, and integrated circuit (IC) modules applied to computer-aided manufacturing of integrated circuits. He is currently a board committee member of the IEIE in Korea and the IEEE senior member since 2003.

Contents

Preface

The intent of this book is to give readers the backgrounds and trends of the printed electronics, including processes, devices, and specific areas of applications covered the terahertz transmission of printed electronics and photonics, the biomedical sensors, and the intelligent textile. As the printed electronics are recently highlighted for low-cost and high-volume manufacturing, the various processing techniques are introduced, and the current development in printed electronics is also presented.

The book consists of seven chapters, including the introductory chapter, which describes the overview of each chapter presenting a specific topic of the printed electronics with the concepts and the progress in current research. Therefore, this book can allow readers to provide the fundamentals of the printed electronics in process or device levels as well as the circuit level implementation scheme for applications. Furthermore, this book can provide a clue for the readers how to solve their current issues for their specific applications. Thus, this book can be used as a reference book for graduate students, engineers, and researchers in the area of the printed electronics.

In presenting this book, I thank all the authors who participated in writing each chapter of the book and followed my positive comments, constructive criticism, and useful suggestions.

I especially extend my sincere thanks to Ms. Andrea Koric, Publishing Process Manager in InTech-Open Access Publisher, for her valuable suggestions and sincere efforts to improve the quality of the book chapters. In addition, I thank the InTech-Open Access Publisher for helping in the type adjustment and for revision of the English for each book chapter.

Finally, I thank my father and mother, Kun-Shik Yun and Hong-Ja Gil, for their influence and inspiration, and my wife, Hyun Jung Cha, and my two adorable sons, Jiho and Joonho Yun, for their sincere care and support.

Ilgu Yun
Professor
School of Electrical and Electronic Engineering
Yonsei University
South Korea

Introductory Chapter: Printed Electronics

Ilgu Yun

Additional information is available at the end of the chapter

1. Motivation

The intent of this book is to provide readers the backgrounds and trends of the printed electronics, including processes, devices, and specific areas of applications covered under the terahertz transmission of printed electronics and photonics, biomedical sensors, and intelligent textile. As the printed electronics are highlighted for low-cost and high-volume manufacturing, various processing techniques are introduced and the current development in printed electronics is also presented.

Currently, the research on the printed electronics is confronted with many issues including material and printing process issues. In addition, for the specific applications with low-cost and high-volume manufacturing, the solutions for the issues may be different depending on the applications.

Therefore, this book can allow readers to provide the fundamentals of the printed electronics in process or device levels as well as the circuit level implementation scheme for applications. Furthermore, this book can provide a clue for the readers on how to solve their current issues for their specific applications.

This book consists of six chapters. Each chapter contains a specific topic of the printed electronics including concepts and progress in current research, which can allow readers to understand the basic information and trend of current research. This can bring readers to initiate new concepts or ideas on the particular research area.

This book can be used as a reference for graduate students, engineers, and researchers in the area of the printed electronics. Some chapters present the fundamental concepts of the proposed topics and some chapters describe the advanced concept of the specific area of the printed electronics.

2. Outline of the chapters

Here, a brief outline of each chapter is introduced:

The chapter entitled "Surface Energy-Modulated Inkjet Printing of Semiconductors" describes newly developed solution processing for the small-molecule organic semiconductors and quantum dots. This chapter deals with process optimization. This chapter will allow readers to understand the technology involved in the fundamentals of surface-energy-controlled inkjet printing processing which will lead to process optimization.

The chapter entitled "Printing of Fine Metal Electrodes for Organic Thin-Film Transistors" presents the fine Ag electrodes fabricated by inkjet printing on PVA polymer substrate and incorporated into all solution processed OTFTs and circuits. It describes from the fundamentals of Organic thin-film transistor (OTFT) to the printing process of metal electrode to OTFT applications.

The chapter entitled "Screen-Printed Front Junction n-Type Silicon Solar Cells" presents the basic information to understand the operating principle of screen-printed front junction n-type silicon solar cells. Also, the detail technology for industrial application is fully described. This chapter will allow readers to address the information of screen-printed process applied for silicon solar cell manufacturing including advanced cell concepts.

The chapter entitled "Efficient Optical Modulation of Terahertz Transmission in Organic and Inorganic Semiconductor Hybrid System for Printed Terahertz (THz) Electronics and Photonics" presents the optical modulation characteristics of thin organic π-conjugated materials on Si substrate using THz time-domain spectroscopy. The study for various laser irradiation conditions for various materials is examined, which can be applied in printed electronics. This will allow readers to provide ideas on how the Thz time-domain spectroscopy can be used for material-dependent characterization.

The chapter entitled "Design and Fabrication of Printed DNA Droplets Arrangement and Detection Inkjet System" describes the implementation of a thermal bubble printhead with simultaneously driving multichannel for DNA droplet arrangement. It proposes a monolithic CMOS/MEMS system with multilevel output voltage electrostatic discharge (ESD) protection system for protecting the inkjet printhead. This chapter will allow readers in the biomedical and electrical engineering areas to understand how the printed electronics can be applied in the bio or biomedical engineering field with full description of hardware implementation by electronics.

The chapter entitled "Development Trends in Electronics Printed Intelligent Textiles Produced with the Use of Printing Techniques on Textile Substrates" presents how the printed electronics can be applied in textile engineering, which will be interesting to the readers involved in research in the field of printed electronics. The hybrid research of the electrical and textile engineering is currently developed for various applications. This chapter shows the recent progress on how to apply the electrically conductive materials for wearable electronics.

Author details

Ilgu Yun

Address all correspondence to: iyun@yonsei.ac.kr

School of Electrical and Electronic Engineering, Yonsei University, Yonsei-ro, Seodaemun-gu, Seoul, South Korea

Surface Energy-Modulated Inkjet Printing of Semiconductors

Xianghua Wang, Miao Yuan and Mengzhi Qin

Additional information is available at the end of the chapter

http://dx.doi.org/10.5772/63425

Abstract

Small-molecule organic semiconductors and quantum dots stabilized with organic surface ligand are drawing attention in future generation solution-processed devices because of their solubility in miscellaneous solvents. Solvent processing and device performance can be effectively modulated with a surface modification layer on the substrate or via ink formulation. Characterization of surface property, specifically the surface energy of the substrate and the liquid, is essentially informative. Investigation on film growth and assembling behavior as well as process optimization via surface energy modulation is successfully achieved.

Keywords: surface energy, inkjet printing, OTFT, interface nucleation, quantum dot

1. Introduction

Inkjet printing is employed as an additive direct writing material growth technology for micron scale pattern formation at a low cost and with the capability of large-scale manufacturing. It permits large-area application without the need of wetting all over the substrate, leading to minimum material consumption. Currently, it is a candidate technology to fabricate electronics of moderate performance and reliability. However, reproducibility of the process over different runs and the reliability of the fabricated devices depend on the ink formulation, the chemical and physical properties of the nozzle plate and the substrate, as well as other process conditions. The wide application of inkjet printing requires a pertinent ink solution designed for each printing step.

Due to the liquid environment, process development for inkjet printing is more complicated than that for material growth within a vacuumed chamber. Current knowledge on the material growth behavior and the mechanism in a solvent environment, especially when the material is deposited as micron scale droplets, is inadequate to satisfy the requirement of rapid process development. Research on typical inkjet-printed electronics and optoelectronics such as organic thin-film transistors (OTFTs) and pixelated color conversion coatings is originally impelled by commercial applications. Investigation of film growth via printed droplets, however, is likely to further unveil the mechanics of solvent processing in the micron and nanometer scales, which can be totally different with large-area film growth.

Concretely, organic semiconductor 6,13-bis(triisopropylsilylethynyl) pentacene (TIPS-PEN) in organic solvents and inorganic quantum dots (QDs) composed of gradient alloyed CdSe/ZnS and surface-stabilizer of PEG-COOH in aqueous solution are inkjet-printed with a Dimatix DMP3000 printer. They are potentially used as the functional layer of OTFTs and as the pixelated color conversion layer on LEDs respectively. It should be noted that the organic component or its molecular structure can be tailored for different surface energy and polarity of the semiconductor [1], thereby rendering its solubility in organic solvents or capability of patterning on a specific substrate. Similarly, the surface of the substrate for printing can be modulated by an organic monolayer with desired surface property to satisfy the requirement of inkjet printing on complex substrates, such as those with 2D patterns or 3D profiles. Fabrication of electronic devices with serial solution processing steps would also become possible [2–4].

A methodology of process development is formulated primarily based on the modulation of surface energy, which is measurable for a liquid droplet or a solid surface [5]. In the first part, also the major part, TIPS-PEN is evaluated as the channel semiconductor of OTFTs. The performance is found to be determined by the interface property as well as the crystallinity. Both can be controlled and optimized via a surface modification layer. In the second part, gradient alloyed CdSe/ZnS QDs are printed as pixelated color conversion element. Here results on an aqueous solution of green color QDs is discussed and referred to as green QDs. In this application, the higher surface energy of aqueous QD solution is favourable to stable jetting. Therefore, positioning accuracy and repeatable printing cycles are developed for accumulated assembling of QDs, while the footprint is well confined within the coffee-rings of the anteriorly printed PVP underlying layers.

2. Small-molecule organic thin-film transistor

Solution processing of soluble conjugated molecules at low cost is a key technology to fabricate OTFTs for "printed electronics". Small-molecule organic semiconductors exhibit high field-effect mobility as a single crystal. The intrinsic field-effect mobility approaches 1 $cm^2V^{-1}s^{-1}$ or even higher than 10 $cm^2V^{-1}s^{-1}$, which is comparable or even superior to those of hydrogenated amorphous silicon (a-Si:H). Compared to polymer semiconductors, small molecule can form low viscosity solutions, which is conducive to stable jetting. Furthermore, the switching

performance of small-molecule OTFTs is usually superior to that of the polymer devices, typically showing a small subthreshold swing (SS). Therefore, much attention is devoted to material processing of small-molecule organic materials in solution forms.

As to the application in OTFTs, we are especially interested in the surface coverage on the substrate, the crystalline morphology, and interface quality. A well-studied small-molecule semiconductor, TIPS-PEN, is used as the semiconducting layer of OTFTs and deposited by inkjet printing. The jetting waveform as shown in **Figure 1** is optimized for stable jetting at frequencies lower than 2 kHz.
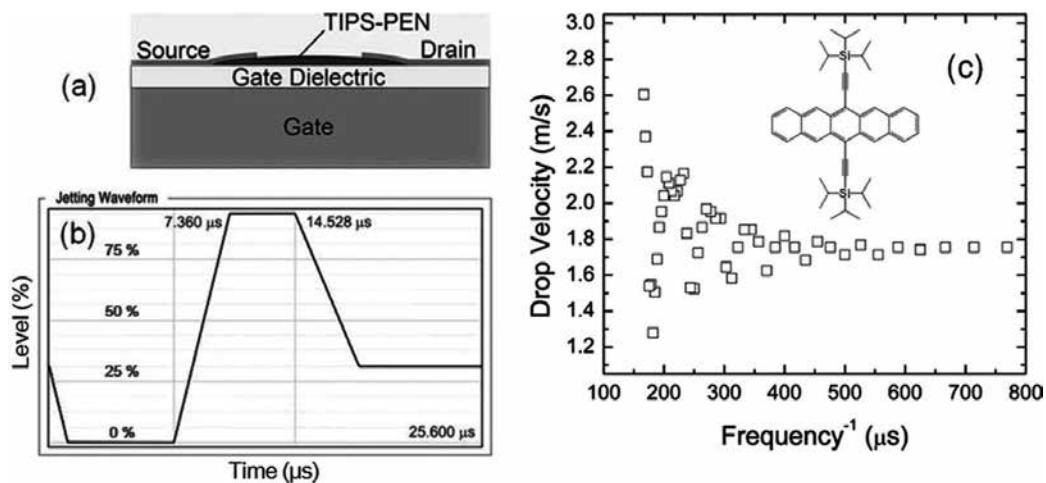
Figure 1. (a) Schematic diagram of a bottom-gate/top-contact OTFT with inkjet printed TIPS-PEN as the channel semi-conductor, (b) The 3-segment jetting waveform, (c) Drop velocity at different jetting frequencies; the inset shows the molecule structure of TIPS-PEN.

2.1. Morphology of single-drop films

A silicon wafer with 300 nm thermal oxide is used as the substrate for inkjet printing. A simple solvent cleaning process is performed on the substrate, which consists of 3 min of ultrasonic cleaning in acetone followed by an ethanol rinse and blow-dry with N_2. In addition to solvent cleaning, spin-coated hexamethyldisilazane (HMDS) is employed to modify the surface property of the substrate. Another surface treatment method uses 10 min of UV-ozone treatment instead of the HMDS coating. Surface tension of liquids and their contact angle with the surface-treated substrate are measured with a type OCA15 video-based automatic contact angle measuring instrument from Data Physics. The surface energy of the substrates as shown in **Figure 2** is calculated from the contact angle measured at a room temperature of 25°C. The surface energy including the dispersion component γ_s^d and the polar component γ_s^p are evaluated based on contact angle measurements of de-ionized water and methylene iodide on these substrates using the harmonic-mean model of Wu [6].
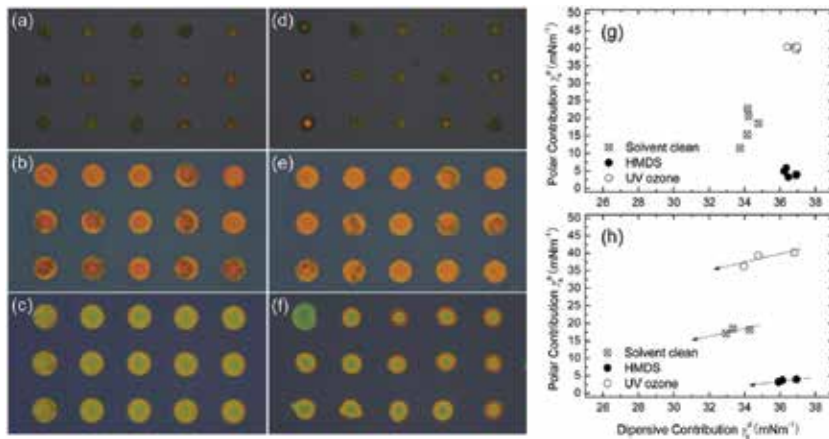
Figure 2. Optical microscopy of arrayed single-drop films on surface treated silica substrate using a 2 wt% TIPS-PEN solution dissolved in *o*-DCB. Drop spacing is 150 μm. (a, d) printed on solvent-cleaned wafer, (b, e) on HMDS-treated wafer, (c, f) on UV-ozone cleaned wafer, after air exposure of 2 hours and 4 hours respectively. (g) Dispersive and polar component of surface energy measured from solvent cleaned wafer and surface-treated substrates. (h) Evolution of surface energy with different air exposure time from 2 to 6 hours.
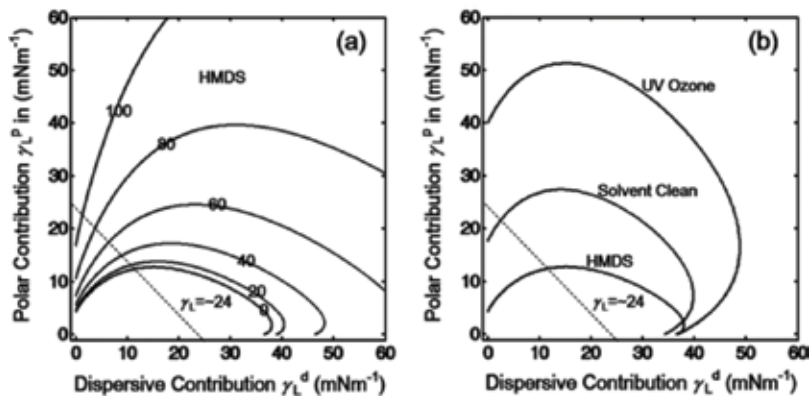
Figure 3. (a) Wetting envelope contour of HMDS-treated substrate plotted for different contact angles (0°–120°); (b) 0° contours for substrates after different surface treatment.

At an ambient temperature of 25°C, the measured surface tension of a 2 wt% and a 1 wt% TIPS-PEN ink solution is 24 mNm^{-1} and 24.4 mNm^{-1} respectively, while that of pure *o*-DCB solvent is 24.8 mNm^{-1}. Contact angle of 2 wt% TIPS-PEN solution on the UV-ozone cleaned sample was 0° at room temperature, while that on an HMDS-treated substrate is about 12°. From the wetting envelope contours shown in **Figure 3**, it is estimated that the solution have a dispersive surface energy of 11.5 mNm^{-1} and the polar component is 12.5 mNm^{-1}, very close to the intersection of the dash line and the 0° contour of the HMDS-treated substrate. Accordingly, the solution completely wets on both of the other two substrates. Obviously, the difference in single-drop film diameter is not determined by the degree of wetting. Further experiment

results in the following sections indicate a positive correlation between single-drop film diameter and the dispersion portion of the substrate's surface energy, which agrees with the results in **Figure 2** and well explains the air exposure effect.

2.2. Elimination of coffee ring staining via surface processing

Apart from film diameter, the thickness profile is evaluated. To achieve a high surface coverage and crystalline film of uniform thickness, the coffee ring phenomena, which is ascribed to faster solvent evaporation from the periphery of the liquid surface, should be avoided. The coffee ring profile can be restrained by slowing down the outward flow induced by solvent evapo-ration, or by inducing a reverse flow with a gradient of surface tension, which can be achieved by a co-solvent system. Another effective approach relies on a facile surface energy modulation of the substrate [7]. The effectiveness arises from the relatively strong interaction between the substrate and the solute molecules, so that the film deposition is initiated by heterogeneous nucleation on the liquid-substrate interface instead of the localized concentration saturation as a result of the higher solvent evaporation rate on the periphery.

Surface silanization with a SAM layer of perfluorodecyltrichlorosilane (FDTS) effectively reduces the surface energy of SiO_2. While the FDTS-SAM treatment reduces the dispersion component as well as the polar component of the surface energy, surface cleaning such as UV-ozone cleaning is found to selectively enhance the polar contribution of surface energy. The combination of a FDTS-SAM treatment and UV-ozone cleaning is proven to be effective in tuning the diameter and profile of the printed single-drop films. For comparison, two sets of surface treatments are performed and the corresponding surface energy is measured. One is solely treated with UV-ozone cleaning and the other is pre-treated with a FDTS-SAM treat-ment. **Figure 4(a)** and **(b)** respectively shows their surface energy in a two-dimensional coordinate space (polar component and dispersive component). Dependence of surface energies, including their two components, on the treatment time of UV-ozone cleaning is plotted in **Figure 4(c)** and **(d)**, respectively, for the two sets of surface treatments.

As shown in **Figure 4(d)**, a prior FDTS-SAM treatment significantly improves the responsivity of surface energy on the treatment time of UV-ozone cleaning. Therefore, the combination of FDTS-SAM treatment and UV-ozone cleaning provide more effective modulation of the surface energy and the film morphology printed thereon. For substrates treated with UV-ozone cleaning alone, the dispersive component and the polar component are of comparable magnitude. For the FDTS-treated sample, the two components deviate from each other after 6 min of UV-ozone cleaning. The strongest contrast is noticed after 8 min of UV-ozone cleaning, when the polarity is maximized to 0.71 for the FDTS-treated sample. Nevertheless, for both sets of substrates, the total surface energy saturates at almost identical level of $75\,mNm^{-1}$. Based on the differential surface energies, a comparative study on inkjet printing is performed on two SiO_2/Si samples, one of which is solely surface-treated with 8 min of UV-ozone cleaning (S1) while the other is grown with a FDTS-SAM followed by the same treatment of 8-min UV-ozone cleaning (S2). It should be noted that these surface treatment cannot achieve a hydro-phobic surface.
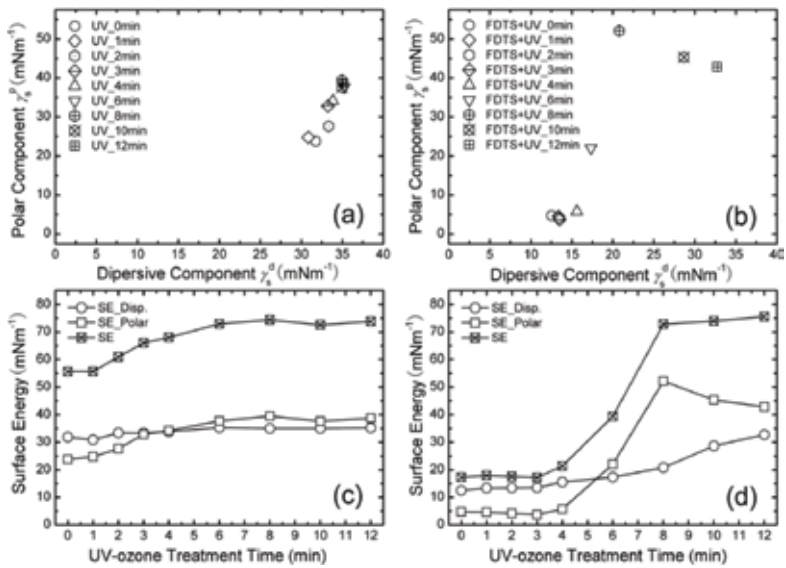
Figure 4. Surface energy of SiO$_2$ plotted in coordinates of polar component versus dispersive component (a, b), and their dependence on the treatment time of UV-ozone cleaning (c, d).
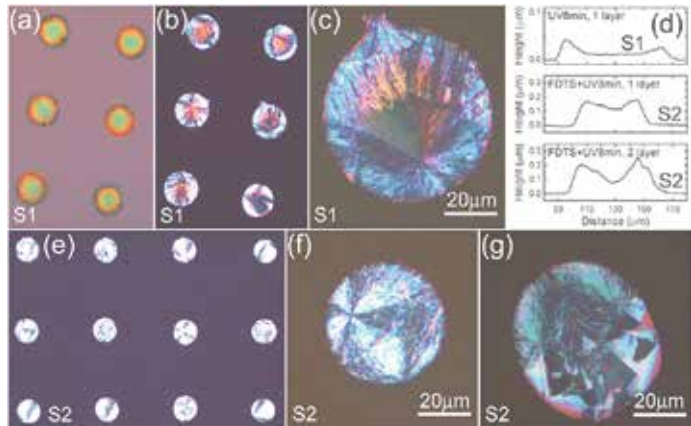
Figure 5. Single-drop films on SiO$_2$ with different surface processing. (a-c) UV-ozone-treated SiO$_2$, (d) PVP-coated substrate, (e, f) FDTS-SAM followed by UV-ozone treatment; (g) microphotograph of a 2-layer isolating dot printed with 2 shots on the same site at a time interval of 10 s.

The polar contribution of surface energy is found to be responsible for the coffee ring profiles, which is usually more serious at increased substrate temperatures or increased number of droplet impacts at the same site (**Figure 5(d)**). On hydrophobic surfaces, such as a PVP-coated or a PETS-treated substrate, more uniform film thickness is obtained as shown in **Figure 6**. We also note that the coffee ring profile would not appear on these hydrophobic substrates even at elevated substrate temperatures.
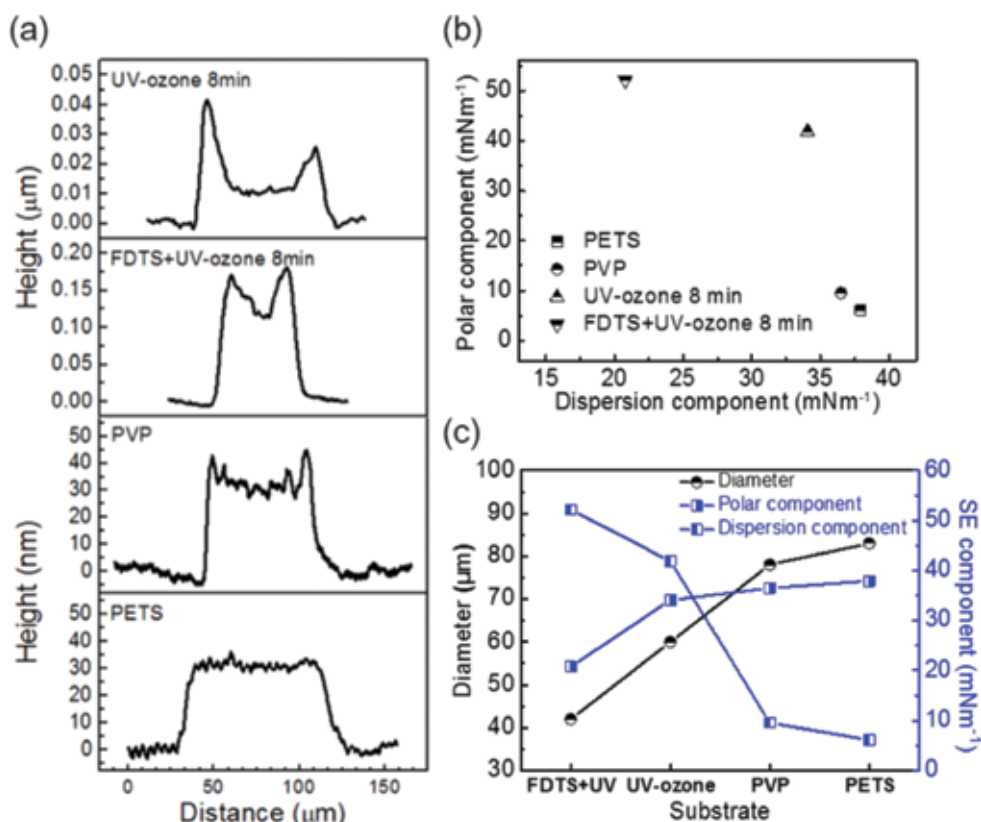
Figure 6. Modulation on thickness profile of a single-drop film via surface processing. The film is printed via *o*-DCB.

2.3. Process optimization for top-contact OTFTs

Fabrication of the field-effect transistor starts with an n-type Si wafer as the common gate material, and a 300 nm thermal oxide is employed as the gate insulator (capacitance =10.8 nFcm^{-2}), whose surface property is considered to be a critical factor that controls the morphology of the printed semiconductor. Instead of pursuing a high resolution patterning, printing of the semiconductor is performed at relatively low resolution, while finer electrode pattern is defined with standard photolithography. Of course, the fabrication of metal line and source-drain electrodes can as well be directly patterned with inkjet printing [8]. In this chapter, the source-drain electrodes are grown by thermal evaporation and patterned via a lift-off process. According to the growth sequence of the semiconductor versus the source-drain contacts, the device architecture is referred to as bottom-gate-top-contact and bottom-gate-bottom-contact respectively. Large-area TIPS-PEN films in the form of single-line or overlapping multiple-line film are employed for OTFT devices.

Single-line films were printed with a drop spacing (DS) of 20 μm. **Figure 7(a)** shows the microphotographs of the single-line film printed on S1 (left) and S2 (right) respectively. Films

of broader width have been printed as well. The inset diagram shows the digital pattern, defined by DS and line spacing (LS) for the printing of broad-width films. The upper diagram of **Figure 7(b)** shows the cross-section profile of the single-line films (intersected by a plane normal to the y-direction), showing a concave profile in the middle due to coffee-ring effect. The lower diagram shows the cross-section profile across a wider line printed with two runs along the y-direction shifted by an LS of 160 μm in the x-direction, which is obviously unsymmetrical, being thicker on one side than the other.
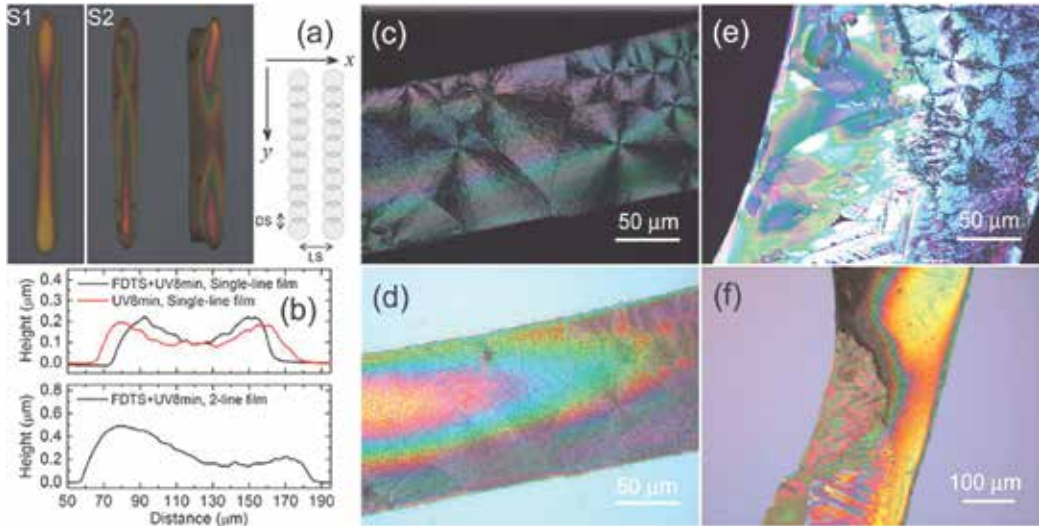
Figure 7. Microphotographs and cross-section profiles of single-line, overlapping 2-line, and multiple-line films of TIPS-PEN printed on SiO$_2$. (a) Image taken with the fiducial camera of the printer (left: single-line film on S1; right: single-line and 2-line films on S2.) The inset diagram shows the printing parameters, DS and LS, as defined for the pattern. (b) Profiles of the single-line films and the 2-line film as shown in (a). Cross-polarized (c, e) and unpolarized (d, f) microphotographs of the films printed on the SiO$_2$ that is surface modified with a FDTS-SAM treatment followed by 8 min (c, d) and 10 min (e, f) of UV-ozone cleaning respectively. Films in (c, d) and (e, f) are printed with 2 and 4 overlapping lines respectively.

The substrate for OTFT fabrication is fluorinated with FDTS followed by 8 min of UV-ozone cleaning. A single nozzle is used for the printing of single-line films or large-area films with overlapping-drop assignment. The print head performs a forward single-trip movement along the y-direction printing a single line with a specified DS that is smaller than the single-drop diameter. At the ending of the forward trip, the print head stops jetting and returns to its starting position on standby or move a step distance along the x-direction according to the specified LS. Films of broader widths were printed by repeating the round trip shifted by an LS smaller than the single-line width. OTFT arrays are printed using varied DS and LS, and optimization on these parameters can contribute to better device performance. As shown in **Figure 8**, the result suggests a critical dependence of field-effect mobility with film thickness and an optimal LS/DS ratio can enhance current on/off ratio of the OTFT by a factor of 10.
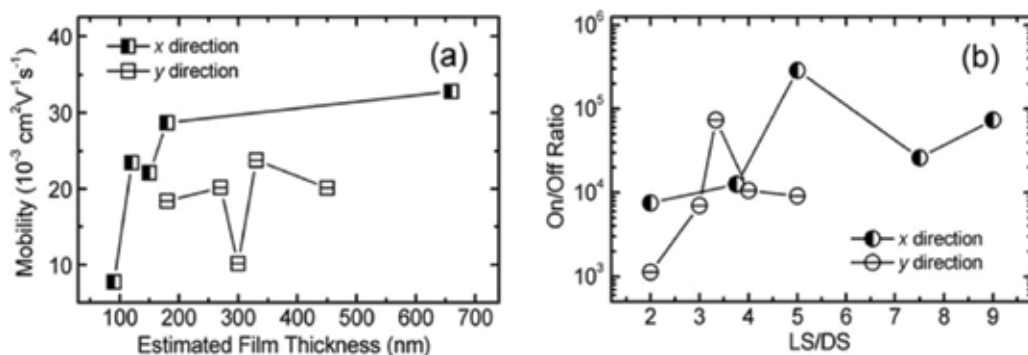
Figure 8. Saturated field-effect mobility of inkjet-printed TIPS-PEN via an *o*-DCB solution on SiO$_2$ substrates treated with FDTS-SAM and 10 min UV-ozone Cleaning. (a) Dependence of mobility along *x*- and *y*-direction on film thickness; (b) Dependence of on/off ratio for field-effect charge transport along *x*- and *y*-direction on the ratio of LS/DS.
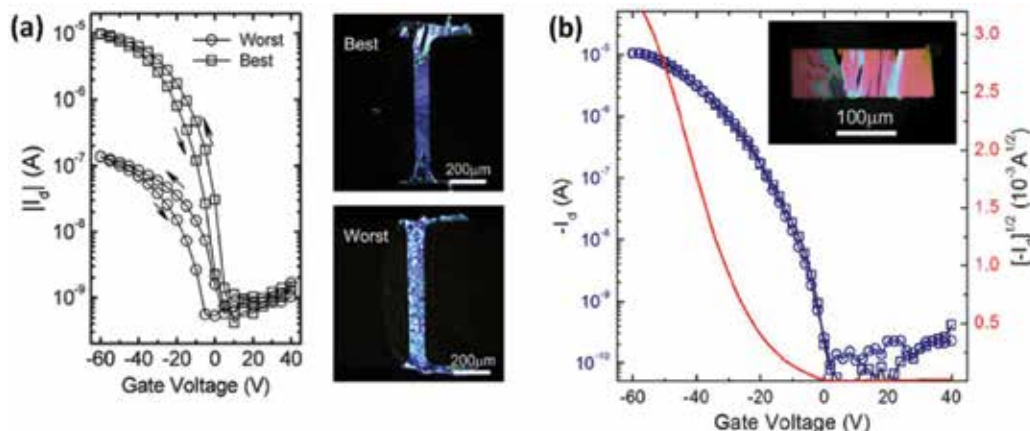
Figure 9. (a) Transfer curves under cycle-swept V$_g$ and the cross-polarized microscopy of the best and the worst device within the same line of the printed OTFT arrays on PVP/SiO$_2$ substrate, both devices are printed via *o*-DCB; (b) Transfer curves under cycle-swept V$_g$ of the highest performance device printed via tetralin, with the accumulation curve shown in open squares and depletion curve in open circles, Inset: the cross-polarized microphotograph of the OTFT.

The effect of using a hydrophobic dielectric surface is also investigated. By spin-coating a second dielectric layer of PVP on the SiO$_2$ as the dual layer gate dielectric, the field-effect mobility can reach 0.1 cm^{2}V^{-1}s^{-1}, but the average mobility is not as high due to the lower performance of devices in the first few columns. Apparently, the difference has been caused by the contrastive film morphology as shown in **Figure 9(a)**. Dissolution test indicates a poor compatibility of the cartridge material with *o*-DCB, which would lead to inferior device performance after a process idle. This is a serious problem in developing high performance devices. Milder solvent such as toluene, anisole, xylene, and tetralin are potential candidates as the solvent. Of these, tetralin is more promising for inkjet printing via tiny droplets because

of its high boiling point that favours self-organization of the semiconductor molecules as crystalline films.
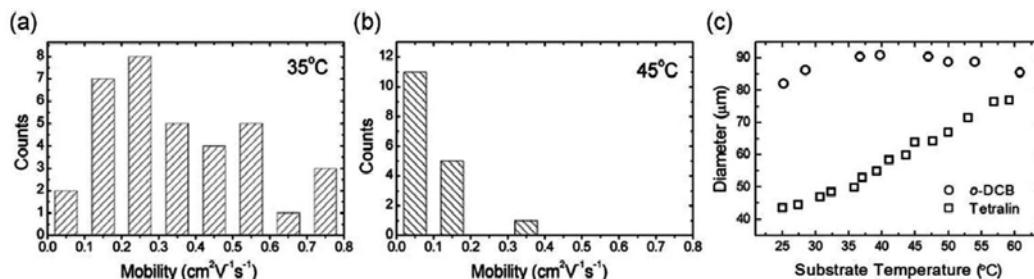
Figure 10. Mobility distribution of 54 TIPS-PEN OTFTs fabricated on PVP/SiO$_2$ substrate with the semiconductor inkjet printed via a 2 wt. % solution in tetralin. Inkjet printing was conducted with the substrate temperature maintained at 45°C (18 devices) or 35°C (36 devices); Diameters of single-drop films printed via the single-solvent solution of o-DCB or tetralin on PVP-coated substrate with increasing substrate temperature.

The multi-line film of TIPS-PEN printed via tetralin on a PVP/SiO$_2$ substrate is polycrystalline with domains in the shape of wide strips (20–100 μm in width) when printed at a substrate temperature of 35°C. The crystal growth direction runs parallel with the y-direction of the printed pattern, therefore, top-contact/bottom-gate OTFT architecture is fabricated with the channel perpendicular to the y-direction of the printed film. Devices printed at a lower substrate temperature of 35°C are generally superior to those printed at a higher temperature of 45°C. The average mobility of devices printed at 35°C is enhanced by one order of magnitude to a value of 0.36 cm^{2}V^{-1}s^{-1} compared with those printed with the o-DCB ink, while the maximum mobility reaches 0.78 cm^{2}V^{-1}s^{-1}, which is about a 7-fold increase. The threshold voltage is -21 V as estimated from the transfer curve in **Figure 9(b)**. Mobility distribution of these OTFTs is shown in **Figure 10**. OTFTs printed at 35°C outperform those printed at 45°C owing to the larger film thickness. Also shown in **Figure 10(c)**, the increasing diameter of the single-drop film printed via tetralin indicates a decreasing film thickness with increasing substrate temperature. Among the 36 devices printed at 35°C, 35 devices exhibit typical OTFT characteristics with approximately 95% of the devices falls within the range of 0.1–0.8 cm^{2}V^{-1}s^{-1}. Compared to devices printed with an o-DCB ink, the tremendous improvement in mobility as well as the more uniform device performance is at least partially ascribed to the tetralin solvent that possesses a higher surface energy than o-DCB, providing a wider process window for the tuning of single-drop film diameter and film thickness.

Film coverage of TIPS-PEN films inkjet-printed for top-contact OTFTs is characterized with AFMs as shown in **Figure 11**. Almost 100% material coverage within the domains was observed for samples printed with the 2 wt% tetralin solution on the PVP/SiO$_2$ substrate. When a 2 wt % solution using o-DCB as the solvent, the crystal ribbons become narrower in width and are

not fully grown, but the crystal growth direction is well aligned. In contrast, crystal domains are not as well aligned over large areas on an untreated hydrophilic SiO₂ substrate.
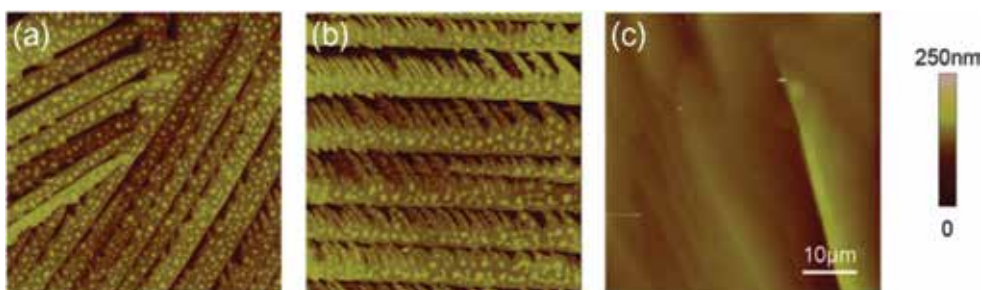

Figure 11. AFM images (50×50 μm²) of large-area TIPS-PEN films printed with overlapping multiple lines on 3 substrates (Left: via *o*-DCB on untreated hydrophilic SiO₂, Middle: via *o*-DCB on PVP/SiO₂, Right: via tetralin on PVP/SiO₂).

2.4. Dielectric surface treatment for bottom-contact OTFTs

The crystallinity of small-molecule semiconductor is generally known to be of paramount importance to its electrical property. Hasegawa et al. developed an antisolvent crystallization inkjet printing technique for the fabrication of single-crystal films on a substrate with predefined patterns. The method is very effective for 2,7-dioctyl[1]benzothieno[3,2-b][1]benzothiophene (C_8-BTBT), achieving average field effect mobility as high as 16.4 cm²V⁻¹s⁻¹. However, the effectiveness is found to be critical on the type of the semiconductor material as to their preferred crystallization behavior. Direct printing of high performance TIPS-PEN OTFTs is still a challenge. The primary obstacle firstly lies in the relatively low field-effect mobility of bottom-contact devices, which is still much smaller than 1 cm²V⁻¹s⁻¹; and secondly, the relatively large subthreshold slope, typically larger than 2 V per decade. The gap can be explained by the inferior crystalline morphology and interface quality. Organic single-crystal transistors can be directly printed on a surface-energy patterned substrate using a co-solvent ink that refrains coffee-ring deposition [9]. To facilitate single-domain crystal growth from a solution, technique of wetting/nonwetting patterning is employed to induce directional lateral crystal growth via the artificial boundary.

In most circumstances, pinning of the three-phase contact line (TCL) initiates the nucleation and crystal growth starts from the circumference and result in polycrystalline film morphology usually with coffee-ring profile. Physical models are proposed to explain the evaporation-induced self organization [10]. However, for the printing of organic semiconductors, it is still difficult to set up an accurate model for the evaporation process based on the contact angle hysteresis measured by a classical method. Because the contact angle, pinning diameter and receding distance are found to be dependent on various factors such as droplet size, solute concentration, and the contact line velocity [11]. It is observed that the receding contact angle determines the TCL behaviors, and can be successfully employed for the assembling of photonic crystals into a dome structure [12]. However, the target of organic semiconductor

film growth is clearly different: laminated structure is desired instead of coffee ring profile or dome structure. It relies to a great extent on the nucleation and its preferred crystal growth behavior to self-organize the solute molecules into the laminated structure.

Printing of bottom-contact OTFTs have to take into account the surface effect of contact electrode in addition to the dielectric surface. In the following, we focus on the latter factor, which is investigated by modifying the surface with a SAM layer of phenethyltrichlorosilane (PETS) or phenyltrichlorosilane (PTS), a spin-coated PVP layer or a UV-ozone treatment. Pentafluorothiophenol (PFTP) was used for the surface treatment of Au electrode. The surfaces as prepared are characterized by contact angle measurement as shown in **Table 1**.

	PTS	PETS	PVP	UV-Ozone	Au	PFTP-Au
CA of H_2O (°)	87.5	85.5	71.3	31.0	91.8	85.4
CA of CH_2I_2 (°)	35.5	37.5	34.4	36.5	23.7	28.6
γ_d (mN·m-1)	38.96	37.94	36.50	37.38	44.20	41.60
γ_p (mN·m-1)	5.17	6.13	9.56	32.47	2.80	5.60
γ (mN·m-1)	44.14	44.07	46.04	69.85	47.00	47.20

Table 1. Contact angles and surface energies of surface-modified dielectrics and Au.

Surface morphologies of the substrates are observed with AFM as shown in **Figure 12**. The surface of the spin-coated PVP and the UV-ozone-treated SiO_2 are comparable in roughness. AFM images indicate that agglomeration of the silane molecules has significantly deteriorated the smoothness of the dielectric surface. The maximum height difference is increased by approximately five times after PETS treatment with an average distance of about 50 nm between neighbouring particulates. Agglomeration of PTS molecules forms even larger particles of around 250 nm in size and dispersed with an average distance larger than 500 nm.
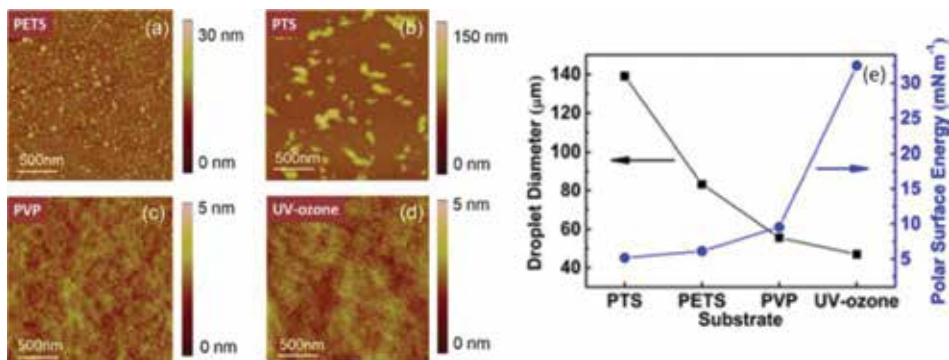

Figure 12. Surface morphology of SiO_2/Si substrates treated by a SAM layer of (a) PETS, (b) PTS, (c) spin-coated PVP, and (d) UV-ozone cleaning; (e) Polar surface energies (solid circles) of SiO2/Si substrates after different surface treatment and the average diameters (solid squares) of the single-drop films printed on them.

TIPS-PEN is printed as a single-line film with a 2 wt% solution in tetralin with the substrate temperature kept at 35°C. Surface morphologies of the single-line films printed at DS of 20 µm and 10 µm are shown in **Figure 13**. Large crystallites are obtained on smooth surfaces, while rougher surfaces as those with PETS- and PTS-treatment clearly result in grainy TIPS-PEN films, which are especially evident for thinner films printed at 20 µm DS. According to the high density of nanocrystalline formed on the SAM-treated surfaces, it is inferred that the film growth on the SAM-treated substrates has been induced by interface nucleation; however, the crystal growth mode seems to be different. Crystal growth on the PETS-treated surface follows a 2D growth mode, while the PTS-treated surface induces a 3D growth mode, which is confirmed by the contrastive height profiles especially that of the thicker films printed at a DS of 10 µm. The increase in grain size for thicker films is most remarkable on the SAM-treated substrates. The out-of-plane X-ray diffraction (XRD) patterns corroborate the dramatic increase in crystallinity for films printed with reduced DS, which is more apparent for the SAM-treated substrates.
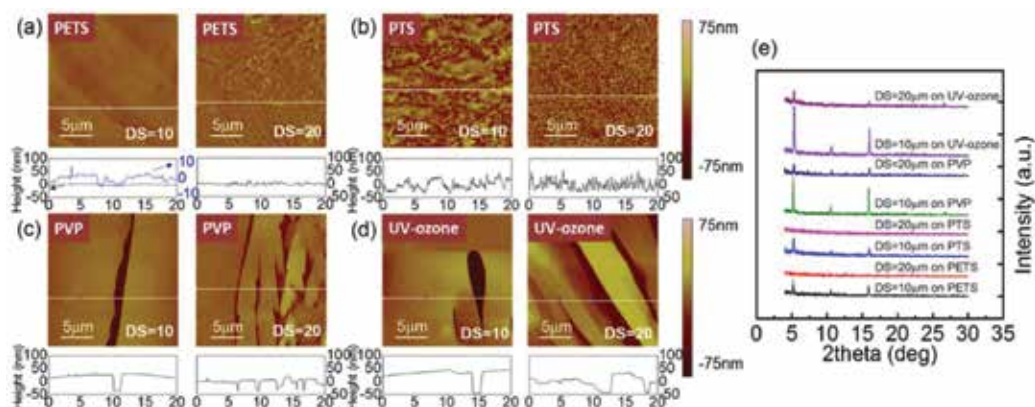
Figure 13. Surface morphologies of single-line films printed at drop spacing of 10 µm and 20 µm on SiO$_2$/Si substrates with different methods of surface treatment (a) PETS, (b) PTS, (c) PVP coating, and (d) UV-ozone cleaning, and (e) out-of-plane XRD patterns of the films with different (00l) peak intensity.

Bottom-contact OTFTs is prepared by printing the TIPS-PEN solution as a single-line film across the source-drain electrodes. As shown in **Figure 14**, the Au electrode induces crystal growth from channel boundary to the centre of the channel, which will inevitably cause a decrease of field-effect mobility. It is clearly seen from the transfer curves in **Figure 15** that the SS is incremental with increasing surface polarity. It is also notable that the OTFT prepared on PETS-treated substrate shows the best performance, with a threshold voltage as small as 1.1 V and a narrow SS of 0.85 V/decade. The extracted transistor parameters for the best performing devices are provided in **Table 2**.
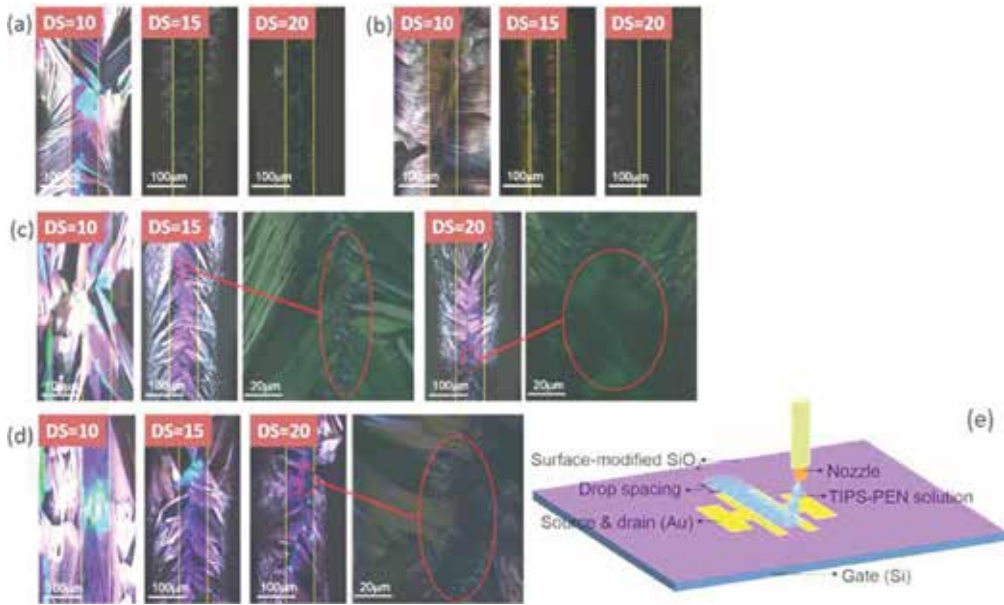
Figure 14. Cross-polarized microphotographs of bottom-contact OTFTs with the single-line films of TIPS-PEN printed across the channels. The substrates have been treated with (a) PETS, (b) PTS, (c) PVP coating, and (d) UV-ozone cleaning.(e) Schematic diagram (not to scale) of bottom-gate/bottom-contact OTFT with inkjet-printed TIPS-PEN as the semiconducting layer in the channel.
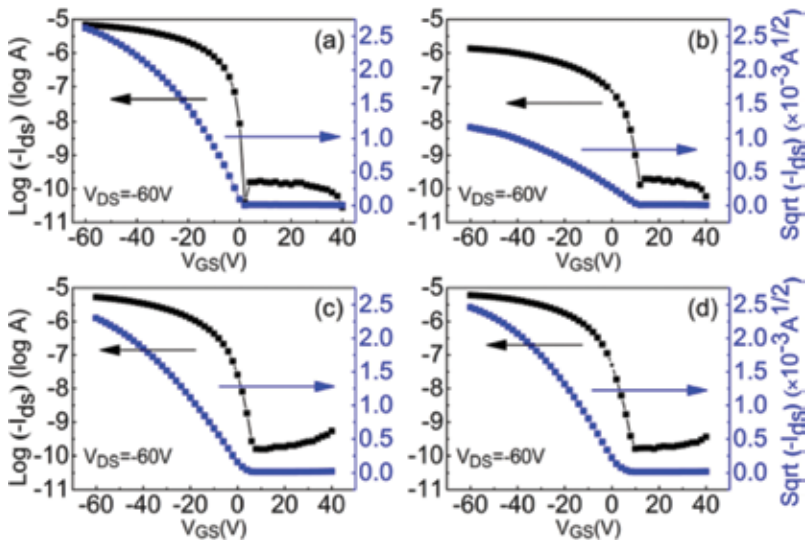
Figure 15. Transfer curves of the best-performing OTFTs. The substrates have been treated with (a) PETS, (b) PTS, (c) PVP coating, and (d) UV-ozone cleaning.

Substrate	DS (μm)	μ (cm^{2}V^{-1}s^{-1})	V$_{TH}$(V)	I$_{on/off}$	SS(Vdec^{-1})
PETS	10	0.140	1.1	2.5×10^5	0.85
	15	0.030	1.0	1.0×10^4	1.88
	20	0.012	2.2	3.5×10^3	1.82
PTS	10	0.007	3.0	2.2×10^3	2.27
	15	0.006	2.8	3.0×10^3	1.68
	20	0.005	1.6	2.4×10^3	2.62
PVP	10	0.062	3.4	4.1×10^4	2.40
	15	0.047	3.5	3.4×10^4	3.36
	20	0.047	2.7	2.4×10^4	2.98
UV-ozone	10	0.058	4.3	3.0×10^4	3.10
	15	0.064	6.7	2.6×10^4	2.10
	20	0.056	5.5	2.8×10^4	1.34

Table 2. Device parameters of the best performing OTFTs.
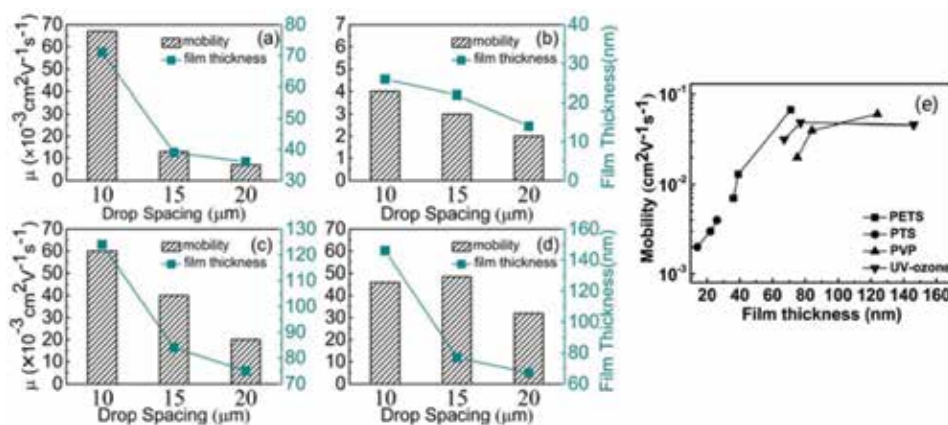
Figure 16. Dependence of film thickness and mobility on drop spacing and correlation between film thickness and field-effect mobility. The substrates have been treated with (a) PETS, (b) PTS, (c) PVP coating, (d) UV-ozone cleaning; (e) Semilogarithmic plot of mobility versus film thickness.

Figure 16 plots the dependence of field-effect mobility and film thickness on the printing parameter of DS. The field-effect mobility generally decreases as the DS is increased, which is ascribed to the decreasing film thickness and crystallinity. An exponentially-decaying trend of saturated mobility on decreasing film thickness is observed for both SAM-treated substrates in the thickness range of approximately sub 100 nm. Although thicker films can be formed on surfaces of higher polarity, the mobility is not improved following the same trend. The device performance is limited by the film morphology of TIPS-PEN showing two features as shown

in **Figure 14(c, d)**. First, the film coverage is not significantly improved with increasing film thickness; second, a crystal boundary in the middle of the channel is formed in the solidified film. Both features are caused by the contact-line nucleation behavior. This problem is not apparent for films printed on the SAM-treated substrates as interface nucleation has played a more significant role during film growth. Film growth via interface nucleation contributes to the formation of a film with higher thickness uniformity and improved crystal coverage, and therefore exhibits higher field-effect mobility.

3. Stacked layers of quantum dots for color conversion

In this part, inkjet printing is developed for the printing of the color conversion element for full-color LED displays. Fluorescent CdSe/ZnS QD is printed via several ink systems. The jetting stability is the key issue to be solved for this application. The stability of the jetting behavior is recorded by printing a dot array, from which the accuracy of drop assignment is evaluated by the extracted coordinates (**Figure 17**). Surface energy of the solvent is a critical factor for stable jetting of the ink suspension. Improvement in jetting stability of the green QDs is achieved using a mixture solvent of water and diluted acetic acid. These experiments again indicate the effectiveness of process development by modulating surface energies of the relevant materials and interfaces, including the substrate, the solvent, and the solute or the dispersed material.

The CdSe/ZnS QDs can be synthesized in organic solvents, however our experiment shows that printing of these organic ink suspension is unstable. The low surface energy of the typical organic solvent for QDs, such as hexane or toluene, substantially wets on the hydrophobic nozzle plate. The single-solvent system of these QDs may not jet at all. The suspension may jet by mixing with anther organic solvent like tetralin, but stable jetting is not achieved. Actually, the nozzle plate has a hydrophobic surface energy designed for stable jetting of aqueous liquids. Here, we focus on processing of aqueous QD suspension.

The mechanical precision of the Dimatix DMP3000 falls within 5 μm. Inkjet printing of aqueous suspension of green QDs achieves a similar level of precision by solvent mixing or dilution. **Figure 18** shows an example of ink formulation and its correlation with jetting stability or precision of printing. QD1 is an aqueous QD suspension purified by centrifugation, also denoted as component A, while other constituents including a 28 wt% acetic acid, glycol, and DI water are denoted as component B, C, and D, respectively. The printing precision of each ink suspension is evaluated by the average deviation, which is calculated by equation (**1**), also shown in **Figure 17**. Deviation of each element single-drop film, r_{ij}, is dependent on the reference grid, which is also optimized by tuning an angle based on the least squares algorithm.

$$\bar{r} = \frac{\sum_{i=1}^{m} \sum_{j=1}^{n} \left| r_{ij} \right|}{m \times n} \tag{1}$$
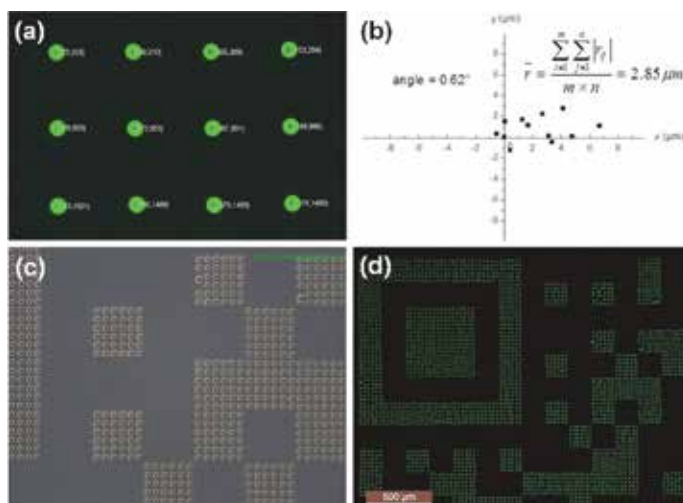
Figure 17. Calculation of positional deviation from target grid for ink jetting of CdSe QDs and demonstration of stable jetting (a) the florescent image of an printed QD single-drop film array with the coordinate extracted and marked as the raw data for calculation, (b) Statistics and calculation of average deviation, (c) an image captured with fiducial camera of the printer after printing a two-dimension code on SiO_2 and (d) fluorescent image of the two-dimension code.
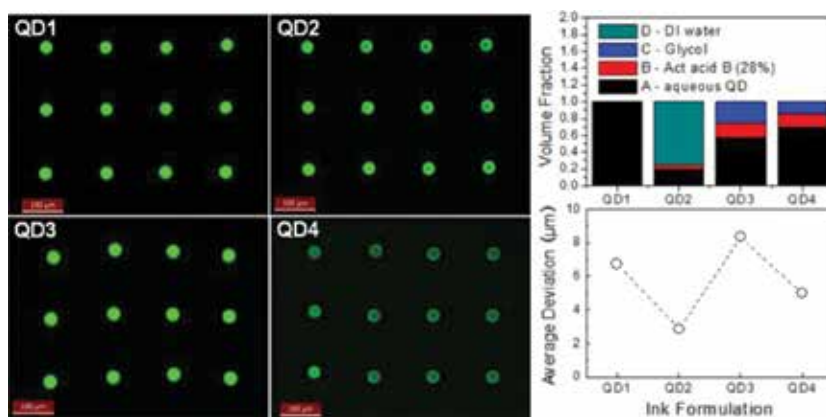
Figure 18. Correlation between ink formulation, color conversion efficiency, and jetting stability.

The aqueous QD suspension with pure component A can be printed with an average deviation of 6.74 μm. It can be remarkably improved to 2.85 μm by dilution with DI water and tuning the PH value with B to around 4. Mixing with ethylene glycol as component C negatively affects the jetting stability, but the high color conversion efficiency of the QDs was at least retained at a low PH value of 3.

Along with positional data for the evaluation of jetting stability, the distribution of the element film diameter in an array also conveys the information about the process stability. The element

QD film diameters can as well be extracted from corresponding fluorescent images for the study of the assembling behavior of QDs on an ITO substrate. Film arrays of green QDs are printed with multiple cycles at the same reference site of the substrate for accumulated assembling of QDs on the grid sites. As shown in **Figure 19**, the diameter of QDs on ITO increases abruptly with the number of printing cycles. Especially, comparing the average diameter obtained from the 3-layer and the 6-layer arrayed films, the doubled printing cycles achieves a 27.7% increase in diameter. The increase factor indicates three-dimensional assembling of QD on ITO. While on the ITO substrates that is patterned with inkjet-printed PVP film arrays, the assembling of QDs on these PVP underlying layer may undergo layer-by-layer assembling as the diameter is almost constant. It should be noted that the inkjet-printed PVP usually have coffee-ring profiles, which can be used as a bank to confine the posterior droplets of QD suspension. But in this experiment, the bank is not wetted owing to the relatively large diameter of PVP and the good positioning accuracy of both materials. Partial wetting of at the bank is observed for the 9-layer QD films printed on the 1-layer PVP, but instead of confinement, the bank guides the assembling of QDs along its interior sidewall. The diameters are calculated according to the area coverage of the fluorescent QDs. Partial wetting at the bank increases the coverage and accordingly increased the calculated film diameter showing an obvious deviation from the baseline data. This can be used for the detection of pattern misalignment.
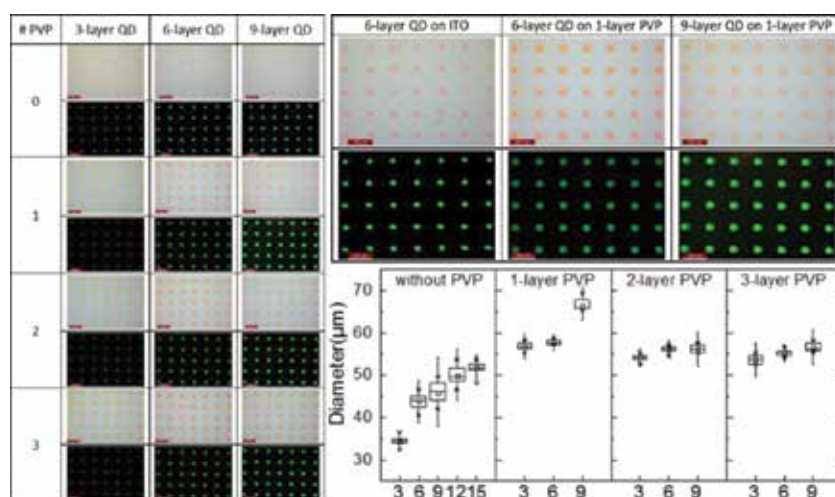

Figure 19. Modulation of the assembling behavior of QDs with inkjet-printed PVP underlying layers.

4. Conclusion

Small-molecule organic semiconductors can be readily processed via inkjet printing and other solution methods with the benefit of reduced cost and pollution. But it is noted that solution-

prepared devices are usually inferior in performance compared to their vacuum-prepared counterpart. Recent investigation on TIPS-PEN indicates a positive correlation between the single-drop film diameter and the dispersive component of the substrate's surface energy, while the coffee-ring staining can be explained by the polarity of surface energy. TIPS-PEN of uniform thickness is printed on the PETS-treated hydrophobic substrate. Process optimization across multiple dimensions is performed and high performance OTFTs are prepared. In addition to modulation of the thickness profile, the nucleation and film growth behavior can be effectively modulated as well. Transition from typical contact-line nucleation to interface nucleation is observed on the PETS-treated substrate, which is attributed to the nanoscale gradient of surface energy. Large-area continuous film with high surface coverage and high performance bottom-contact TIPS-PEN OTFTs can be fabricated on these hydrophobic substrates with nanoscale surface energy gradient. Surface energy also plays an important role in the printing of nanomaterials. Jetting stability, which is critically dependent on various surfaces, is qualitatively evaluated and employed as a key target of optimization for the printing of QDs. It can be employed for ink formulation. High resolution digital patterns are printed using QD material, which can be assembled in 3-dimensions or possibly stacked layer-by-layer depending on the underlying surface.

Author details

Xianghua Wang[1*], Miao Yuan[1,2*] and Mengzhi Qin[1,2*]

*Address all correspondence to: xhwang@hfut.edu.cn, horizon419@126.com and mzqin@foxmail.com

1 Academy of Photoelectric Technology, National Engineering Laboratory of Special Display Technology, National Key Laboratory of Advanced Display Technology, Hefei University of Technology, Hefei, China

2 School of Electronic Science & Applied Physics, Hefei University of Technology, Hefei, China

References

[1] D. Janssen, R. De Palma, S. Verlaak, P. Heremans, and W. Dehaen, "Static solvent contact angle measurements, surface free energy and wettability determination of various self-assembled monolayers on silicon dioxide," *Thin Solid Films*, vol. 515, pp. 1433–1438, 2006.

[2] C. Seungjun, K. Seul Ong, K. Soon-Ki, L. Changhee, and H. Yongtaek, "All-inkjet-printed organic thin-film transistor inverter on flexible plastic substrate," *IEEE Electron Device Letters*, vol. 32, pp. 1134-1136, 2011.

[3] J. Kim, J. Jeong, H. D. Cho, C. Lee, S. O. Kim, S. K. Kwon, *et al.*, "All-solution-processed bottom-gate organic thin-film transistor with improved subthreshold behaviour using functionalized pentacene active layer," *Journal of Physics D-Applied Physics*, vol. 42, pp. 115107-115112, 2009.

[4] A. Arias, S. Ready, R. Lujan, W. Wong, K. Paul, A. Salleo, *et al.*, "All jet-printed polymer thin-film transistor active-matrix backplanes," *Applied Physics Letters*, vol. 85, pp. 3304-3306, 2004.

[5] X. H. Wang, X. F. Xiong, L. Z. Qiu, and G. Q. Lv, "Morphology of inkjet printed 6, 13 bis (tri-isopropylsilylethynyl) pentacene on surface-treated silica," *Journal of Vacuum Science & Technology B*, vol. 30, pp. 021206-021211.

[6] S. Wu, *Polymer interface and adhesion*. New York: CRC, 1982.

[7] X. H. Wang, M. Yuan, X. F. Xiong, M. J. Chen, M. Z. Qin, L. Z. Qiu, *et al.*, "Process optimization for inkjet printing of triisopropylsilylethynyl pentacene with single-solvent solutions," *Thin Solid Films*, vol. 578, pp. 11–19, 2015.

[8] T. Sekitani, Y. Noguchi, U. Zschieschang, H. Klauk, and T. Someya, "Organic transistors manufactured using inkjet technology with subfemtoliter accuracy," *Proceedings of the National Academy of Sciences of the United States of America*, vol. 105, pp. 4976–4980, 2008.

[9] Y. H. Kim, B. Yoo, J. E. Anthony, and S. K. Park, "Controlled deposition of a high-performance small-molecule organic single-crystal transistor array by direct ink-jet printing," *Advanced Materials*, vol. 24, pp. 497-502, 2012.

[10] J. A. Lim, W. H. Lee, D. Kwak, and K. Cho, "Evaporation-induced self-organization of inkjet-printed organic semiconductors on surface-modified dielectrics for high-performance organic transistors," *Langmuir*, vol. 25, pp. 5404–5410, 2009.

[11] J. Fukai, H. Ishizuka, Y. Sakai, M. Kaneda, M. Morita, and A. Takahara, "Effects of droplet size and solute concentration on drying process of polymer solution droplets deposited on homogeneous surfaces," *International Journal of Heat and Mass Transfer*, vol. 49, pp. 3561–3567, 2006.

[12] M. Kuang, J. Wang, B. Bao, F. Li, L. Wang, L. Jiang, *et al.*, "Inkjet printing patterned photonic crystal domes for wide viewing-angle displays by controlling the sliding three phase contact line," *Advanced Optical Materials*, vol. 2, pp. 34–38, 2014.

Printing of Fine Metal Electrodes for Organic Thin-Film Transistors

Xiaojun Guo, Wei Tang, Sujie Chen, Linrun Feng,
Jiaqing Zhao, Yukun Huang, Li Ding and
Haoqian Zhao

Additional information is available at the end of the chapter

http://dx.doi.org/10.5772/64135

Abstract

Attributed to the excellent mechanical flexibility and compatibility with low-cost and high-throughput printing processes, the organic thin-film transistor (OTFT) is a promising technology of choice for a wide range of flexible and large-area electronics applications. Among various printing techniques, the drop-on-demand inkjet printing is one of the most versatile ones to form patterned electrodes with the advantages of mask-less patterning, non-contact, low cost, and scalability to large-area manufacturing. However, the limited positional accuracy of the inkjet printer system and the spreading of the ink droplets on the substrate surface, which is influenced by both the ink properties and the substrate surface energy, make it difficult to obtain fine-line morphologies and define the exact channel length as required, especially for relatively narrow-line and short-channel patterns. This chapter introduces the printing of uniform fine silver electrodes and down scaling of the channel length by controlling ink wetting on polymer substrate. All-solution-processed/printable OTFTs with short channels (<20 μm) are also demonstrated by incorporating fine inkjet-printed silver electrodes into a low-voltage (<3 V) OTFT architecture. This work would provide a commercially competitive manufacturing approach to developing printable low-voltage OTFTs for low-power electronics applications.

Keywords: inkjet printing, metal electrodes, thin-film transistors (OTFTs), all-solution-processed, low voltage

1. Introduction

Following the well-known Moore's Law, metal-oxide-semiconductor field-effect transistor (MOSFET) has been the key semiconductor device platform for silicon (Si) microelectronics since the 1960s [1]. In the past few decades, with the significantly growing demand for display-related information exchange, thin-film transistor (TFT) technology for display backplanes has attracted more and more attention [2]. Similar to MOSFET in Si microelectronics, TFT is considered to be a key component for large-area electronics (display included).

According to different semiconductor materials, TFTs can be mainly divided into amorphous Si (a-Si) TFT [3], metal oxide TFT [4], low-temperature poly-silicon (LTPS) TFT [5] and organic TFT (OTFT) [6]. The liquid crystal display (LCD) has been dominated by a-Si TFT since the 1980s [7]. Lately, metal oxide TFT and LTPS TFT have shown great potential for being used in driving organic light emitting diode (OLED) display [8, 9]. Meanwhile, OTFT is becoming another hot topic in both academy and industry due to its potential applications in low-cost, large-area flexible electronics [10].

Compared with strong covalent bonds in inorganic materials, the van der Waals bonds in organic molecules are much weaker, which brings high degree of intrinsic mechanical flexibility in OTFTs [10]. On the other hand, organic materials have the advantages of good molecule-level design flexibility and bio-degradability. More importantly, low cost and low temperature solution-based processes can be used to fabricate OTFTs, such as spin-coating, blade-coating, slot-die coating, spray coating, bar-coating, ink-jet printing, gravure printing, roll-to-roll printing, and so on. The printing processes make OTFTs very competitive due to the advantages of low energy consumption, high throughput, and good customization. Based on different application requirements, OTFTs can be manufactured on arbitrary substrates including flexible plastic, paper, and fabric over large area.

In the past decades, apart from research activities on OTFTs in a variety of global universities, lots of companies including Plastic Logic, Polyera, SmartKem, NeuDrive, and ISORG have also been established for the commercialization of OTFTs. With the continuous development, the reported device performance of OTFTs has been far beyond that of a-Si TFTs, and even close to metal oxide TFTs.

The attractive features of superior intrinsic mechanical flexibility, low-cost printable processes, and sustainable performance improvement for OTFTs make them suitable for being used in applications of ubiquitous sensors [11], digital/analog circuits [12], radio frequency identification (RFID) tags [13], smart memories [14], flexible display backplanes [15], and wearable devices [16].

2. Basics of OTFTs

2.1. Device architecture

OTFTs consist of five parts including substrate, gate (G) electrode, source and drain (S/D) electrodes, gate insulator (GI), and organic semiconductor (OSC). According to different gate

electrode configurations (top-gate and bottom-gate) and S/D electrodes configurations to OSC (bottom-contact for OSC on the S/D electrodes and top-contact for OSC under S/D electrodes), there are four kinds of architectures for OTFTs as shown in **Figure 1**: (a) bottom-gate bottom-contact (BGBC) structure, (b) bottom-gate top-contact (BGTC) structure, (c) top-gate bottom contact (TGBC) structure, and (d) top-gate top-contact (TGTC) structure. In terms of G configuration, bottom-gate architecture has been widely used because gate electrode and GI are prepared before deposition of the organic solvent-sensitive OSC, eliminating the possible degradation in OTFT performance. With the BG architecture, other additional processes applied onto G electrodes and OGI as well as for via holes fabrication can be employed without damage to the OSC [17]. The advantage of top-gate architecture is the ease to pattern high-resolution S/D electrodes and the GI naturally acts as a passivation layer for protecting the OSC underneath. However, the relatively rough upper surface of the OSC, especially for small molecular materials, usually causes degradation in carrier transporting and reduces the OTFT's mobility [18]. Moreover, in order not to damage the OSC when depositing GI, an orthogonal solvent for GI is usually required, which greatly restricts selections of GI materials. In terms of contact, top-contact devices usually show superior performance than bottom-contact counterparts for certain organic semiconductors, which results from reduced contact resistance between the S/D electrodes and OSC due to the increase in charge injection area [19]. Each of these architectures has particular advantages and disadvantages, either in performance or in fabrication. Therefore, the proper structure should be carefully considered, which depends mainly on the actual situation and application.
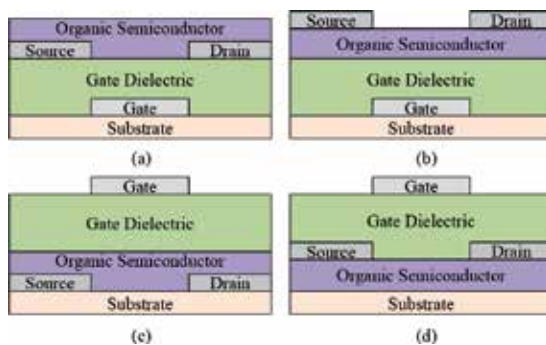
Figure 1. Schematic diagram of the four typical OTFT device structures: (a) bottom-gate bottom-contact, (b) bottom-gate top-contact, (c) top-gate bottom-contact, and (d) top-gate top-contact.

2.2. Work principle

As an active voltage-controlled current source, the conductivity of the channel in the semi-conductor can be modulated by controlling the carrier density in the channel through electric field for a typical field-effect transistor (FET). The representative FETs were metal-oxide-semiconductor field-effect transistors (MOSFETs), where channel conductivity is dependent on the formation of inverse channel. Unlike MOSFETs, semiconductor in OTFTs is a sort of

intrinsic semiconductor without doping, so OTFTs operate in enhancement mode rather than inverse mode. Take p-type BGBC OTFTs as an example, OTFTs can be seen as parallel-plate capacitor. One side of the parallel-plate capacitor is the G electrode and the other side is the semiconductor channel between the S/D electrodes. The density of carriers in the channel is modulated by the voltage of the G electrode (V_{GS}), and the source/drain electrodes inject/collect carrier into/from semiconductor. For p-type semiconductor transporting holes, a negative V_{GS} is needed to generate the corresponding electric field to form the conductive channel. When the V_{GS} hasn't reached the threshold voltage (V_{th}), the drain current (I_D) is usually small enough that can be neglected. It's important to note that the definition of V_{th} in MOSFETs refers to the minimum V_{GS} needed to create an inversion conducting channel between the S/D electrodes. However, there is no inversion in OTFTs, so the definition of V_{th} is not the same as the traditional MOSFETs; however, the V_{th} can also mark the transition of the different regions of operation. When V_{GS} is larger than V_{th}, mobile carriers begin to increase to form the channel layer, as shown in **Figure 2(a)**. If a negative drain source voltage (V_{DS}) is applied, the holes will flow from the source to drain along the channel to generate the I_D in **Figure 2(b)**.
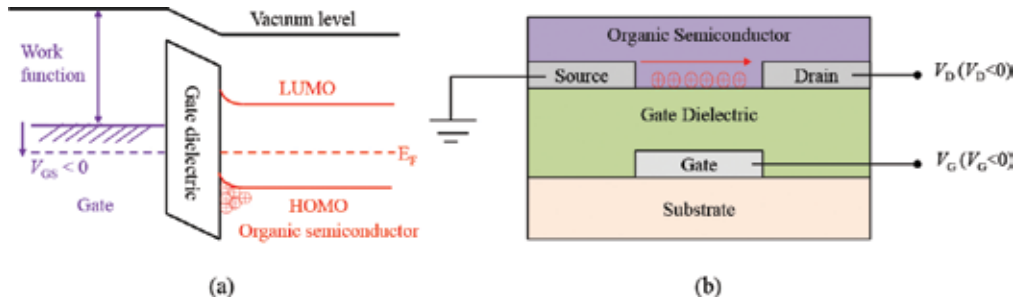
Figure 2. (a) Energy-level diagram of the p-type OTFT with a negative V_{GS} bias. (b) Schematic diagram of working principle for p-type OTFT.

When $|V_{DS}| V_{GS}-V_{th}|$, the transistor is turned on and I_D increases linearly as the increase of V_{DS}, and OTFTs operate in the linear region. When $|V_{DS}| \geq |V_{GS}-V_{th}|$, since the channel is cut off by the strong electric field between S/D, I_D is no longer modulated by the V_{DS} and OTFTs operate in the saturated region. The current-voltage characteristics can be described as following [6]:

For $|V_{DS}| V_{GS}-V_{th}|$ (linear region)

$$I_D = \mu C_i \frac{W}{L}\left(V_{GS} - V_{th} - \frac{V_{DS}}{2}\right)V_{DS} \tag{1}$$

For $|V_{DS}| \geq |V_{GS}-V_{th}|$ (saturated region)

$$I_D = \frac{1}{2} \mu C_i \frac{W}{L} (V_{GS} - V_{th})^2 \tag{2}$$

where μ is effective mobility, C_i is the gate dielectric capacitance per unit area, W is the channel width and L is the channel length.

2.3. Materials and processes

2.3.1. Organic semiconductor (OSC)

OSC materials can be classified into small molecular and polymer OSC materials based on the chemical structures of molecules, while they are also divided into p-type and n-type OSC materials according to the type of charge carriers. Some representative solution-processable OSC materials commonly used are as follows: 1. p-type small molecular, such as TIPS-pentacene, diF-TES-ADT, and C8-BTBT; 2: p-type polymer, such as poly(3-hexylthiophene-2,5-diyl) (P3HT), indacenodithiophene-co-benzothiadiazole (IDTBT), PCDTPT, and poly(2,5-bis(3-alkylthiophen-2-yl)thieno[3,2-b]thiophenes) (PBTTT); 3: n-type small molecular, such as C60, NDI3HU-DTYM2, and 6,13-bis((triisopropylsilyl)ethynyl)-5,7,12,14-tetraazapentacene (TIPS-TAP); and 4: n-type polymer OSC materials, such as P(NDI2OD-T2), NDI-Ph, and NDI-DTYA2.

2.3.2. Gate insulator

Dielectric plays an important role in the operation of OTFTs, which is often used for carrier accumulation at the semiconductor/dielectric interface and prevention of the leakage current. The materials available for the GI can be divided into two kinds: organic polymer dielectrics and inorganic dielectrics. The most commonly used organic polymer dielectrics reported in literature are poly (4-vinylphenol) (PVP), polystyrene (PS), poly(vinyl alcohol) (PVA), polymethylmethacrylate (PMMA), poly(vinyl cinnamate) (PVC), poly(vinylidenefluoride-co-trifluoroethylene) (P(VDF-TrFE-CFE)), and CYTOP. Besides, the traditional vacuum or solution-processed inorganic materials can also be used as the GI for OTFTs, such as SiO_2, Al_2O_3, Si_3N_4, HfO_2, TiO_2, and so on.

2.3.3. Gate and source/drain electrodes

Common conductive metals (such as Au, Ag, Cu, and Al) and polymer (such as PEDOT:PSS) can be used for gate (G) electrode in OTFT. Different from G electrode, source/drain (S/D) electrodes, which contact directly with the OSC and are in charge of carrier injection and collection, have great impacts on the OTFTs' performance. In order to reduce contact resistance with the OSC, the work function of S/D electrodes should match with the highest occupied molecular orbital (HOMO) for p-type OSC or lowest unoccupied molecular orbital (LUMO) for n-type OSC. Hence, the S/D electrodes usually choose high work function Au electrode or self-assembled monolayer modified Ag or Cu electrodes. In addition, two-dimension materials such as graphene are also demonstrated as the S/D electrodes of OTFTs.

2.3.4. Basic processes

OTFTs can be fabricated with vacuum deposition process, such as sputter, thermal evaporation, chemical vapor deposition, plasma-enhanced chemical vapor deposition. However, compared with vacuum processes, low-cost solution processes could effectively decrease the fabrication cost of OTFTs. The common solution processes for OTFTs fabrication are drop-casting and spin-coating methods, which are usually used in the laboratory for OSC deposition for their simple processes [20]. A scalable process method called spray-coating is also developed and mostly applied to many kinds of materials for GI and OSC. With the advantage of direct patterning and drop-on-demand, ink-jet printing has gained a lot of attention in fabrication OSC [21] and electrodes [22]. The dip-coating method is very suitable for OSC formation with well-controlled crystallization direction [23]. Some traditional coating methods such as blade-coating and slot-die coating have also been applied into OTFTs' OSC [24] and GI [25] fabrication. Recently, a "solution shearing" method was proposed by Bao's group in Stanford University [26]. In addition, many other large-area printing/coating methods such as gravure printing [27], roll-to-roll printing [28], bar coating [29], and brush coating [30] are also being used for OTFTs' fabrication.

3. Requirements and technical challenges of printed electrodes

Despite its low-cost and simpleness, printing electrodes for OTFT suffer from several technical issues. Integration of printed electrodes in a multi-layered OTFT structure for circuits would be challenging, since poor interfacial contacts and/or intermixing of the printed electrodes with the semiconductor or dielectric layer during the successive layer deposition processes would adversely affect the device performance. Nevertheless, good control of the cross-sectional profile of the printed electrodes and their geometry shapes is also required.

Normally, the request for high uniformity of overlaying layers and the desire to achieve reliable operation in a multi-layer OTFT lead to uniform profile in the cross-section for lower printed electrodes. Otherwise, the fluctuation of lower electrodes' thickness will interfere with the flatness and uniformity associated with overlaying functional layers, resulting in poor yield over large area. Moreover, the fully printed OTFT devices may also suffer breaking down issue arising from the potential leakage due to relatively higher potential for electrical shorts at the abnormal peak point located on the lower electrodes [31]. As such, the issue of "coffee-ring effect" has received considerable critical attention especially when fabricating OTFTs by utilizing inkjet-printed electrodes. Besides the cross-sectional profile, the parallel source/drain electrode pairs need to be of smooth edges in order to ensure a uniform channel length along the whole channel [32].

On the other hand, to meet the intended requirements of high operation frequency (f_T) of organic integrated logic circuits, there is an urgent need to achieve short channels and small parasitic capacitances. From the organic semiconducting material design point of view, great efforts have been given to develop organic semiconductors for printable OTFTs with mobility similar to or even over amorphous silicon a-Si [33–36], mainly taking performance comparable

to that of conventional silicon electronics, that is, usually 100 kHz at a short channel length less than 10 μm, into consideration [37]. However, it is still far from being able to fabricate high-speed OTFT circuits, which are mainly constrained by the limits of device geometry features when using current printing technology. This is because, in fact, f_T is also dominantly dependent on the device geometry features as shown in the following equation: $f_T \approx u_{eff}(V_{GS} - V_{th})/2\pi L\ (L\ + 2L_c)$, where u_{eff} is the effective carrier mobility, L is the channel length representing the distance between source and drain electrodes, and L_C is the contact length representing the length of overlap between drain-source electrodes and gate electrode [38]. However, the limited positional accuracy of the inkjet printer system and the complicated dynamics of the inks impacting the substrate surface make it difficult to obtain relatively narrow-line and short-channel patterns as required. It is well known that as the distance between two parallel printed electrodes decreases, the failure probability caused by shorting will significantly increase at the same time. Due to the manufacturing limits subject to currently available printing systems, short channel of less than 10 μm and small overlap length that is less than 5 μm are not practically achievable yet. As a consequence, it is now very challenging to mass-print short TFT channel and precisely align the gate electrodes to source/drain electrodes toward manufacturing fully printed OTFT logic circuits with high operating frequencies.

4. Review of printing methods for metal electrodes in OTFTs

4.1. Gravure printing

Gravure printing is an intaglio printing process with a cylinder, which is engraved with wells. When the cylinder rolls over a passing substrate, the ink is carried from the fountain to the substrate, and the excess is wiped using a doctor blade, leaving the ink pattern on the substrate. Recently gravure printing has received great attention to fabricate printable OTFTs due to advantages such as low cost, high throughput, and high speed [39]. Optimization of the printing parameters has been systematically studied to help well understand the process [40–42] At the same time, the optimization of ink formulations for metal ink, dielectric, and semiconductor was conducted [43], enabling clearer understanding of the gravure process . However, to achieve the high performance OTFT devices, the long channel length (~50 to 100 μm) is a persistent limitation due to the different materials' properties and higher quality requirements [44]. Using a combination of rotogravure and ink-jet printing, Vornbrock et al. fabricated highly scaled gravure-printed OTFTs with channel lengths below 20 μm on plastic substrates, offering the highest switching speeds among fully-printed transistors [45]. Kang et al. [27] further developed a novel large-area femtoliter-scale microgravure printing process for high-speed (MHz) printing pBTTT semiconductor and demonstrated highly scaled (10 μm channel length) bottom-gate OTFTs on flexible plastic substrates. Voigt et al. [46] reported the fabrication of polymer OTFTs by nearly-all gravure printing process on plastic substrates with pre-patterned indium tin oxide source and drain contacts with a high speed. Although the scale and resolution are still the limitations of the gravure compared to the lithography-based

technique, the advantages of high speed and high throughout show huge potential in fabrication of low-cost printable OTFTs.

4.2. Flexography printing

Flexographic printing is a type of transfer printing like a modern version of the letter press. In this printing process, ink may be transferred to an anilox roll with textures to get a specific amount of ink, and then picked out from the anilox roll with the reliefs on the elastic printing plate, followed by printing onto various substrate, including plastic, metal, and paper, using an impression cylinder. This high-throughput, low-cost, and high-speed process is potential for the mass-production of flexible OTFT electronic devices [39]. It is normally combined with other print process to realize roll-to-roll OTFT fabrication. Schmidt et al. [44] combined the flexography with gravure and offset processes to achieve the printing OFET using PEDOT:PSS —source/drain electrodes with a yielded channel length of only 10 μm and realized the fully printed flexible audio system [47, 48]. As another practical application example, Pastorelli et al. [28] demonstrated an electrochromic display cell driven by OTFT with flexography-printed silver source/drain electrodes.

4.3. Screen printing

Screen printing is a printing technique originally applied for art work. It uses a mesh and a blade usually moving across the whole area to fill the open mesh with the ink to print pattern on a substrate. The advantage of this process is obvious: the whole technique is simple and it needs no complex equipment. What's more, the printing speed can be very high and there is no limit on the printing area theoretically and the technique is available for nearly all kinds of conventional flat substrates, such as glass, plastic, or even paper. However, a main problem of this technique for fabricating OTFT is that the thickness of the formed electrodes is dependent on the thickness of the mesh and it is very difficult to be reduced to nanometer level. At the same time, the uniformity of the thickness is also hard to be guaranteed. Thus, screen printing is believed to be unsuitable for OTFT fabrication. Interestingly, a recent work by Peng et al. [49] successfully applied screen printing to form 6μm-thick silver gate and source/drain electrodes to construct high-performance OTFTs on a piece of paper and demonstrated OTFT active-matrix LED array.

4.4. Reverse-offset printing

Reverse-offset printing technology as a type of ink-transfer method is also widely used to fabricate printable OTFTs. Compared with other printing methods, it has higher throughput and the minimum line width and space to about 1 μm can be guaranteed [50]. However, this printing method requires the specific ink formulation to prevent from incomplete and excess printing, impeding the widespread use of the reverse-offset printing for OTFT fabrication. By newly developed silver nanoparticle inks, Fukuda et al. demonstrated printed high-performance OTFT devices with wide reverse-offset printed channel length from 0.6 to 100 μm, enabling a systematic investigation of short-channel effects in printed organic TFT devices.

This scalable, high-resolution printing technique will pave a way to fabricate printed circuits with high integration and fast operation over large area.

4.5. Inkjet printing

Drop-on-demand inkjet printing has emerged as a versatile method of increasing interest to manufacture printable OTFTs, due to advantages such as maskless patterning, non-contact, low cost and scalability to large-area manufacturing [51]. There are an increasing number of published studies that utilize inkjet printing to form source/drain and gate electrodes for OTFT fabrication.

To direct-write these conductive electrodes and interconnects, if necessary, a broad spectrum of ink formulations, including polymer PEDOT:PSS and metal nanoparticle inks are available. Recently printing of metal nanoparticles has attracted increasing attention because they can provide robust, highly conductive patterned S/D electrodes with a low annealing temperature, which is particularly important to fabricate devices on flexible plastic substrates. Wu et al. [52] demonstrated the printing of n-butanethiol-functionalized gold (Au) nanoparticles as source/drain electrodes and fabricated high-mobility ($0.15 \text{ cm}^2\text{V}^{-1}\text{s}^{-1}$) poly(didodecylquaterthiophene) (PQT-12) OTFTs with no noticeable contact resistance observed. However, the high cost of gold is against the attributes of this otherwise appealing printing approach for low-cost electronic applications. Not surprisingly, the same group then tried to develop silver nano-particles as potentially much lower cost alternatives. They found improved carboxylic acid-stabilized silver nanoparticles represented ideal printable precursors to highly conductive elements for use in low-cost printed OTFT circuits. The printed silver electrode was of high electrical conductivity similar to the vacuum-deposited silver conductor and enabled fabricated OTFTs with an ohmic contact formation as the energetic mismatch issue of silver electrode with PQT-12 semiconductors was addressed via in situ modification of their interfacial properties [53, 54]. These works demonstrated the ease of printed low-cost silver electrodes as conductive elements for high-performance printed OTFTs.

In most cases, a standard inkjet printer produces a line feature size of above 20 μm corresponding to droplet volumes of tens of picoliter (pL), but offers a limited smallest channel length. To overcome the switching speed limitation and fabricate high-speed OTFT circuits, the channel size defined between printed source/drain electrodes needs to reduce, which has been achieved by several methods. Sirringhaus et al. [55] proposed a hybrid approach to creating short channels that range from several micrometers to hundreds of nm with the help of lithographically patterned hydrophobic polyimide banks, or a hydrophobic self-assembled monolayer (SAM) mesa-like structure by e-beam lithography as an alternative [56], or well-defined polymethyl methacrylate (PMMA) trenches with hydrophilic bottom and hydrophobic walls to contain conducting polymer solutions by combination of nanoimprint lithography and inkjet printing [57].

However, the utilization of various high-resolution lithography tools inevitably leads to more processing complexity and increases the production cost. Therefore, a more cost-effective approach was suggested to create sub-micron channels, most of which were focused upon self-aligning printing (SAP). Generally, the SAP technique is based on two-step printing, that is,

printing of a first conductive electrode line, followed by modifying its surface to more hydrophobic either with plasma treatment or with a self-assembled monolayer (SAM) so that it becomes repulsive to the successively deposited inks, and then printing of a second conductive electrode line along the edge of the first electrode, such that the ink droplets self-aligned off the first conductive electrode, forming a submicron gap of <500 nm in between the two printed electrodes [58–61]. Although the SAP method is simpler and capable of creating shorter channel length than the lithography-based technique, it still requires an undesirable intermediate processing step of surface modification for the firstly deposited electrode. Doggart et al. [62] proposed a facile method for printing source and drain electrodes with very reproducible narrow channel length but free of any intermediate processing steps, which is particularly interesting for a fully complete roll-to-roll fabrication process. This is achieved via engineering ink formulated using organoamine as a stabilizer for silver nanoparticles, allowing a hydrophobic boundary around the first-printed electrodes to be formed during the printing process. Then the ink subsequently printed in the vicinity of the original electrode is repelled and self-aligned by this boundary. Despite the sacrifice of creating a narrow channel only as low as 10 μm, this self-alignment–based printing method allows for printed source/drain arrays with a very narrow distribution of channel length. Moreover, this method is very useful for the development of all printed low-cost OTFT devices.

5. Inkjet-printed fine silver electrodes for OTFTs

In the following research, a metal-organic precursor-type ink (Jet-600C, Hisense Electronics, Kunshan, China) was used for the printed electrodes, which contained 15 wt% silver with viscosity of 12 cps and surface tension of 23.5–24 dyne/cm, and was printed with a piezoelectric inkjet printer (Dimatix, DMP 2831) using a 10 pL cartridge. Cross-linked polymer polyvinyl-alcohol (PVA) coated on glass or PEN plastic foil was used for the printing substrate as it not only presented a flat homogeneous surface, but also served as a good gate dielectric material for OTFT fabrication.

The surface roughness of the PVA was exceptionally small with a root mean square (RMS) roughness of about 0.3 nm measured using a BioScope™ Veeco atomic force microscope (AFM), which was the prerequisite to form controllable and even-printed features [22]. Indeed, an ideal circle shape with a uniform diameter was formed in an array of IJP Ag dots as shown in **Figure 3(a)**. When these isolated droplets overlap each other and merge, a track is then formed. However, the final morphologies of the formed Ag tracks are significantly dependent on drop spacing (Ds) (**Figure 3(b)**). To print Ag tracks with smooth edges, Ds is optimized to be smaller than 50 μm to obtain a straight line with a uniform width. Further decrease of Ds results in increase of the line width of the uniform Ag tracks, meaning the narrowest available Ag track is constrained to about 70 μm wide. The uniform IJP Ag electrodes' surface profiles measured by a surface profiler (KLA-Tencor D-120) present a smooth cross-section without any bulges or coffee rings as shown in **Figure 3(c)**.
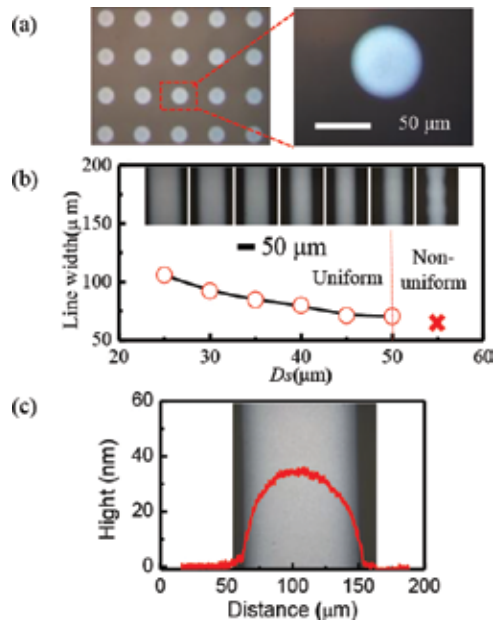
Figure 3. (a) Optical microscopic image of an array of IJP Ag dots. (b) The width of the IJP Ag tracks as a function of the drop spacing (*Ds*) (inset: the top-view optical microscope image of the IJP Ag tracks and their line width). (c) Top-view optical micrograph image of the printed Ag track by using *Ds* of 30 μm with the measured surface profile.

The printed electrode width can be described according to the following equation [63]:

$$W = \sqrt{\frac{2\pi d_0^3}{3D_s\left(\dfrac{\theta}{\sin^2\theta} - \dfrac{\cos\theta}{\sin\theta}\right)}} \tag{3}$$

where d_0 is the ink droplet diameter, *Ds* is drop spacing and θ is the measured contact angle using the printed ink as the test liquid. This equation indicates that for a given printer cartridge with a fixed d_0, to improve the printing feature resolution, theoretically *Ds* and θ are the two parameters which can be optimized. However, it is found that to obtain fine uniform tracks with smooth edges and good conductivity, *Ds* cannot be too small. Then the contact angle turns to be the only alternatively optimized parameter, which is relevant to surface energy of the substrate and also the material ink. An effective method to modulate the surface wettability of the PVA would be using a fluoroalkyl silanes-trichloro(1H,1H,2H,2H-perfluorooctyl)silane (FOTS) self-assembled monolayers (SAMs) [64]. It can be seen that the PVA surface became much less wettable after FOTS modification with the measured water contact angle increasing from 54° to 118° and ink contact angle from 15° to 52°, respectively, as shown in **Figure 4(a)**. The corresponding surface free energy of PVA notably thus reduces from 50.0 mN/m to 10.3 mN/m after modification by FOTS. In this case, the line width of uniform fine Ag tracks could change from about 106 μm for IJP Ag tracks on bare PVA to about 35 μm for those on FOTS-

PVA when an identical D_S of 25 μm is used as shown in **Figure 4(b)**. The reduced spreading behavior of ink droplets on FOTS-PVA mainly attributes to the formation of narrower Ag tracks, demonstrating the feasibility of the developed approach for fabricating narrower fine electrodes (**Figure. 4(c)**).
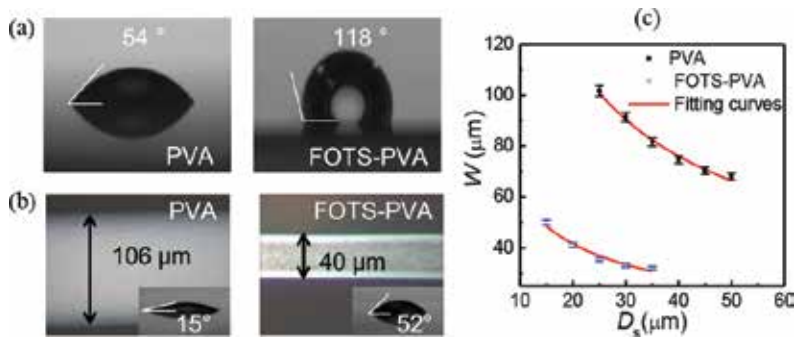

Figure 4. (a) The measured contact angles on bare PVA and FOTS-PVA, respectively. (b) The optical microscopy images of printed Ag lines using a drop spacing (Ds) of 25 μm on PVA and FOTS-PVA, respectively (insets: the measured ink contact angles on the two different surfaces, respectively). (c) The width of the IJP Ag tracks as a function of Ds and the fitting curves.

Then the further challenge would be to form pairs of IJP Ag tracks with small separation for relatively short channels. One reason is due to the limited registration accuracy of common inkjet printer equipment. Another reason is that after the kinetic energy contained in the printed droplet drives it to spread to a certain maximum radius on the substrate, the surface energy of the substrate could finally drive the droplet to recede to a certain radius, which will extend the channel length and also make it difficult to control the channel length [65]. As illustrated in **Figure 5**, the channel length (L) is related to the lateral track spreading width (R) which is dependent of D_S. Thus, to obtain uniform IJP Ag tracks with a short separation, selecting a proper D_S is very crucial.
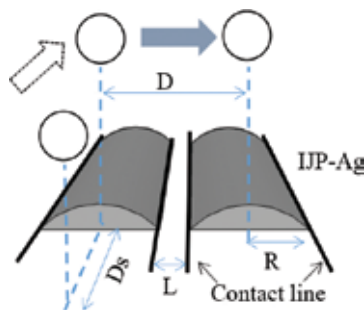

Figure 5. Illustration of the mechanism for inkjet printing uniform electrodes and forming short channels through controlling the ink droplet spreading. Drop spacing (Ds); the track spreading width (R); the moving distance of the printer (D); the channel length (L).

The static contact angle of the Ag ink droplet on the PVA surface is about 11° by the pendant drop method and the receding contact angle approximates zero [22]. These highly hydrophilic properties mean the retraction of the ink droplets is insignificant and the formed tracks are pinned by the contact line (the drop edge) after they monotonously spread to reach the maximum diameter [66, 67]. This surface-energy-limited retracting behavior of inks makes it possible to form the shortest channels at a given moving distance of printer in a controllable manner. By setting a D_s of 45 μm and a printer head moving distance (D) two times of the D_s, formation of parallel S/D electrodes with a separation of about 20 μm was realized with R of about 35 μm as shown in **Figure 6(a)**. To evaluate the process, 100 samples fabricated in arrays were measured with nearly 60% of a gap distance of around 20 μm as shown in **Figure 6(b)**. However, the channel length could be also reduced like the line width by controlling the surface wettability. It has been found that Ag electrodes printed on FOTS-modified PVA are much narrower due to the reduced spreading of inks. Another merit of the formation of narrower Ag tracks on the hydrophobic substrate would be enabling pairs of parallel electrodes to print closer for shorter channel lengths. By setting the printer head moving distance to 50 μm, channels as short as about 15 μm were realized on the FOTS-PVA layer (**Figure 6(c)**), and showed very good yield and uniformity by evaluating 280 test structures (**Figure 6(d)**). Different from utilizing the high-surface-energy-limited "pinning effect" to inhibit retraction after deposition of ink droplets for more wettable surface, the formation of short channels for more unwettable surface instead relies on the low-surface-energy-constrained lateral spreading not only to produce narrower lines but also makes it possible to print two electrodes closer for shorter channels, thus resulting in higher resolution of printing features.
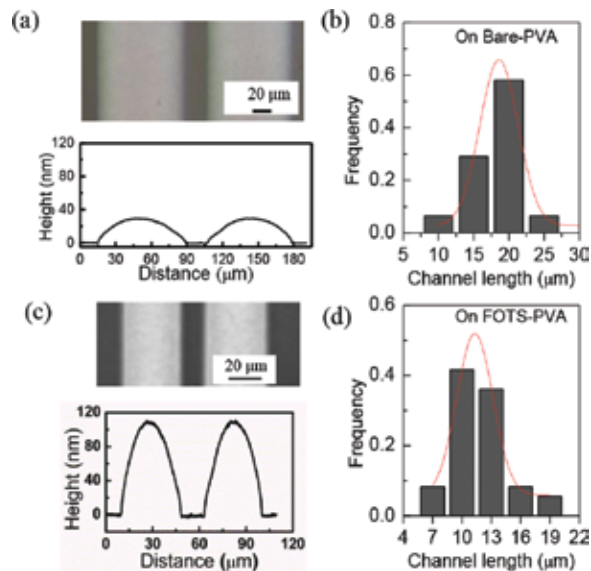

Figure 6. Top-view optical micrograph images of the parallel IJP Ag S/D electrodes and the measured surface profile (a, c) and statistical distributions of the formed channel length (b, d) on PVA and FOTS-PVA substrate, respectively.

Figure 7 shows that the printed Ag electrodes quickly become conductive after 2 min annealing at 150°, a temperature compatible with the PEN plastic substrate. These Ag electrodes have good conductivity calculated with a four-point measurement structure in the range of 5×10^4 S cm^{-1} to 9×10^4 S cm^{-1}. In addition, the electrodes also present a smooth surface (RMS of 1.8 nm) comparable to the thermally evaporated Ag. Combined with uniform morphologies and shapes, these excellent characteristics are attractive for enabling printed electrodes to conduct high current, form good interface, and enable high device performance in practical low-cost OTFT applications.
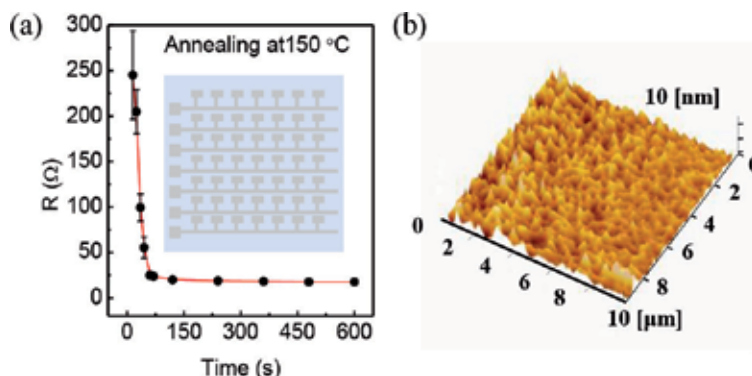

Figure 7. (a) Plot of resistance of printed Ag electrodes versus annealing time at 150° on a hot plate. A four-point measurement structure is also indicated in the inset. (b) Atomic force micrograph (AFM) image of the surface of the inkjet-printed Ag electrodes, with the measured RMS roughness of about 1.8 nm.

The feasibility of printing Ag electrodes enables fabrication of OTFTs by low-cost all-solution or fully-printable processing. Incorporation of fine inkjet-printed silver (IJP Ag) source/drain (S/D) and gate electrodes into recently developed low-voltage OTFT architecture with an ultra-thin high crystalline channel formed by inducing phase separation with the blend of TIPS-pentacene/PS [68], the first demonstration of all-solution-processed low-voltage OTFTs with IJP Ag electrodes was reported [22]. As shown in **Figure 8**, OTFTs present good device performance with a low operation voltage below 2 V, mobility of 0.3 cm^2/V.s, and an ON/OFF current ratio larger than 10^4. It is found that the overlaying dielectric layer was of high quality for low leakage current that was comparable to that in thermally evaporated gate electrode-based OTFTs, thanks to the low flat surface profile of IJP gate electrodes (**Figure 9(a)**). It is also found that the contact resistance extracted according to the transfer line method was about 0.42 MΩ cm, much smaller than that of previously reported BGBC OTFTs, indicating the formation of fine electrode/channel interfaces even with printed Ag electrodes (**Figure 9(b)**). Furthermore, the printed fine Ag electrodes were also incorporated into OTFT logic gate to fabricate all-solution-processed low-voltage inverter on PEN substrate [69]. The demonstrated inverter presents good switching performance with a high dc voltage gain of 67.3 at a supply voltage of about 3 V. It is fair to point out that printing of fine conductive metal electrode and the corresponding low-temperature all-solution-processed device technology is promising for developing low-power fully printable organic-integrated circuits on cheap plastic substrates.
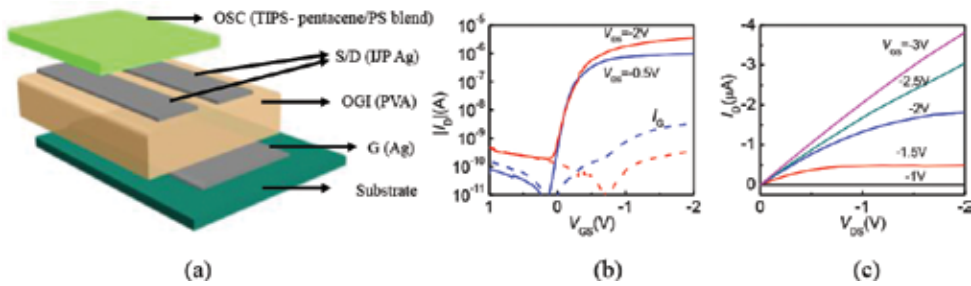
Figure 8. (a) Schematic of the bottom-gate bottom-contact OTFT devices with inkjet-printed silver (IJP Ag) as the gate (G) and source/drain (S/D) electrodes, cross-linked polyvinyl-alcohol (PVA) as the gate dielectric layer, and the blend of TIPS-pentacene/PS is used as the channel. (b) Transfer and (c) output electrical characteristics for the all-solution-processed OTFTs using an IJP Ag gate with a W/L=1200 μm/20 μm [22].

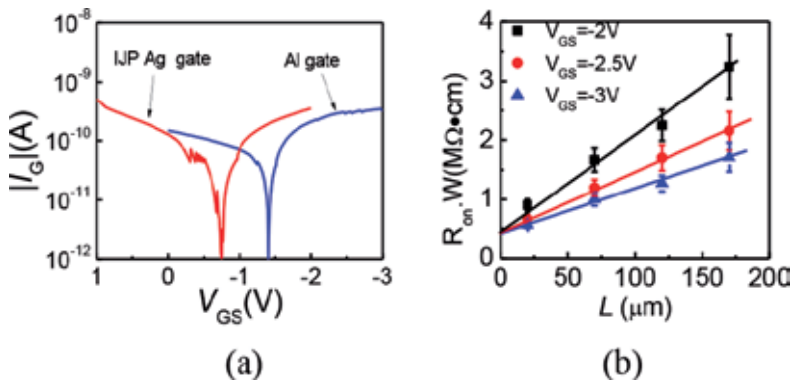**Figure 9.** (a) The measured gate leakage current (I_G) as a function of the gate-to-drain bias (V_{GS}) for the Al gate and IJP Ag gate devices. (b) The transmission line method (TLM) results for OTFTs with IJP Ag S/D electrodes to extract the contact resistance [22].

However, since the polar PVA film contains rich hydroxyl groups and tends easily to absorb water from ambience, the unencapsulated OTFT devices present poorer ambient operational and storage stabilities. Moderate gate leakage is also another issue for low-power OTFT circuit applications. To address these issues, PVA dielectric was then replaced by several commercially available low-k polymers. For example, all-solution-processed low-voltage (< 5 V) OTFT was realized by using 1-micrometer-thick (1.16 μm) commercial SU8 photoresist, which presents an ultra-low gate leakage current of less than 1 pA in the whole operation regime and can also well sustain high-voltage (> 40 V) operation [70]. More importantly, it is found that the small dielectric capacitance provides the fabricated device with better power efficiency than conventional low-voltage OTFTs, which is promising for constructing low-voltage power-efficient logic circuits. Alternatively, printable OTFTs using a hydroxyl groups-free PVC gate dielectric present highly stable electrical properties subject to continuously prolonged bias stressing for hours or being shelved for weeks with the channel being exposed to the ambient air [71]. Nevertheless, with these material advancements, such a fully-printable

low-voltage OTFT technology is believed to practically benefit from inkjet printing of fine metal electrodes.

6. Conclusion

In summary, fine Ag electrodes have been obtained by inkjet printing on PVA polymer substrate and incorporated into all-solution-processed OTFTs and circuits. By controlling the surface wettability of the PVA dielectric layer by coating FOTS SAMs, resolution of the printing feature is improved with S/D electrodes as narrow as about 35 μm and channels as short as 15 μm. The printed Ag electrodes present fine morphology, smooth surface, and high electrical conductivity. Based on these Ag electrodes, all-solution-processed/fully printable low-voltage OTFTs and circuits are further demonstrated and presented excellent device performance, indicating the potential of inkjet-printed metal electrodes for the strict requirements of the S/D and gate electrodes for OTFT fabrication. For further development, highly efficient printable OTFTs and low-cost sensors can be achieved by combination of utilization of more reliable gate dielectric materials. Therefore, the developed printable low-voltage OTFT technology would provide a promising platform for developing general low-cost low-power electronics applications.

Author details

Xiaojun Guo[*], Wei Tang, Sujie Chen, Linrun Feng, Jiaqing Zhao, Yukun Huang, Li Ding and Haoqian Zhao

*Address all correspondence to: x.guo@sjtu.edu.cn

National Engineering Laboratory of TFT-LCD Materials and Technologies, Department of Electronic Engineering, Shanghai Jiao Tong University, Shanghai, China

References

[1] Lundstrom M (2003) Moore's law forever? *Science* 299(5604): 210.

[2] Semenza P (2007) Can anything catch TFT LCDs? *Nat Photonics* 1(5): 267–268.

[3] Wong WS, Ready SE, Lu J-P, Street RA (2003) Hydrogenated amorphous silicon thin-film transistor arrays fabricated by digital lithography. *IEEE Electron Device Lett* 24(9): 577–579.

[4] Nomura K, et al. (2004) Room-temperature fabrication of transparent flexible thin-film transistors using amorphous oxide semiconductors. *Nature* 432(7016): 488–492.

[5]   Lin C-W, et al. (2001) High-performance low-temperature poly-Si TFTs crystallized by excimer laser irradiation with recessed-channel structure. *IEEE Electron Device Lett* 22(6): 269–271.

[6]   Klauk H (2010) Organic thin-film transistors. *Chem Soc Rev* 39(7): 2643–2666.

[7]   Snell A, et al. (1981) Application of amorphous silicon field effect transistors in addressable liquid crystal display panels. *Appl Phys* 24(4): 357–362.

[8]   Arai T, et al. (2011) Highly reliable oxide-semiconductor TFT for AMOLED displays. *J Soc Inf Disp* 19(2): 205–211.

[9]   Gao X, Lin L, Liu Y, Huang X (2015) LTPS TFT process on polyimide substrate for flexible AMOLED. *J Disp Technol* 11(8): 666–669.

[10] Sirringhaus H (2014) Organic field-effect transistors: the path beyond amorphous silicon. *Adv Mater* 26(9): 1319–1335.

[11] Schwartz G, et al. (2013) Flexible polymer transistors with high pressure sensitivity for application in electronic skin and health monitoring. *Nat Commun* 4: 1859.

[12] Zaki T, et al. (2012) A 3.3 V 6-bit 100 kS/s current-steering digital-to-analog converter using organic p-type thin-film transistors on glass. *IEEE J Solid-State Circuits* 47(1): 292–300.

[13] Kjellander BC, et al. (2013) Optimized circuit design for flexible 8-bit RFID transponders with active layer of ink-jet printed small molecule semiconductors. *Org Electron* 14(3): 768–774.

[14] Shih CC, et al. (2015) Conjugated polymer nanoparticles as nano floating gate electrets for high performance nonvolatile organic transistor memory devices. *Adv Funct Mater* 25(10): 1511–1519.

[15] Yagi I, et al. (2008) A flexible full-color AMOLED display driven by OTFTs. *J Soc Inf Disp* 16(1): 15–20.

[16] Tee BC-K, et al. (2015) A skin-inspired organic digital mechanoreceptor. *Science* 350(6258): 313–316.

[17] Xu Y, Liu C, Khim D, Noh Y-Y (2015) Development of high-performance printed organic field-effect transistors and integrated circuits. *PCCP* 17(40): 26553–26574.

[18] Xu Y, et al. (2012) Tunable contact resistance in double-gate organic field-effect transistors. *Org Electron* 13(9): 1583–1588.

[19] Roichman Y, Tessler N (2002) Structures of polymer field-effect transistor: experimental and numerical analyses. *Appl Phys Lett* 80(1): 151–153.

[20] Park SK, Jackson TN, Anthony JE, Mourey DA (2007) High mobility solution processed 6, 13-bis (triisopropyl-silylethynyl) pentacene organic thin film transistors. *Appl Phys Lett* 91(6): 3514.

[21]   Minemawari H, et al. (2011) Inkjet printing of single-crystal films. *Nature* 475(7356): 364–367.

[22]   Tang W, et al. (2014) Inkjet printed fine silver electrodes for all-solution-processed low-voltage organic thin film transistors. *J Mater Chem C* 2(11): 1995–2000.

[23]   Sele CW, et al. (2009) Controlled deposition of highly ordered soluble acene thin films: effect of morphology and crystal orientation on transistor performance. *Adv Mater* 21(48): 4926–4931.

[24]   Pierre A, et al. (2014) All-printed flexible organic transistors enabled by surface tension-guided blade coating. *Adv Mater* 26(32): 5722–5727.

[25]   Chang J, Chi C, Zhang J, Wu J (2013) Controlled growth of large-area high-performance small-molecule organic single-crystalline transistors by slot-die coating using a mixed solvent system. *Adv Mater* 25(44): 6442–6447.

[26]   Giri G, et al. (2011) Tuning charge transport in solution-sheared organic semiconductors using lattice strain. *Nature* 480(7378): 504–508.

[27]   Kang H, et al. (2014) Megahertz-class printed high mobility organic thin-film transistors and inverters on plastic using attoliter-scale high-speed gravure-printed sub-5 μm gate electrodes. *Org Electron* 15(12): 3639–3647.

[28]   Pastorelli F, et al. (2016) The organic power transistor: Roll-to-Roll manufacture, thermal behavior, and power handling when driving printed electronics. *Adv Eng Mater* 18(1): 51–55.

[29]   Khim D, et al. (2013) Simple bar-coating process for large-area, high-performance organic field-effect transistors and ambipolar complementary integrated circuits. *Adv Mater* 25(31): 4302–4308.

[30]   Qi Z, et al. (2013) All-brush-painted top-gate organic thin-film transistors. *J Mater Chem C* 1(18): 3072–3077.

[31]   Fukuda K, Sekine T, Kumaki D, Tokito S (2013) Profile control of inkjet printed silver electrodes and their application to organic transistors. *ACS Appl Mat Interfaces* 5(9): 3916–3920.

[32]   Jeong J, et al. (2008) Modelling and numerical analysis for wavy edge in printed source and drain electrodes of thin-film transistors. *Electron Lett* 44(10): 616–617.

[33]   Yan H, et al. (2009) A high-mobility electron-transporting polymer for printed transistors. *Nature* 457(7230): 679–686.

[34]   Li J, et al. (2012) A stable solution-processed polymer semiconductor with record high-mobility for printed transistors. Sci Rep 2(754): 1–6.

[35]   Zhang W, et al. (2010) Indacenodithiophene semiconducting polymers for high-performance, air-stable transistors. *J Am Chem Soc* 132(33): 11437–11439.

[36] Kim G, et al. (2014) A thienoisoindigo-naphthalene polymer with ultrahigh mobility of 14.4 cm2/V s that substantially exceeds benchmark values for amorphous silicon semiconductors. *J Am Chem Soc* 136(26): 9477–9483.

[37] Noh J, et al. (2015) Key issues with printed flexible thin film transistors and their application in disposable RF sensors. *Proc IEEE* 103(4): 554–566.

[38] Ante F, et al. (2012) Contact resistance and megahertz operation of aggressively scaled organic transistors. *Small* 8(1): 73–79.

[39] Kang B, Lee WH, Cho K (2013) Recent advances in organic transistor printing processes. *ACS Appl Mat Interfaces* 5(7): 2302–2315.

[40] Yin X, Kumar S (2006) Flow visualization of the liquid emptying process in scaled-up gravure grooves and cells. *Chem Eng Sci* 61(4): 1146–1156.

[41] Kapur N (2003) A parametric study of direct gravure coating. *Chem Eng Sci* 58(13): 2875–2882.

[42] Sung D, De La Fuente Vornbrock A, Subramanian V (2010) Scaling and optimization of gravure-printed silver nanoparticle lines for printed electronics. *IEEE Trans Compon Packa Technol* 33(1): 105–114.

[43] Higgins SG, et al. (2015) Quantitative analysis and optimization of gravure printed metal ink, dielectric, and organic semiconductor films. *ACS Appl Mat Interfaces* 7(9): 5045–5050.

[44] Schmidt GC, et al. (2010) Modified mass printing technique for the realization of source/drain electrodes with high resolution. *Org Electron* 11(10): 1683–1687.

[45] De La Fuente Vornbrock A, et al. (2010) Fully gravure and ink-jet printed high speed pBTTT organic thin film transistors. *Org Electron* 11(12): 2037–2044.

[46] Voigt MM, et al. (2010) Polymer field-effect transistors fabricated by the sequential gravure printing of polythiophene, two insulator layers, and a metal ink gate. *Adv Funct Mater* 20(2): 239–246.

[47] Schmidt GC, et al. (2015) Fully printed flexible audio system on the basis of low-voltage polymeric organic field effect transistors with three layer dielectric. *J Polym Sci, Part B: Polym Phys* 53(20): 1409–1415.

[48] Kheradmand-Boroujeni B, et al. (2014) Analog characteristics of fully printed flexible organic transistors fabricated with low-cost mass-printing techniques. *IEEE Trans Electron Devices* 61(5): 1423–1430.

[49] Peng B, et al. (2014) High performance organic transistor active-matrix driver developed on paper substrate. Sci Rep 4(6430): 1–7.

[50] Fukuda K, et al. (2015) Reverse-offset printing optimized for scalable organic thin-film transistors with submicrometer channel lengths. Adv Electron Mater 1(8): 1500145.

[51] Singh M, Haverinen HM, Dhagat P, Jabbour GE (2010) Inkjet printing—process and its applications. *Adv Mater* 22(6): 673–685.

[52] Wu Y, et al. (2005) High-performance organic thin-film transistors with solution-printed gold contacts. *Adv Mater* 17(2): 184–187.

[53] Wu Y, Li Y, Ong BS (2006) Printed silver ohmic contacts for high-mobility organic thin-film transistors. *J Am Chem Soc* 128(13): 4202–4203.

[54] Wu Y, Li Y, Ong BS (2007) A simple and efficient approach to a printable silver conductor for printed electronics. *J Am Chem Soc* 129(7): 1862–1863.

[55] Sirringhaus H, et al. (2000) High-resolution inkjet printing of all-polymer transistor circuits. *Science* 290(5499): 2123–2126.

[56] Wang J, et al. (2004) Dewetting of conducting polymer inkjet droplets on patterned surfaces. *Nat Mater* 3(3): 171–176.

[57] Wang J, Gu J, Zenhausern F, Sirringhaus H (2006) Low-cost fabrication of submicron all polymer field effect transistors. *Appl Phys Lett* 88: 133502.

[58] Sele CW, von Werne T, Friend RH, Sirringhaus H (2005) Lithography-free, self-aligned inkjet printing with sub-hundred-nanometer resolution. *Adv Mater* 17(8): 997–1001.

[59] Noh YY, Zhao N, Caironi M, Sirringhaus H (2007) Downscaling of self-aligned, all-printed polymer thin-film transistors. *Nat Nanotechnol* 2(12): 784–789.

[60] Zhao N, et al. (2007) Self-aligned inkjet printing of highly conducting gold electrodes with submicron resolution. *J Appl Phys* 101: 064513.

[61] Caironi M, et al. (2010) High yield, single droplet electrode arrays for nanoscale printed electronics. *ACS Nano* 4(3): 1451–1456.

[62] Doggart J, Wu Y, Liu P, Zhu S (2010) Facile inkjet-printing self-aligned electrodes for organic thin-film transistor arrays with small and uniform channel length. *ACS Appl Mat Interfaces* 2(8): 2189–2192.

[63] Stringer J, Derby B (2010) Formation and stability of lines produced by inkjet printing. *Langmuir* 26(12): 10365–10372.

[64] Tang W, et al. (2014) Controlling the surface wettability of the polymer dielectric for improved resolution of inkjet-printed electrodes and patterned channel regions in low-voltage solution-processed organic thin film transistors. *J Mater Chem C* 2(28): 5553–5558.

[65] Doggart J, Wu Y, Zhu S (2009) Inkjet printing narrow electrodes with <50 μm line width and channel length for organic thin-film transistors. *Appl Phys Lett* 94(16): 163503.

[66] Dong H, Carr WW, Bucknall DG, Morris JF (2007) Temporally-resolved inkjet drop impaction on surfaces. *AlChE J* 53(10): 2606–2617.

[67] Smith P, et al. (2006) Direct ink-jet printing and low temperature conversion of conductive silver patterns. *J Mater Sci* 41(13): 4153–4158.

[68] Feng L, et al. (2013) Ultralow-voltage solution-processed organic transistors with small gate dielectric capacitance. *IEEE Electron Device Lett* 34(1): 129–131.

[69] Feng L, et al. (2014) All-solution-processed low-voltage organic thin-film transistor inverter on plastic substrate. *IEEE Trans Electron Devices* 61(4): 1175–1180.

[70] Tang W, et al. (2016) Highly efficient all-solution-processed low-voltage organic transistor with a micrometer-thick low-k polymer gate dielectric layer. Adv Electron Mater 2(5): 1500454.

[71] Feng L, et al. (2016) Unencapsulated air-stable organic field effect transistor by all solution processes for low power vapor sensing. Sci Rep 6(20671): 1–9.

Screen-Printed Front Junction *n*-Type Silicon Solar Cells

Yuguo Tao

Abstract

This chapter aims to provide students/engineers/scientists in the field of photovoltaics with the basic information needed to understand the operating principles of screen-printed front junction *n*-type silicon solar cells. The relevant device fabrication processing is described, from texturing, diffusion, passivation and antireflection coating, to screen-printed and fired-through metallization as well as the technologies that are currently used for most industrially produced solar cells. A brief description of the characterisation approaches is given and discussed for an understanding and analysis of the loss mechanisms in a finished cell, including resistance loss, recombination loss, and optical loss. The application of advanced cell concepts and the improved technologies for further increasing cell efficiency, such as selectively doping structure and tunnel oxide passivated contact, are addressed for screen-printed front junction *n*-type silicon solar cells.

Keywords: screen printed, front emitter, *n*-type silicon solar cell, recombination, surface passivation

1. Introduction

Photovoltaics is the process of converting sunlight directly into electricity using solar cells. For the past few decades, the main research tendency in solar cells has been to develop cells which are both highly efficient and also cost-effective. Because of the abundance and nontoxicity of silicon, the fabrication simplicity, and the vast amount of accumulated knowledge in processing developed in the integrated circuit industry, silicon wafer-based solar cells dominate the very dynamic photovoltaic market. Silicon solar cells generate electricity via absorbing photons and generating electron–hole pairs, which are separated by a *pn*-junction and flow to electrical contacts and then into an external circuit. Due to its relative insensitivity to the degradation caused by exposure to cosmic rays, *p*-type (typically boron doped) silicon solar cells have

dominated all industrial development for decades. Until the 1980s, the main application of photovoltaics was to power space satellites [1]. For today's industrial mass production for terrestrial electricity generation, a typical state-of-the-art *p*-type silicon solar cell with an homogeneous emitter and full aluminium back surface field (Al-BSF) has an efficiency of ~19% with the standard silicon nitride passivation and screen-printed silver paste metallization on the front. However, a lot of research has been being conducted in the field of *n*-type (typically phosphorus doped) silicon-based solar cells, because *n*-type silicon provides several advantages over *p*-type, including better tolerance to common impurities (e.g., iron) [2], high bulk lifetime, and no light-induced degradation due to the boron–oxygen complex formation [3]. Accordingly, *n*-type silicon solar cells with high efficiency can be potentially more cost-effective than *p*-type silicon-based cells. In addition, for either *n*-type or *p*-type silicon solar cells, electrical contacts are needed to extract carriers to an external circuit. In order to form electrical contacts, the silver paste screen-printing/firing-through technology is a very reliable and relatively simple process in today's silicon solar cell mass production. Hence, in this chapter, the focus will be on front junction *n*-type silicon solar cells with screen-printed and fired-through contacts on both sides, including their operating principles, fabrication processes, and more advanced cell concepts.
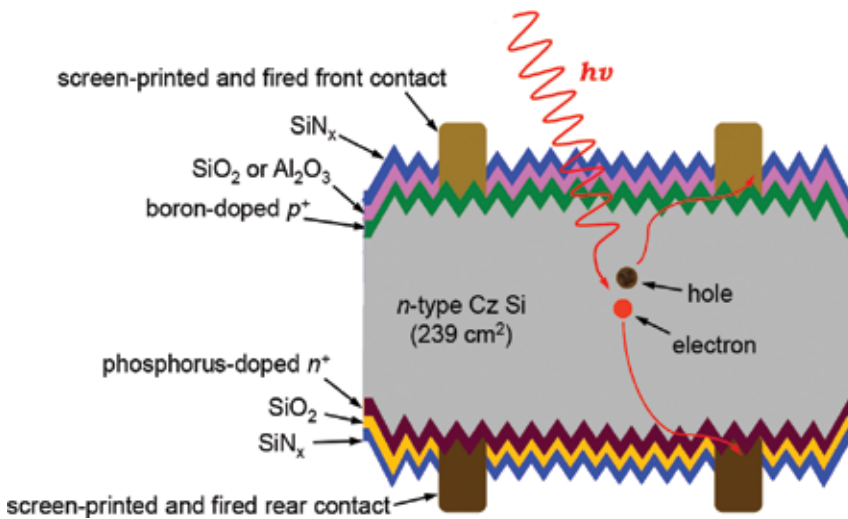

Figure 1. Schematic structure of a screen-printed front junction *n*-type silicon solar cell in cross-section (not to scale), featuring bifacial architecture.

Figure 1 shows a schematic of the basic structure for a typical screen-printed front junction *n*-type silicon solar cell, which represents the passivated emitter and rear totally diffused (PERT) cell structure [4]. The bulk material is *n*-type silicon wafer with a resistivity of around 5 Ω cm (phosphorus doping level about 9.2E10^{14} cm^{-3}) and a thickness of ~180 μm. The wafer surface is randomly textured to form small size of pyramids to reduce surface reflection. Hence, more photons can be absorbed in the cell. The front emitter is boron-doped with a surface dopant concentration in the range of 8E10^{18} to 8E10^{19} cm^{-3}, and passivated by silicon dioxide (SiO$_2$) or

aluminium oxide (Al_2O_3). The back surface field is phosphorus-doped with a surface concentration of typically over $1E10^{20}$ cm^{-3} and passivated by SiO_2. A hydrogen-rich silicon nitride (SiN_x) on both the front and rear surfaces acts as a passivation layer and as an antireflective coating (ARC) layer. The electrical contacts on both sides are formed by screen-printing different silver pastes and then co-firing through SiN_x the layer at a high temperature (over 700°C). Note that this basic cell structure features a bifacial architecture, which can also collect radiation from the rear side of solar cell, and hence has the potential to achieve an increased energy yield in certain module configurations. To understand the operating principles of a silicon solar cell with this basic structure, the next section will describe the basic physics in detail.

2. Operating principles of a front junction *n*-type silicon solar cell

2.1. Energy-band diagram

Figure 2 shows the schematic energy-band diagram for the fundamental operating principles of a screen-printed front junction *n*-type silicon solar cell. The p^+ emitter region is formed by 'doping' the front side of an *n*-type silicon wafer with boron dopants in high concentration, and joining the p^+ region and the *n* region forms the *pn*-junction. Due to the doping concentration gradient across the *pn*-junction, electrons flow by diffusion from the *n* region to the p^+ region, and holes flow by diffusion from the p^+ region to *n* region. This leaves behind exposed charges on ionized doping atoms at lattice sites, which form the space charge region (SCR). These exposed charges build up an electric field that hinders the natural flow of electrons and holes until an equilibrium situation is reached. The built-up electric field causes a bending of the energy bands (E_V and E_C).
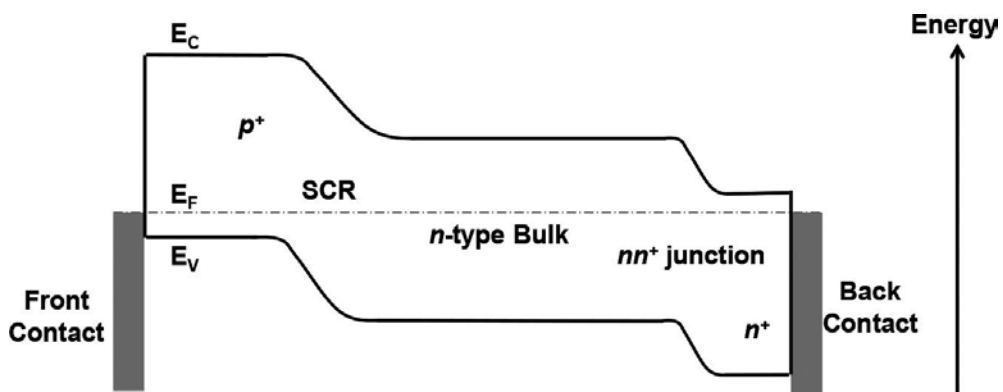

Figure 2. Schematic energy-band diagram of a screen-printed front junction *n*-type silicon solar cell in thermal equilibrium (without illumination or applied voltage), including p^+ emitter, *pn*-junction, space charge region (SCR), nn^+ high–low junction and n^+ back surface field (BSF).

The n^+ back surface field region is produced by 'doping' the rear side of n-type silicon wafer with phosphorus dopants in much higher doping concentration (typically over $1E10^{20}$ cm^{-3}) than in the n bulk region (typically about $1E10^{15}$ cm^{-3}). The formed nn^+ high–low junction induces a slight bending of the energy bands. In the case without illumination or applied voltage, the cell is in thermal equilibrium with a single, constant-valued Fermi level (E_F), as shown in **Figure 2**.

When the cell is illuminated, photons with energy greater than the silicon band gap energy are absorbed to excite electrons from the valence band to the conduction band, which generates an electron–hole pair (a hole refers to the missing electron in the valence band), as shown in **Figure 3**. The generated electrons and holes can diffuse within the solar cell until they reach the SCR, if they do not recombine. Then, the electric field at the pn-junction separate these carriers by sweeping electrons to the n region and holes to the p^+ region. The induced nn^+ high–low junction also can sweep holes away the back surface field and the back contact, and hence reduce the back surface recombination. In the case of illumination, quasi-Fermi levels (E_{Fn} for electrons and E_{Fp} for holes) are used to analyse the solar cell in non-equilibrium. To allow electrical contacts to extract carriers from both front and back sides, E_{Fp} is essentially continuous with the Fermi level of the front contact metal, while E_{Fn} is at the same energetic position with the back contact metal. In the bulk quasi-neutral regions, both E_{Fp} and E_{Fn} are approximately constant. In the p^+ emitter region, the electrical contact is described as an ohmic contact. In the n^+ back surface field region, the contact is of a Schottky-type that the contact metal induces a barrier to majority carriers (electrons), which gives rise to an undesirable contact resistance. Therefore, to obtain a decent cell performance, a proper doping profile in both the p^+ and the n^+ regions is needed.
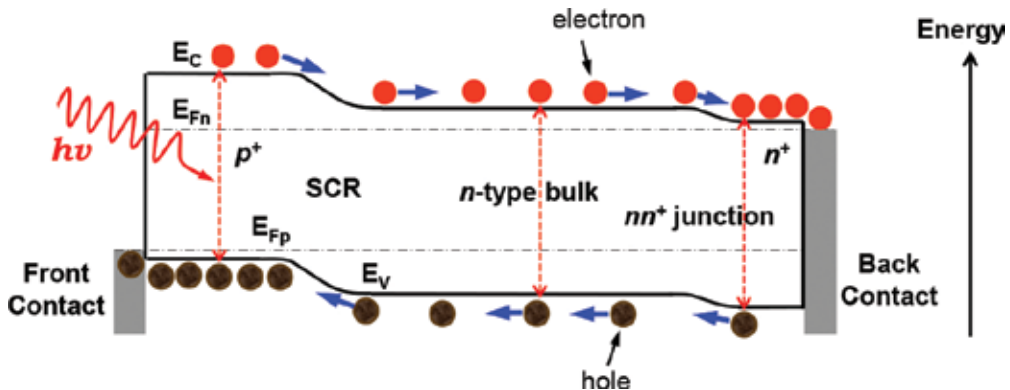

Figure 3. Schematic energy-band diagram of a screen-printed front junction n-type silicon solar cell in a non-equilibrium (with illumination); including photon absorption, carrier generation and separation.

2.2. Solar cell output parameters

The *Ideal Diode Law* (one-diode model) is often used to describe an ideal silicon solar cell, which is expressed as

$$J = J_0 \left[\exp\left(\frac{qV}{kT} \right) - 1 \right] \tag{1}$$

where J is the current density, J_0 is the saturation current density (the solar cell leakage current density in the dark), V is the voltage, q is the electronic charge, k is the Boltzmann's constant, and T is the absolute temperature. J_0 is defined as [5]

$$J_0 = \frac{qD_e n_i^2}{L_e N_A} + \frac{qD_h n_i^2}{L_p N_D} \tag{2}$$

where D_e (D_h) is the diffusion constant of electrons (holes), n_i is the intrinsic carrier concentration, L_e (L_p) is the diffusion length of electrons (holes), and N_A (N_D) is the total density of acceptors (donors).

When the cell is illuminated, it is ideally modelled as

$$J = J_0 \left[\exp\left(\frac{qV}{kT} \right) - 1 \right] - J_l \tag{3}$$

where J_l is the light-generated current density. At the short-circuit condition ($V = 0$), the maximum light-generated current density is the short circuit current density J_{sc}, hence $|J_{sc}| = J_l$.

For an actual solar cell, Eq. (3) becomes

$$J = J_0 \left[\exp\left(\frac{qV}{nkT} \right) - 1 \right] - J_l \tag{4}$$

where n is the ideality factor, and typically in the range of between 1 and 2.

The resulting dark and illuminated *J–V* curves by the diode law are shown in **Figure 4a**. The illuminated *J–V* curve is most often plotted with the output power in the first quadrant, as shown in **Figure 4b**, and represented by

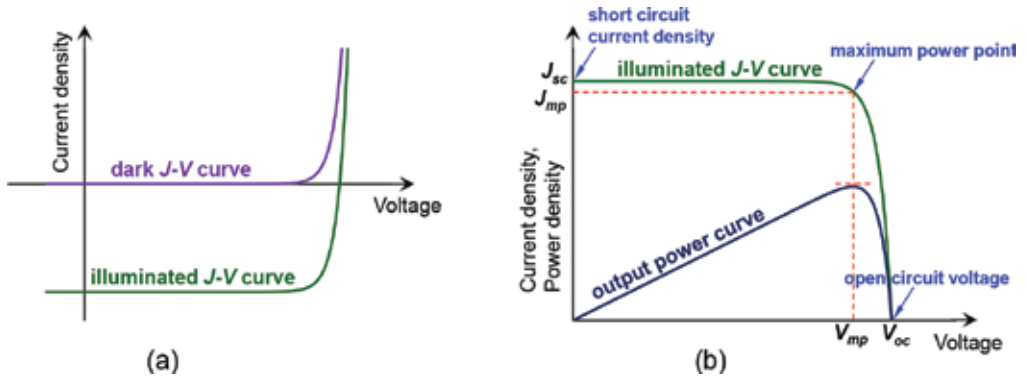$$J = J_l - J_0 \left[\exp\left(\frac{qV}{nkT} \right) - 1 \right] \tag{5}$$

Figure 4. Dark and illuminated *J–V* curves of a silicon solar cell (a); a typical representation of an illuminated *J–V* curve as well as output power density curve as a function of voltage (b), including indication of the short-circuit point (0, J_{sc}), the open-circuit point (V_{oc}, 0), as well as the maximum power point (V_{mp}, J_{mp}).

In **Figure 4b**, the maximum power point (V_{mp}, J_{mp}) is indicated. The fill factor (*FF*) is a metric of the *pn*-junction quality and the parasitic resistance of a finished silicon solar cell, and defined as

$$FF = \frac{J_{mp}V_{mp}}{J_{sc}V_{oc}} \tag{6}$$

where V_{oc} is the open circuit voltage. At the open-circuit condition ($J = 0$), the cell voltage is the V_{oc}.

Finally, the cell energy-conversion efficiency is defined as

$$\eta = \frac{J_{sc}V_{oc}FF}{P_{in}} \tag{7}$$

where P_{in} is the total power density of the light incident on the solar cell. For an ideal single junction crystalline silicon solar cell (energy band gap E_g=1.12 *eV* at 25°C), its theoretical efficiency limit is about 30%, based on a detailed balancing of incident and generated power density [6]. The major fundamental loss mechanisms in an ideal silicon solar cell include: (1) photons with energy less than 1.12 eV ($E\_photon < E\_g$) cannot be absorbed (directly transmit through the cell); (2) the excessive energy in the photons with high energy ($E\_photon > E\_g$) is wasted as the generated electron–hole pair relax back to the edges of respective carrier band (electrons back to conduction band, and holes to valence band) through thermalization; and (3) the split between the two quasi-Fermi levels must stay within two energy gap ($|E\_Fn - E\_Fp| < E\_g$).

2.3. Resistance loss

Actual silicon solar cells generally have a parasitic series resistance (R_s) and a shunt resistance (R_{sh}). Both R_s and R_{sh} have a negative impact on *FF* and cause ohmic losses. For a screen-printed front junction *n*-type silicon solar cell, **Figure 5** shows the schematic components of total R_s in a finished cell, including: (1) sheet resistance of the p^+ emitter layer ($R_{emitter}$) and the n^+ back surface field layer (R_{BSF}); (2) bulk resistance of *n*-type wafer ($R_{substrate}$); (3) metallic resistance of the front gridline (R_{finger}) and the rear gridline (R'_{finger}); (4) contact resistance between screen-printed metal contacts and silicon on the front side ($R_{contact}$) and the rear side ($R'_{contact}$); and (6) metallic resistance of the front bus-bar (R_{busbar}) and the rear bus-bar (R'_{busbar}). The specific values of these components can be approximately estimated by the approach developed in [7].
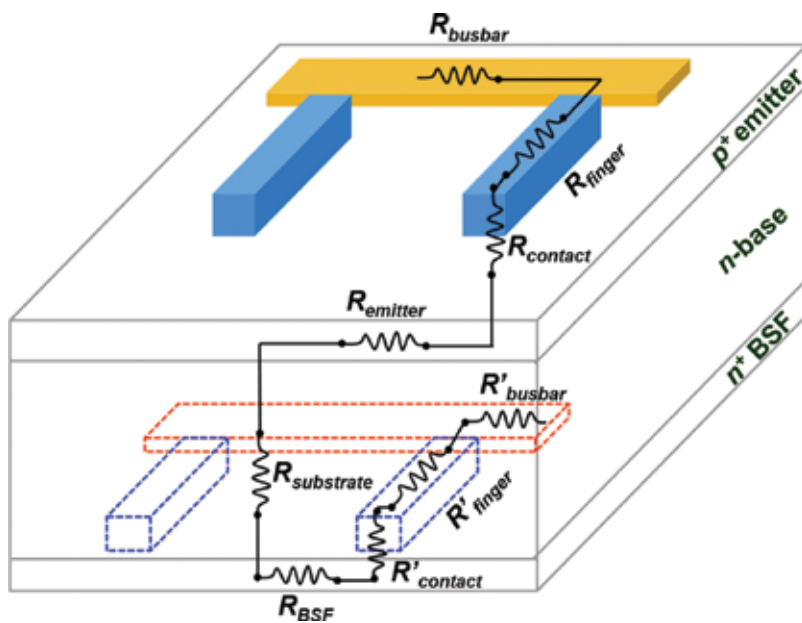

Figure 5. Schematic structure of major components of series resistance (R_s) in a screen-printed front junction *n*-type silicon solar cell.

The R_{sh} is particularly due to the non-ideality of the *pn*-junction and some defects near the junction, especially around cell edges. Consequently, in reality, the illuminated *J–V* curve of a screen-printed silicon solar cell with R_s and R_{sh} is given by

$$J = J_I - J_0 \left\{ \exp\left[\frac{V + AJR_s}{\left(\frac{nkT}{q}\right)} \right] - 1 \right\} - \frac{V + AJR_s}{AR_{sh}} \tag{8}$$

where A is the total area of a solar cell, and typically about 239 cm^2 for the industrial pseudo-square n-type silicon solar cells. So, in order to design and fabricate a silicon solar cell with high-efficiency performance, minimizing the ohmic losses is necessary. In addition, carrier recombination after generation can also degrade the cell performance as described in the following section, so it should be minimized as well.

2.4. Recombination loss and saturation current density

The generated electron–hole pair can recombine if they are not efficiently separated and collected. There are typically three recombination mechanisms that can occur in parallel in silicon solar cells. First, radiative recombination is the process that electron makes a band-to-band transition while emitting a photon as light. Hence, it is the reverse of the light absorption. But it is often neglected for silicon solar cell, because silicon is an indirect-band-gap material and a phonon is required for this type of recombination. Second, Auger recombination refers to electrons and holes that recombine and use the excess energy to excite a free carrier. Then, this excited free carrier relaxes back to its original energy status by emitting phonons. This type of recombination is particularly effective in the heavily doped regions with doping concentration over 10^{17} cm^{-3}, for instance, the p^+ emitter and the n^+ back surface field regions in screen-printed n-type silicon solar cells. Third, recombination through traps, the so-called SRH recombination named from Schockley, Read and Hall [8, 9], is a very effective process whereby electrons relax from the conduction band to the defect levels (within the forbidden gap) that are created by impurities or defects, then relax to the valence band and recombine with holes. For industrial n-type silicon Czochralski wafers, this type of recombination is also very usual as the impurities induced during the entire device fabrication process introduce energy levels near the middle of the forbidden gap and become very effective recombination centres.

The carrier lifetime is typically used to define the time for recombination to occur after the electron–hole generation. Because the three recombination mechanisms occur in parallel, the silicon material bulk lifetime (τ_{bulk}) is given by

$$\frac{1}{\tau_{bulk}} = \frac{1}{\tau_{radiative}} + \frac{1}{\tau_{Auger}} + \frac{1}{\tau_{SRH}}$$

(9)

where $\tau\_radiative$ is the radiative lifetime, τ_Auger is the Auger lifetime, τ_SRH is the SRH lifetime.

In addition, for crystalline silicon wafers, dangling bonds are present on the front and back surfaces, and introduce defect levels throughout the energy-band gap. Surface recombination velocity (s) is typically used to estimate the surface passivation quality and can be approximately calculated for a decently passivated surface ($s < 1000$ cm/s) by

$$\frac{1}{\tau_{eff}} = \frac{1}{\tau_{bulk}} + \frac{2s}{d} \tag{10}$$

where d is the silicon wafer thickness, τ_eff is the effective lifetime. Both τ_eff and τ_bulk can be directly measured by the quasi-steady-state photoconductance (QSSPC) technique [10], hence s can be extracted.

For silicon solar cells, recombination after carrier generation not only reduces J_{sc} but also degrades V_{oc}. According to Eq. (4), the total saturation current density ($J_{0,total}$) has a strong impact on V_{oc}. At open-circuit condition, Eq. (4) becomes

$$V_{oc} = \frac{nkT}{q} ln\left(\frac{J_{sc}}{J_{0,\ total}} + 1\right) \tag{11}$$

In order to conduct a detailed analysis about the recombination contribution from each part of a finished screen-printed *n*-type silicon solar cell, $J_{0,total}$ can be estimated by

$$J_{0,\ total} = J_{0e} + J_{0b,\ bulk} + J_{0b} \tag{12}$$

where J_{0e} is the total saturation current density of front emitter side, including the passivated emitter regions and the metal contact regions, and is expressed by

$$J_{0e} = \left(1 - f_{front}\right) \cdot J_{0e,pass} + f_{front} \cdot J_{0e,contact} \tag{13}$$

where f_{front} is the fraction of screen-printed metal contact coverage on the front emitter. $J_{0e,pass}$ is the emitter saturation current density of passivated regions and can be directly obtained from the lifetime measurement on symmetrical structures (passivation/p^+/n/p^+/passivation) by the QSSPC technique. $J_{0e,contact}$ is the metal-induced emitter saturation current density on the contacted regions and can be extracted by numerical modelling, i.e, two-dimensional simulations [11]. It also can be experimentally estimated on a specifically designed test sample structure, as shown in **Figure 6a**, by the following equation

$$2 \cdot J_{0e,\ measured} = \left(J_{0e,contact} - J_{0e,pass}\right) \cdot f_{front} + 2 \cdot J_{0e,\ pass} \tag{14}$$
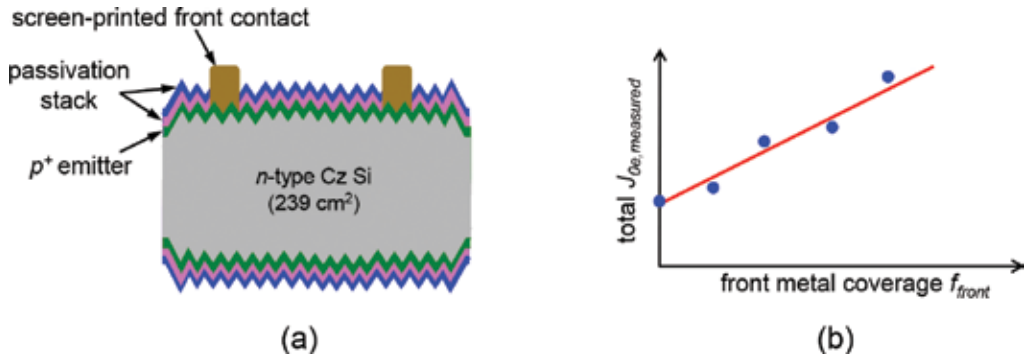
Figure 6. Schematic of a test sample symmetrical structure with screen-printed contact on one side for extracting $J_{0e,contact}$ (a); a typical representation of $J_{0e,contact}$ line fitting as a function of the front metal contact coverage f_{front} on the test samples (b).

where $J_{0e,measured}$ is the directly measured saturation current density value from the lifetime measurement on the test sample structure. So, $J_{0e,contact}$ can be extracted from the resulting slope of the line fitting, as shown in **Figure 6b**.

In Eq. (12), $J_{0b,bulk}$ is the saturation current density of substrate bulk region and is determined by bulk lifetime and the bulk resistivity. Although it is a limited validation, $J_{0b,bulk}$ can be approximately given by [12]

$$J_{0b,bulk} = q n_i^2 \frac{W}{N_D \tau_p} \tag{15}$$

where the intrinsic carrier concentration $n\_i = 8.3 \times 10^9 \ cm^{-3}$ [13]. N_D is the doping density of n-type silicon bulk region, i.e., $N\_D = 9.2 \times 10^{14} \ cm^{-3}$ for a bulk resistivity of 5 Ω cm. W is the silicon wafer thickness, typically about 180 μm. τ_p is the Auger lifetime with the specific value referred to [14].

Similar to J_{0e}, J_{0b} in Eq. (12) is the saturation current density of rear side on a finished cell, including the passivated back surface field regions and the metal contacted regions, and is given by

$$J_{0b} = (1 - f_{rear}) \cdot J_{0b,pass} + f_{rear} \cdot J_{0b,contact} \tag{16}$$

where f_{rear} is the fraction of metal contact coverage on the back surface field. $J_{0b,pass}$ is the saturation current density of passivated back surface field regions and also can be directly obtained from the lifetime measurement on symmetrical structure (passivation/n^+/n/n^+/ passivation) by the QSSPC technique. $J_{0b,contact}$ is the metal-induced saturation current density of contacted regions on the back surface field and can be extracted by using the same method

as estimating $J_{0e,contact}$. Its test sample structure is shown in **Figure 7a**, with the following calculation equation

$$2 \cdot J_{0b,\,measured} = \left(J_{0b,contact} - J_{0b,pass} \right) \cdot f_{rear} + 2 \cdot J_{ob,\,pass} \tag{17}$$

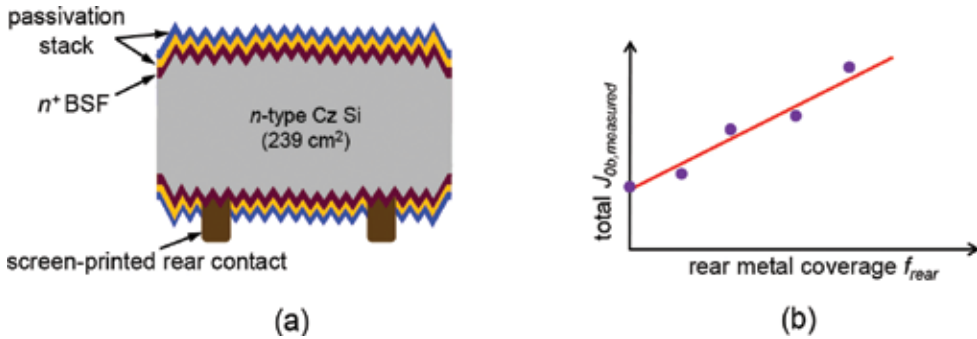(a)   (b)

Figure 7. Schematic of a test sample symmetrical structure screen-printed contact on one side for extracting $J_{0b,contact}$ (a); a typical representation of $J_{0b,contact}$ line fitting as a function of the rear metal contact coverage f_{rear} on the test samples (b).

where $J_{0b,measured}$ is the directly obtained value from the lifetime measurement on the test sample structure. So, $J_{0b,contact}$ can be extracted from the resulting slope of the line fitting, as shown in **Figure 7b**.

So, in order to obtain a low $J_{0,total}$ (hence high cell V_{oc}), considering a trade-off among these saturation current densities in Eqs. (12)–(17) is necessary. A detailed example about the recombination contribution from each part of a finished cell will be specifically given in Section 3.

2.5. Optical loss

Apart from the recombination that contributes to the J_{sc} loss because the total number of generated electrons decreases after recombination, optical loss is another contributor for the J_{sc} loss since the total number of photons that can be absorbed to create electron–hole pair becomes less. **Figure 8** shows the typical mechanisms of optical losses in a screen-printed *n*-type silicon solar cell, including (1) reflection/shading at the screen-printed front metal contact, (2) reflection at the cell front surface, (3) reflection from the rear side out of cell, (4) absorption in the front passivation and antireflection coating layers, (5) absorption via free carrier absorption in the p^+ emitter layer, (6) absorption via free carrier absorption in the n^+ back surface field layer, (7) absorption in the rear passivation layers, (8) absorption in the screen-printed rear metal contact, (9) transmission without being absorbed in the cell. Therefore, to fabricate high-efficiency screen-printed front junction *n*-type silicon solar cells, these optical losses need to be reduced.
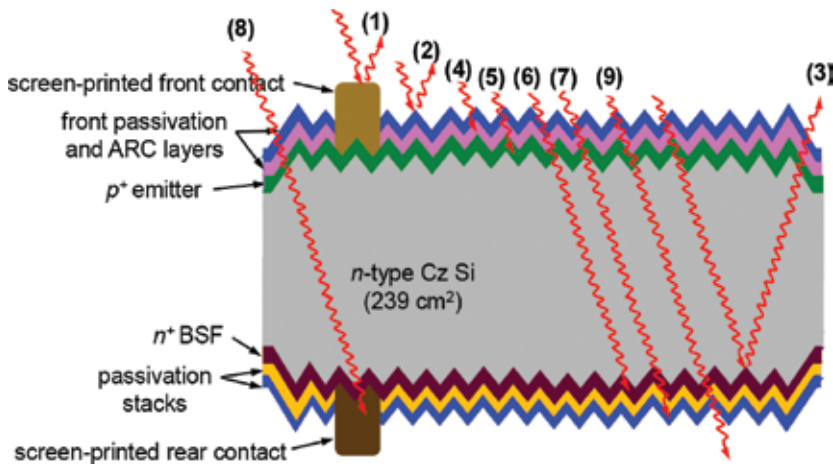
Figure 8. Schematic structure of optical loss mechanisms in a screen-printed front junction *n*-type silicon solar cell.

So, to reduce the optical loss in a finished cell, front gridline should be as narrow as possible to reduce metal shading while not sacrificing conductivity. Currently, the screen-printed gridline in mass production typically demonstrates ~60 μm width. The size of pyramids also needs to be as small as possible to reduce reflection at the front surface, and currently, typical size is in the range of 3–6 μm. Low doping levels in the diffused regions (p^+ emitter and n^+ back surface field) can reduce the free carrier absorption, but the metal contact resistance and the lateral transport resistance of these layers should not be sacrificed.

3. Cell fabrication process with screen-printed metallization

In this section, the typical processes of fabricating screen-printed front junction *n*-type silicon solar cells are presented, starting from as-cut wafers to finished cells. All these cell fabrication processes are industrially relevant, and some of them have already been implemented on production lines.

3.1. Saw damage removal and texturing

After the silicon ingot is grown, wire sawing is typically used to slice silicon ingots into wafers with a resulting thickness of around 200 μm, and often in pseudo-square shape (~156 × 156 mm^2) with total area of about 239–242 cm^2 depending on the diameter of the original ingot. During this process, the sawing damages the entire surface of both sides of the silicon wafers, with the damage depth of approximately 10 μm. This saw-induced damage has a very bad effect on the electronic quality of the wafer as they dramatically increase the surface recombination velocity, and hence have to be removed together with other contaminants prior to the next high-temperature diffusion step. This etching of the saw damage normally occurs in heated potassium hydroxide (KOH) solution at ~80°C for few minutes. This etching reaction

takes place in three steps, including oxidation of silicon, formation of a solvable salt and dissolving of the salt in water, which is summarized in [15, 16]

$$Si + 2H_2O + OH^- \rightarrow HSiO_3^- + H_2 \tag{18}$$

In addition, this is a selective etching process as different crystallographic orientations have different etch rates, with the lowest etch rate for the <111> plane. In order to effectively reduce the reflection at the front surface, isopropyl alcohol (IPA) is normally added into KOH solution to form small pyramids with a square base randomly distributed over the <100> oriented silicon surface, as shown in **Figure 9**.
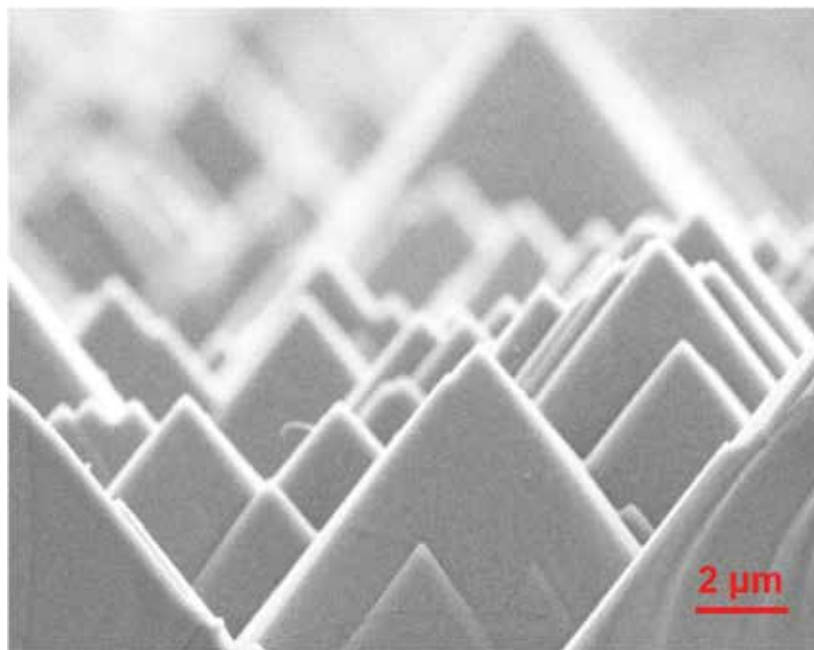

Figure 9. Appearance of a textured silicon surface for *n*-type mono-crystalline silicon wafer under a scanning electron microscope using alkaline texturing.

After texturing, the wafers are processed by a thorough cleaning to remove impurities present on the wafer surface that could diffuse into the wafer and cause carrier recombination. This cleaning typically consists of a rinsing in deionized (DI) wafer, a thorough etching in hydrochloric acid (HCl) to remove metal impurities from wafer surfaces, then another DI water rinsing, a short etching in hydrofluoric acid (HF) to etch off the native silicon dioxide (SiO_2) and to form a hydrophobic surface feature, and a final DI water rinsing and then air drying [17]. The more aggressive and more expensive 'RCA' clean ('SC-1' and 'SC-2') is another standard set of wafer cleaning steps typically used in R&D labs [18].

3.2. Boron emitter formation

To form the *pn*-junction of *n*-type silicon solar cells, a typical approach is to diffuse boron atoms into the silicon wafers. This can be implemented by depositing boron-doped silicon oxide via plasma-enhanced chemical vapour deposition (PECVD) or atmospheric pressure chemical vapour deposition (APCVD), and then annealing at high temperature. Another promising technology is direct thermal diffusion of boron from a boron tribromide (BBr_3) source, the so-called 'BBr$_3$ diffusion' process. In this process, pure nitrogen (N_2) carrier gas flows into a bubbler-containing liquid BBr_3, which forms gaseous BBr_3 and transports it into the quartz tube where the wafers are loaded in quartz boat. In the oxygen (O_2) ambient, a boron trioxide (B_2O_3) layer is formed on the silicon wafer surface through the reaction

$$4BBr_3 + 3O_2 \rightarrow 2B_2O_3 + 6Br_2 \qquad (19)$$

This reaction is often referred to as the deposition stage, as a very high concentration of boron forms in the very thin layer on the silicon surface. Next, the formed B_2O_3 reacts with the silicon atoms which can diffuse boron atoms into the silicon bulk to form the p^+ emitter layer at high temperatures (over 900°C) through the reaction

$$2B_2O_3 + 3Si \rightarrow 4B + 3SiO_2 \qquad (20)$$

which is often referred to as the diffusion stage. The formed SiO_2/B_2O_3 stack on the silicon surface is the so-called borosilicate glass (BSG) that needs to be removed to improve surface passivation quality. The resulting boron-doped p^+ emitter properties (surface doping concentration, depth and the shape of the doping profile) depend on the diffusion process temperature, diffusion duration, and gas flow rates [19, 20]. It is noteworthy that the boron emitter profiles typically show a concentration decline towards the silicon wafer surface due to the higher solubility of boron in the grown SiO_2 than in silicon [21].

Due to BBr$_3$ diffusion being a double-sided coating process, a mask on the rear side is needed to protect the rear surface where the n^+ back surface field is formed in the next process for the *n*-type front junction silicon solar cells. To eliminate these extra processes (masking, then removing mask after diffusion), ion implantation is another promising alternative technology due to its other advantages [22]: (1) formation of very uniform single-sided junction, (2) elimination of edge isolation and (3) elimination of dopant glass removal. Because boron is light element, crystal point defects (self-interstitials and vacancies) without amorphization are created during implantation [23], and a very high temperature (over 1000°C) is needed to anneal out this lattice damage [24]. To achieve high-efficiency screen-printed *n*-type silicon solar cells, an optimal boron emitter is needed to balance emitter sheet resistance, contact resistance and emitter saturation current density J_{oe} shown in Eq. (13). This can be achieved by flexibly controlling implant energy, boron ion dose and post-implantation annealing conditions.

3.3. Formation of phosphorus-doped back surface field

The most commonly used technique to form phosphorus-doped n^+ layer in the photovoltaic industry is a tube furnace diffusion process, the so-called 'POCl$_3$ diffusion' (phosphorus oxychloride) process. In this process, pure nitrogen carrier gas flows into a bubbler filled with liquid POCl$_3$, which forms gaseous POCl$_3$ and transports it into the quartz tube where the wafers are loaded in quartz boat. Phosphorus oxide (P$_2$O$_5$) is formed on the wafer surface in the oxygen ambient with the chemical reaction by

$$4POCl_3 + 3O_2 \rightarrow 2P_2O_5 + 6Cl_2 \tag{21}$$

where the formed P$_2$O$_5$ acts as a phosphorus dopant source. This is often referred to a deposition stage, as a very high concentration of phosphorus forms in the very thin layer (only tens of nanometres) on the silicon surface. Then, in the same process, the furnace temperature is often slightly increased for the next drive-in stage: in which the phosphorus atoms diffuse deeper into the silicon. Phosphorus atoms diffuse into the silicon substrate to create an n^+ layer at a relatively higher temperature, typically in the range of 800–900°C through the reaction at the wafer surface

$$2P_2O_5 + 5Si \rightarrow 4P + 5SiO_2 \tag{22}$$

where the formed SiO$_2$/P$_2$O$_5$ stack is the so-called phospho-silicate glass (PSG). The resulting doping profile depends on diffusion temperature, diffusion time and gas flow rates [25, 26].

Because the POCl$_3$ diffusion is also a double-sided coating process, a mask on the front side is needed to protect the p^+ emitter layer for the *n*-type front junction silicon solar cells. Both silicon dioxide (SiO$_2$) and silicon nitride (SiN$_x$) deposited by PECVD can act as a mask layer. Similar to the p^+ emitter formation, in order to eliminate the complicated masking process, ion implantation is a promising technology to form the n^+ back surface field. Unlike the light elements (i.e., boron), phosphorus is a heavy enough ion, that nuclear collisions dominate and result in amorphized surface during implantation. Hence, a relatively lower annealing temperature (around 850°C) can recover implantation-induced defects on the silicon wafer surface. A proper combination of implant energy, phosphorus ion dose and post-implantation annealing conditions is needed to obtain high-efficiency screen-printed *n*-type silicon solar cells [27, 28].

3.4. Surface passivation and antireflection coating

To obtain high cell performance, surface passivation plays an important role in reducing recombination in the finished cell. There are two fundamental mechanisms for surface passivation: (1) chemical passivation that the surface defect states are removed or reduced; (2) field-effect passivation that a fixed-charge dielectric is deposited on the surface to create an internal electrical field that repels or screens minority carriers inside the wafer from the

defective surfaces. For field-effect passivation, the positive-fixed-charge dielectrics (i.e., SiN_x and SiO_2) repel the positively charged holes inside the silicon wafer from the surfaces and are ideally suitable to passivate n^+ surfaces. The negative-fixed-charge dielectrics repel the negatively charged electrons from surfaces and typically are used to passivate p^+ surfaces. Aluminium oxide (Al_2O_3) is the most studied of these dielectrics [29, 30]. So, in screen-printed n-type silicon solar cells, the p^+ emitter is more often passivated by Al_2O_3 which can be formed by atomic layer deposition (ALD), APCVD or PECVD. A minimum Al_2O_3 thickness is required to achieve excellent surface passivation quality without adding significant optical loss due to its insufficient antireflection properties. The n^+ back surface field is typically passivated by thermally grown SiO_2. To simplify the cell fabrication process, in some cases, the thermally grown SiO_2 is also used to passivate the p^+ emitter, but the resulting surface passivation quality is inferior to p^+ emitters passivated by Al_2O_3 [29].

In order to further reduce reflection losses at the textured front side, a layer of hydrogen-rich silicon nitride (SiN_x:H) is normally deposited by PECVD on top of the passivation layer (Al_2O_3 or SiO_2) as an ARC. Since there is significant amount of H in this ARC layer, it can be released during the metal contact firing step at high temperature ($\sim 800°C$) and diffuse into the silicon wafer bulk region to passivate bulk defects, which reduces bulk recombination. The thickness of this ARC can be calculated by the quarter wavelength law [31]

$$d = \frac{\lambda}{4 \times n_{SiN}} \tag{23}$$

where λ is the wavelength, n_{SiN} is the refractive index of ARC layer. Reflection can be further minimized when n_{SiN} equals the geometric mean of the materials on both its sides, for instance,

$$n_{SiN} = \sqrt{n_{air} \cdot n_{Si}} \tag{24}$$

where n_{air} is the air refractive index (=1) n_{Si} is the silicon refractive index (=4). Therefore, for n_SiN =2, a typical ARC thickness is about 75 nm to obtain minimum reflectivity at wavelength of 600 nm. Because cells are eventually encapsulated to make modules under ethylene vinyl acetate (EVA) and glass which have refractive index of ~ 1.5, a slightly higher n_{SiN} (~ 2.3) is typically implemented in module application. The precursor silane and ammonia ratio (SiH_4/NH_3) during PECVD deposition are typically adjusted to obtain the proper n_{SiN} and absorption coefficient of the resulting ARC layer. Note that in the screen-printed n-type silicon solar cells, the ARC layer is deposited on top of a passivation layer, so its thickness d needs to be modified according to the thickness of the passivation layer to achieve the antireflection quality without sacrificing any surface passivation quality.

3.5. Screen-printed metallization

Screen-printed metallization is very robust, simple and widely used for PV applications since its introduction about four decades ago [32]. **Figure 10** shows the schematic of a screen-printing process. The squeegee is moved with a proper pressure over the screen that consists of emulsion and mesh wires, which presses down the screen locally against the wafer surface and pushes the paste on the wafer surface through the well-defined opened region (typically 40–60 μm wide openings). During the printing, wafer stays on the stage under vacuum condition. The printer settings, i.e., snap-off distance, print pressure and print speed, are very critical parameters to obtain a good aspect ratio (height to width ratio) of screen-printed gridlines.
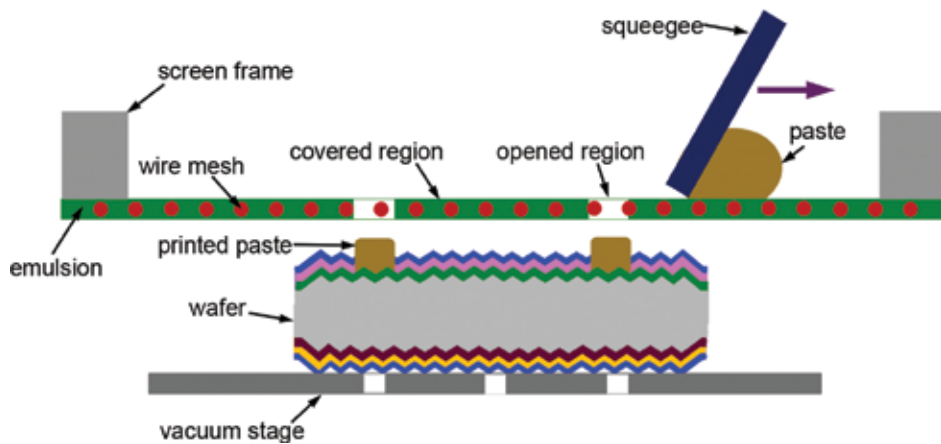

Figure 10. Schematic of a screen-printing contact process for front junction *n*-type silicon solar cells.

The paste ingredients are also crucial to obtain a high aspect ratio, good conductivity and low contact resistance. For front junction *n*-type silicon solar cells, the paste for front contact gridlines (typically named Al/Ag paste) is different from the one for rear contact gridlines (typically named Ag paste), because a proper fraction of Al in the paste can dramatically reduce the contact resistance on the p^+ emitter [33]. Glass frits containing lead oxide (PbO) are essential for both pastes to etch through the ARC and passivation stacks to promote the adhesion of Ag contact to silicon. Organic binders are also important to ensure the continuity of and the high aspect ratio of screen-printed gridlines [34].

Figure 11 shows an example of firing-temperature profile, including the firing-temperature ramp up and ramp down. During this firing step in a conveyor belt furnace at a peak temperature of over 700°C, the metal contact is formed on both sides (p^+ emitter, and n^+ back surface field), which is the so-called co-firing process. Due to the different paste ingredients and the different doping profiles on the front and back, the firing parameter settings have to be optimized to achieve an optimum cell performance, including the conveyor speed and temperature ramp up/down.
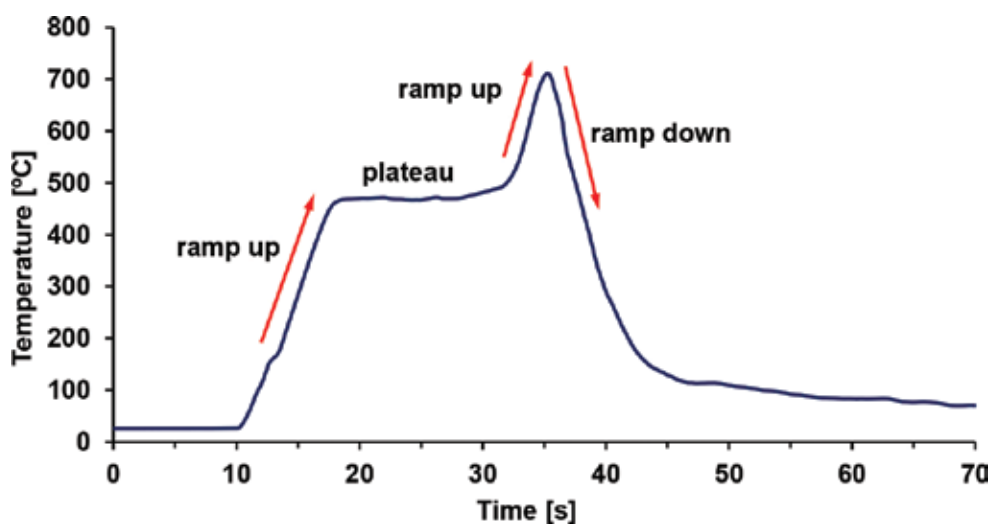
Figure 11. A typical firing-temperature profile for front junction *n*-type silicon solar cells.
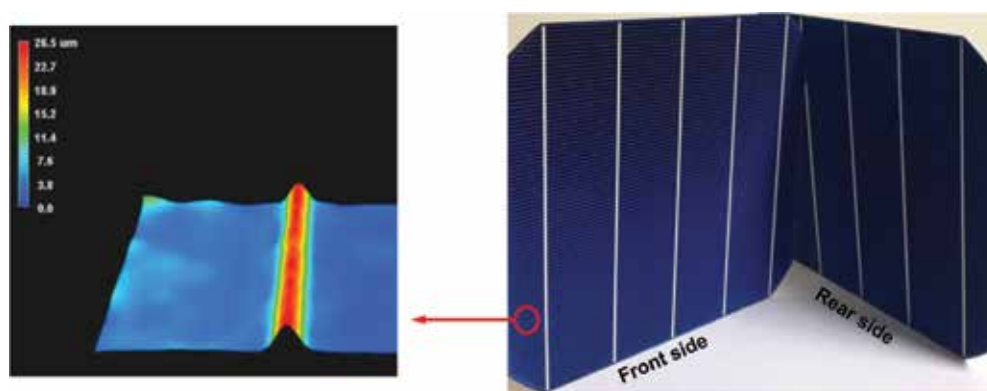

Figure 12. Optical microscope false colour height image of a screen-printed gridline (a); a large-area (~239 cm^2) front junction *n*-type silicon solar cell with screen-printed contact on both sides, featuring 5 bus-bars (b).

During the firing process, organic binders are burned out below 600°C, which typically occurs during the plateau stage as shown in **Figure 11**. In the higher-temperature zones of the furnace, including the peak firing temperature, both the front and rear contacts are simultaneously formed by etching through the ARC and passivation layers, Ag particle sintering, and forming the ohmic contact [35]. In the meantime, the hydrogen of the SiN$_x$:H ARC layer is released into the wafer to passivate electrical defects at interfaces and in the wafer bulk regions. The duration of the peak temperature often only lasts for a few seconds. **Figure 12b** shows the physical appearance of a finished cell with screen-printed contacts, featuring 5 bus-bars on both front

and rear sides. The final gridline on the cell is typically ~60 μm wide, and ~20 μm high, as shown in optical microscope image of **Figure 12a**.

3.6. Characterization

After cell fabrication, the illuminated current density–voltage (*J–V*) characteristic is measured by using an IV tester with a solar simulator with a light intensity of 1000 W/m², AM1.5 spectrum, and temperature of 25°C. This light *J–V* measurement determines important solar cell parameters, such as, V_{oc}, J_{sc}, *FF*, *n*-factor, R_s, R_{sh}, and cell efficiency *η*. Excellent results on large-area screen-printed front junction *n*-type silicon solar cells have been reported to date, with cell V_{oc} of ~665 mV, J_{sc} of 39.8 mA/cm², *FF* of 79.3%, and an efficiency of 21% [36]. For module application purposes, the cell's reverse breakdown characteristics are also determined to avoid hot-spot heating.

To obtain a better understanding of the loss mechanisms in a finished cell, detailed analysis is typically needed. For instance, a cell's internal and external quantum efficiency (*IQE* and *EQE*) and reflection are measured, as shown in **Figure 13**, including the illustration of optical and recombination losses. In addition, saturation current densities from each part of the
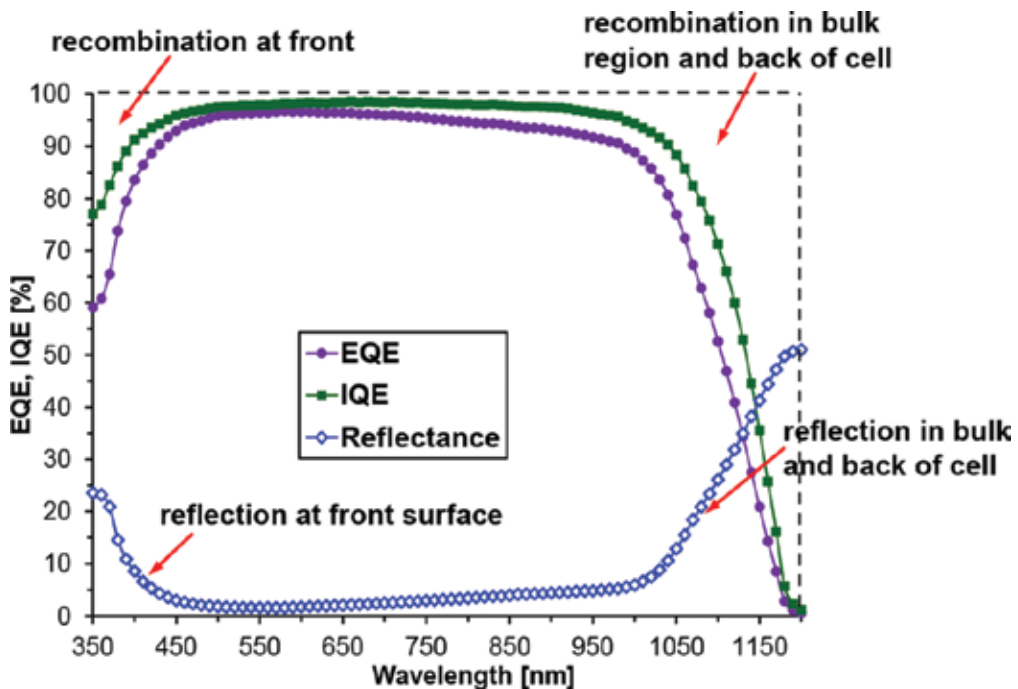

Figure 13. Typical internal and external quantum efficiency (*IQE* and *EQE*) and reflection in actual screen-printed front junction *n*-type silicon solar cells.

finished cell, as described by Eqs. (12)–(17), are also often extracted to quantitatively analyse these recombination losses.

4. Advanced cell concepts and fabrication

4.1. Selective doping

Due to the recent improvements in material quality and surface passivation, current high-efficiency silicon solar cells are often limited by the recombination at the metal/semiconductor contacts. A feasible solution to minimize contact recombination is a selectively doped structure, which allows decoupling of the metallized and non-metallized areas of the doped regions. **Figure 14** shows an example of a selective doping structure on the front emitter (p^+/p^{++}) and the back surface field (n^+/n^{++}). The higher surface doping concentration and the deeper doping profile underneath the screen-printed contact regions can result in lower contact resistance and lower metal-induced saturation current density ($J_{0e,contact}$ and $J_{0b,contact}$). In addition, the lower surface doping concentration on the non-metallized (passivated) regions can lead to lower saturation current density on the passivated regions ($J_{0e,pass}$ and $J_{0b,pass}$) due to less Auger recombination and better surface passivation quality. Consequently, the selective doping structure results in higher J_{sc} and V_{oc}.
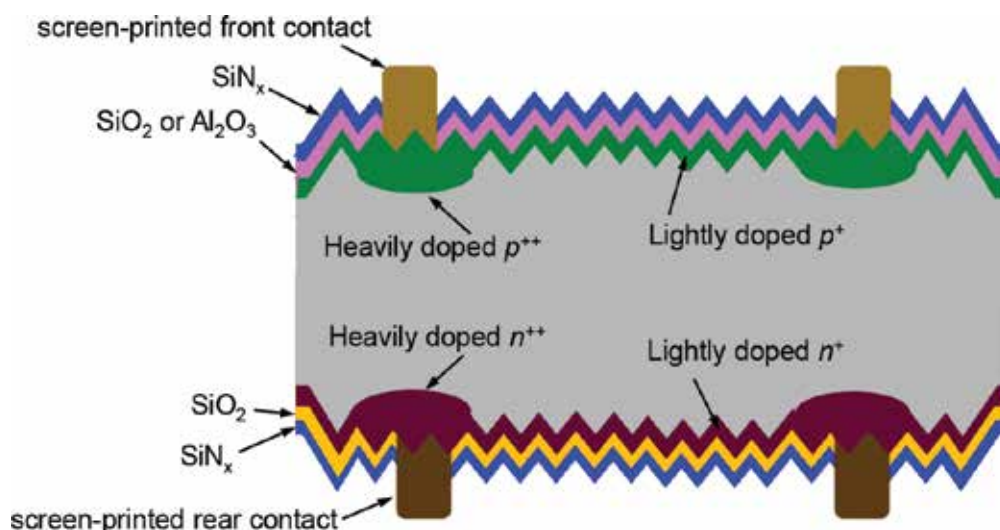

Figure 14. Schematic of selective doping for a screen-printed front junction n-type silicon solar cell.

There are several selective doping technologies that have been developed over years in the field of photovoltaics. One of these promising technologies is based on ion implantation through a mask which only increases the dopant dose on the regions underneath the screen-printed contacts. The advantages of this technology are eliminating the formation of PSG and/

or BSG, and fewer process steps. Other selective doping technologies, such as the etch-back process, laser-doping, oxide mask process, etc., have been addressed by Hahn, et al. [37]. As a rule of thumb, in order to implement these selective doping technologies to an industrial production line, every extra process step should provide the enhancement in cell efficiency of 0.2–0.3% absolute considering the related extra manufacturing costs.

4.2. Tunnel oxide passivated contact

Another feasible solution to minimize contact recombination is to put a passivating material with offset bands between the metal and silicon, also known as a passivated contact. Introduction of a thin passivating interlayer between the high recombination regions and the silicon absorber mitigates their negative impact because they are not in direct contact with the absorber. This reduces total recombination or saturation current density ($J_{0,total}$), resulting in much higher V_{oc}. However, the interlayer must passivate the silicon surface without interfering with the majority carrier transport to ensure good fill factor FF and efficiency. The best example of a passivated contact is the heterojunction silicon solar cell with an intrinsic thin amorphous layer (HIT), which has demonstrated cell V_{oc} of 750 mV [38] and cell efficiency of over 25% [39]. However, this passivation scheme cannot withstand temperature above 250°C for the back-end metallization process; hence, it is not compatible with the widely used industry standard simple and reliable screen-printed and fired-through metallization, which requires a temperature over 700°C for contact formation.

A promising approach to achieving a carrier selective passivated contact involves an ultra-thin (~15 Å, see the TEM image in **Figure 15b**) tunnel oxide capped with phosphorus doped n^+ polycrystalline silicon (*poly*-Si) and metal on the entire back side of *n*-type silicon cell (see **Figure 15a**), which is the so-called tunnel oxide passivated contact (TOPCON) [40]. This passivation scheme is thermally stable and so compatible with screen-printed and fired-through metallization. In this passivated contact structure as shown in its band diagram of **Figure 15b**, three parallel mechanisms contribute to carrier selectivity. First, heavily doped n^+ *poly*-Si creates an accumulation layer at the absorber surface due to the work function difference between the n^+ *poly*-Si and the n^- silicon absorber. This accumulation layer or band bending provides a barrier for holes to flow to the tunnel oxide, while electrons can migrate easily to the oxide/silicon interface. Second, the tunnel oxide itself provides the second level of carrier selectivity, because it presents a 4.5 eV barrier for holes to tunnel through relative to 3.1 eV for electrons [41], which is also the most important carrier selectivity feature [42]. Third, there are very few or no states on the other side of the dielectric (n^+ region) for holes to tunnel through because of the forbidden gap. Furthermore, due to the full area metal contact on the back, there is only one-dimensional current flow, which eliminates the lateral transport resistance (two-dimensional current flow) in a finished solar cell, and so results in much higher FF. By optimizing the depositions conditions of the *poly*-Si and the tunnel oxide growth temperature in nitric acid (HNO_3), excellent interface passivation quality and carrier selectivity can be achieved. For instance, a back saturation current density $J_{0b,pass}$ of less than 5 fA/cm^2 [43], and a cell efficiency of ~21.4% for large-area front junction *n*-type silicon solar cells with screen-

printed contact on an homogeneous emitter have been demonstrated (as shown in **Figure 15a**) [44].
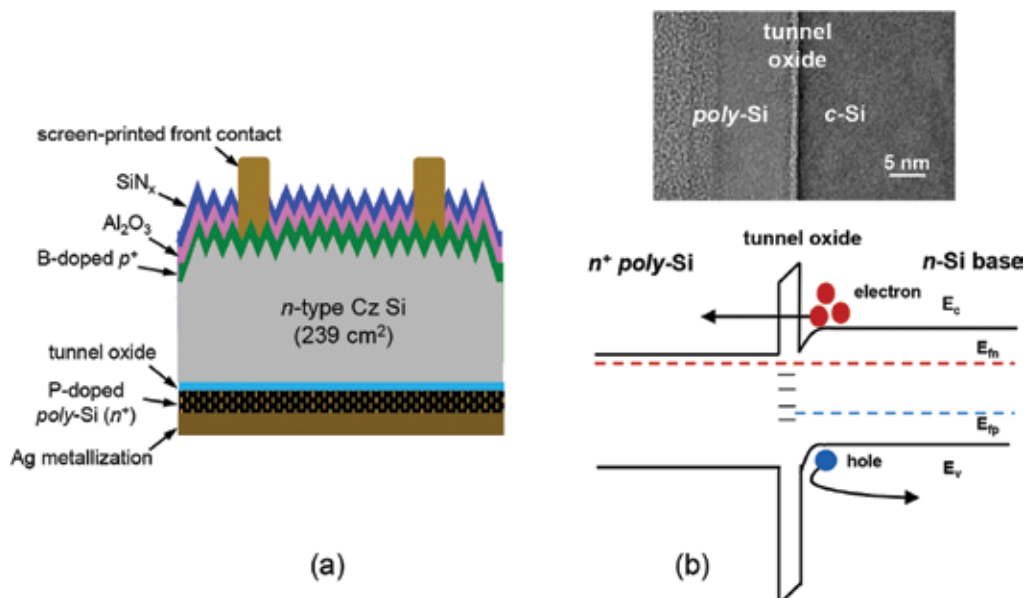

Figure 15. Schematic structure of a front junction *n*-type silicon solar cell with tunnel oxide passivated rear contact (a); a transmission electron microscopy (TEM) image of tunnel oxide passivated contact structure and its schematic band diagram (b) [42, 44].

5. Summary and outlook

The annual shipment and installation of PV cells and modules up to date are still dominated by the standard industrial solar cell fabrication process on *p*-type silicon wafers (full Al-BSF). However, screen-printed front junction *n*-type silicon solar cells featuring bifacial structure are attracting more and more interest, due to their potential for higher efficiency, higher-energy yield, and hence lower LCOE (levelized cost of electricity). The next few years promise to be an exciting timeframe for research and development of screen-printed front junction *n*-type silicon solar cells, which are also predicted in the latest Internal Technology Roadmap for Photovoltaic (ITRPV) [45].

Although it is hard to exactly predict which process approach and cell architecture will be the most cost-effective in the future, selective doping and tunnel oxide passivated contacts have become active areas of investigation for silicon solar cells, because they can produce higher cell efficiency due to reduced minority carrier recombination. Combining these two promising technologies into a screen-printed front junction *n*-type silicon solar cell may attract even more research investigation in the future. For instance, by applying atomic hydrogenation process,

boron-diffused selective front emitter and photolithographically defined front metal contacts (Ti/Pd/Ag), the TOPCON cell has successfully demonstrated over 25% efficiency on a small-area *n*-type float zone (FZ) silicon substrate [46, 47]. So, this cell structure explores research areas for future industrial application with screen-printed front contacts (as shown in **Figure 16**), due to its potential for high cell efficiency and its compatibility with high-temperature firing contact formation process.
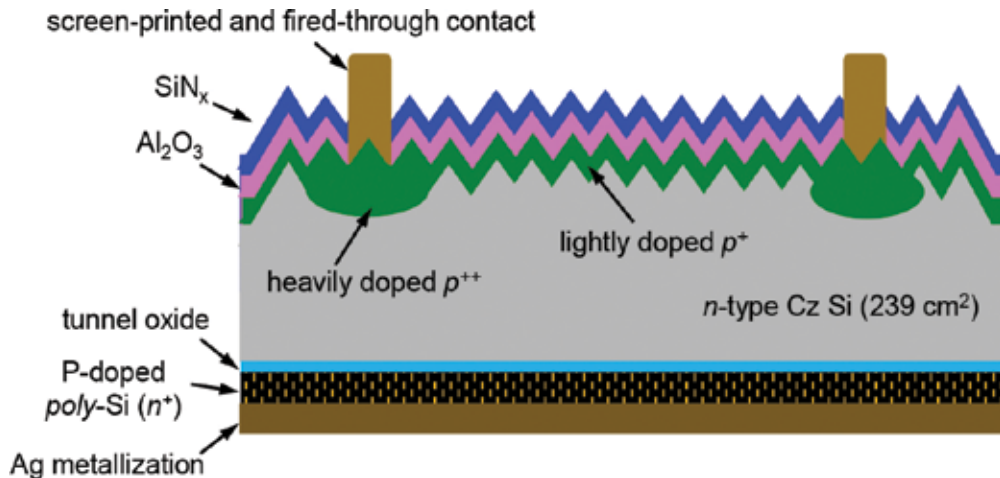

Figure 16. Schematic structure of a front junction *n*-type silicon solar cell (not to scale), with screen-printed and fired-through contact on a selectively doped front emitter, and tunnel oxide passivated rear contact.

Acknowledgements

Author details

Yuguo Tao[*]

Address all correspondence to: yuguo.tao@ece.gatech.edu

School of Electrical and Computer Engineering, Georgia Institute of Technology, Atlanta, Georgia, USA

References

[1] Hahn G, Joos S. State-of-the-art industrial crystalline silicon solar cells. In: Semiconductors and Semimetals; G.P. Willeke and E.R. Weber, Eds, 1st ed. San Diego, CA, USA: Academic, 2014, vol. 90, pp. 1–62.

[2] Macdonald D and Geerligs L J. Recombination activity of interstitial iron and other transition metal point defects in p-and n-type crystalline silicon. Applied Physics Letters. 2004;85(18):4061–4063.

[3] Glunz SW, Rein S, Lee JY, Warta W. Minority carrier lifetime degradation in boron-doped Czochralski silicon. Journal of Applied Physics. 2001;90(5):2397–2404.

[4] Zhao J, Wang A, Altermatt P P, Green M, Rakotoniaina J P & Breitenstein O. High efficiency PERT cells on n-type silicon substrates. In: 29th IEEE Photovoltaic Specialists Conference; May 2002; pp. 218–221.

[5] Green M G. Solar cells: operating principles, technology, and system applications. Englewood Cliffs, NJ: Prentice-Hall, Inc.; 1982. 288 p.

[6] Shockley W, Queisser HJ. Detailed balance limit of efficiency of p–n junction solar cells. Journal of Applied Physics. 1961;32(3):510–519.

[7] Meier DL, Good EA, Garcia RA, Bingham BL, Yamanaka S, Chandrasekaran V, Bucher C. Determining components of series resistance from measurements on a finished cell. In: Photovoltaic Energy Conversion, Conference Record of the 2006 IEEE 4th World Conference; IEEE; Wailohoa, HI, USA 2006; pp. 1315–1318.

[8] Shockley W, Read WT, Jr. Statistics of the recombinations of holes and electrons. Physical Review. 1952;87(5):835.

[9] Hall RN. Electron-hole recombination in germanium. Physical Review. 1952;87(2):387.

[10] Sinton RA, Cuevas A. Contactless determination of current–voltage characteristics and minority-carrier lifetimes in semiconductors from quasi-steady-state photoconductance data. Applied Physics Letters. 1996;69(17):2510–2512.

[11] Altermatt PP. Models for numerical device simulations of crystalline silicon solar cells—a review. Journal of Computational Electronics. 2011;10(3):314–330.

[12] Feldmann F, Bivour M, Reichel C, Hermle M, Glunz SW. Passivated rear contacts for high-efficiency n-type Si solar cells providing high interface passivation quality and excellent transport characteristics. Solar Energy Materials and Solar Cells. 2014;120:270–274.

[13] Misiakos K, Tsamakis D. Accurate measurements of the silicon intrinsic carrier density from 78 to 340 K. Journal of Applied Physics. 1993;74(5):3293–3297.

[14] Richter A, Werner F, Cuevas A, Schmidt J, Glunz SW. Improved parameterization of Auger recombination in silicon. Energy Procedia. 2012;27:88–94.

[15] Seidel H, Csepregi L, Heuberger A, Baumgärtel H. Anisotropic etching of crystalline silicon in alkaline solutions: I. Orientation dependence and behavior of passivation layers. Journal of the Electrochemical Society. 1990; 137(11):3612–3626.

[16] Neuhaus DH, Münzer A. Industrial silicon wafer solar cells. Advances in OptoElectronics. vol. 2007 (2007):1–15.

[17] Kern W. The evolution of silicon wafer cleaning technology. Journal of the Electrochemical Society. 1990;137(6):1887–1892.

[18] Kern W. Cleaning solutions based on hydrogen peroxide for use in silicon semiconductor technology. RCA Review. 1970;31:187–206.

[19] Schiele Y, Fahr S, Joos S, Hahn G, Terheiden B. Study on boron emitter formation by BBr3 diffusion for n-type Si solar cell applications. In: 28th EU PVSEC; Paris, France: 2013.

[20] Werner S, Lohmuller E, Belledin U, Vlooswijk AHG, Naber RCG, Mack S, Wolf A. Optimization of BBr3 diffusion processes for n-type silicon solar cells. In: 31st European PVSEC; 14–18 September; Hamburg, Germany. 2015.

[21] Taniguchi K, Kurosawa K, Kashiwagi M. Oxidation enhanced diffusion of boron and phosphorus in (100) silicon. Journal of the Electrochemical Society. 1980;127(10):2243–2248.

[22] Rohatgi A, Meier DL, McPherson B, Ok YW, Upadhyaya AD, Lai JH, Zimbardi F. High-throughput ion-implantation for low-cost high-efficiency silicon solar cells. Energy Procedia. 2012;15:10–19.

[23] Hermle M, Benick J, Rüdiger M, Bateman N, Glunz SW. N-type silicon solar cells with implanted emitter. In: 26th European Photovoltaic Solar Energy Conference; Hamburg, Germany; 2011; pp. 875–878.

[24] Müller R, Benick J, Bateman N, Schön J, Reichel C, Richter A, Hermle M, Glunz SW. Evaluation of implantation annealing for highly-doped selective boron emitters suitable for screen-printed contacts. Solar Energy Materials and Solar Cells. 2014; 120:431–435.

[25] Peters S. Industrial diffusion of phosphorus n-type emitters for standard wafer-based silicon solar cells. Photovoltaics International. 2009;3:60–66.

[26] Wolf A, Kimmerle A, Werner S, Maier S, Belledin U, Meier S, Biro D. Status and perspective of emitter formation by POCl3-diffusion. In: 31st European PVSEC; 14–18 Sep; Hamburg, Germany. 2015.

[27] Tao Y, Ok YW, Zimbardi F, Upadhyaya AD, Lai JH, Ning S, Upadhyaya VD, Rohatgi A. Fully ion-implanted and screen-printed 20.2% efficient front junction silicon cells on 239 cm n-type CZ substrate. IEEE Journal of Photovoltaics. 2014;4(1):58–63.

[28] Lanterne A, Le Perchec J, Gall S, Manuel S, Coig M, Tauzin A, Veschetti Y. Understanding of the annealing temperature impact on ion implanted bifacial n-type solar cells to reach 20.3% efficiency. Progress in Photovoltaics: Research and Applications. 2015;23(11):1458–1465.

[29] Hoex B, Schmidt J, Bock R, Altermatt PP, Van de Sanden MC, Kessels WM. Excellent passivation of highly doped p-type Si surfaces by the negative-charge-dielectric Al_2O_3. Applied Physics Letters. 2007;91(11):112107.

[30] Dingemans G, Kessels WMM. Recent progress in the development and understanding of silicon surface passivation by aluminium oxide for photovoltaics. In: 25th European PVSEC; Valencia, Spain. 2010.

[31] Heavens OS. Optical properties of thin solid films. Courier Corporation; Dover, New York; 1991.

[32] Ralph EL. Recent advancements in low cost solar cell processing. In: 11th IEEE PVSC; Scottsdale. 1975. pp. 315–316.

[33] Ok YW, Upadhyaya AD, Zimbardi F, Tao Y, Cooper IB, Rohatgi A, Carroll AF, Suess T. Effect of Al content on the performance of Ag/Al screen printed N-type Si solar cells. In: 39th IEEE Photovoltaic Specialists Conference (PVSC); June 16; IEEE; Tampa, FL, USA 2013.

[34] Ballif C, Huljić DM, Willeke G, Hessler-Wyser A. Silver thick-film contacts on highly doped n-type silicon emitters: structural and electronic properties of the interface. Applied Physics Letters. 2003;82(12):1878–1880.

[35] Schubert G, Fischer B, Fath P. Formation and nature of Ag thick film front contacts on crystalline silicon solar cells. In: Proceedings of the Photovoltaic in Europe Conference; October 7; Rome, Italy; 2002; Vol. 343.

[36] Institute for Solar Energy Research in Hamelin (ISFH). Ion implanted, co-annealed and fully screen-printed bifacial n-type PERT solar cells with efficiencies of 21% and bifaciality factors exceeding 97% [Internet]. September 4, 2015. Available from: http://www.isfh.de

[37] Hahn G. Status of Selective Emitter Technology. In: 25th European Photovoltaic Solar Energy Conference and Exhibition/5th World Conference on Photovoltaic Energy Conversion; 6–10 September; Valencia, Spain; 2010; pp. 1091–1096.

[38] Taguchi M, Yano A, Tohoda S, Matsuyama K, Nakamura Y, Nishiwaki T, Fujita K, Maruyama E. 24.7% record efficiency HIT solar cell on thin silicon wafer. IEEE Journal of Photovoltaics. 2014;4(1):96–99.

[39] Masuko K, Shigematsu M, Hashiguchi T, Fujishima D, Kai M, Yoshimura N, Yamagu-chi T, Ichihashi Y, Mishima T, Matsubara N, Yamanishi T. Achievement of more than 25% conversion efficiency with crystalline silicon heterojunction solar cell. IEEE Journal of Photovoltaics. 2014;4(6):1433–1435.

[40] Feldmann F, Bivour M, Reichel C, Hermle M, Glunz SW. Passivated rear contacts for high-efficiency n-type Si solar cells providing high interface passivation quality and excellent transport characteristics. Solar Energy Materials and Solar Cells. 2014;120:270–274.

[41] Lee WC, Hu C. Modeling CMOS tunneling currents through ultrathin gate oxide due to conduction-and valence-band electron and hole tunneling. IEEE Transactions on Electron Devices. 2001;48(7):1366–1373.

[42] Tao Y, Upadhyaya V, Jones K, Rohatgi A. Tunnel oxide passivated rear contact for large area n-type front junction silicon solar cells providing excellent carrier selectivity. AIMS Materials Science. 2016;3(1):180–189.

[43] Tao Y, Chang EL, Upadhyaya A, Roundaville B, Ok YW, Madani K, Chen CW, Tate K, Upadhyaya V, Zimbardi F, Keane J, Rohatgi A. 730 mV implied Voc enabled by tunnel oxide passivated contact with PECVD grown and crystallized n+ polycrystalline Si. In: Photovoltaic Specialist Conference (PVSC), IEEE 42nd; June 14; New Orleans; 2015.

[44] Tao Y, Upadhyaya V, Huang Y, Chen C, Jones K, Rohatgi A. Carrier selective tunnel oxide passivated contact enabling 21.4% efficient large-area n-type silicon solar cells. In: 43rd IEEE Photovoltaic Specialists Conference; June 5; Portland, Oregon; 2016.

[45] ITRPV. International Technology Roadmap for Photovltaic Results 2014_Rev.1 [Internet]. July 2015. Available from: http://www.itrpv.net/Reports/Downloads/2015/

[46] Hermle M, Feldmann F, Eisenlohr J, Benick J, Richter A, Lee B, Stradins P, Rohatgi A, Glunz SW. Approaching efficiencies above 25% with both sides-contacted silicon solar cells. In: Photovoltaic Specialist Conference (PVSC), 2015 IEEE 42nd; June 14; pp. 1–3.

[47] Glunz S, Feldmann F, Richter A, Bivour M, Reichel C, Benick J, Hermle M. The irresistible charm of a simple current flow pattern approaching 25% with a solar cell featuring a full-area back contact. In: Proc. 31h Europ. Photovolt. Sol. Energy Conf., Hamburg, Germany, 2015 Sep 14.

Efficient Optical Modulation of Terahertz Transmission in Organic and Inorganic Semiconductor Hybrid System for Printed Terahertz Electronics and Photonics

Tatsunosuke Matsui, Keisuke Takano, Makoto Nakajima and Masanori Hangyo

Additional information is available at the end of the chapter

Abstract

Highly efficient optical modulation of terahertz (THz) transmission through Si substrate coated with thin layer of organic π-conjugated materials was investigated under various laser light irradiation conditions using THz time-domain spectroscopy. As in the pioneering work by Yoo et al. [Yoo et al., Applied Physics Letters. 2013;103:151116-1–151116-3.], we also used copper phthalocyanine (CuPc). It was perceived that the charge carrier transfer from Si to CuPc is crucial for the photo-induced metallization and efficient optical modulation of THz transmission. We found that the thickness of CuPc layer is a critical parameter to realize high charge carrier density for efficient THz transmission modulation. We also fabricated a split-ring resonator (SRR) array metamaterial on CuPc-coated Si utilizing superfine inkjet printer and succeeded in obtaining efficient modulation of resonant responses of SRR array metamaterials by laser light irradiation. We have further investigated THz transmission modulation through Si substrates coated with another four solution-processable π-conjugated materials. Two of them are π-conjugated low molecules such as the [6,6]-phenyl-C61-butyric acid methyl ester (PCBM) and 6,13-bis(triisopropylsilylethynyl) pentacene (TIPS-pentacene), and another two are the π-conjugated polymer materials such as poly[5-(2-ethylhexyloxy)-2-methoxycyanoterephthalyliden] (MEH-CN-PPV) and poly(benzimidazobenzophenanthroline) (BBL). Among these four π-conjugated materials, PCBM- and TIPS-pentacene showed better modulation efficiencies even higher than CuPc. Our findings may open the way to fabricating various types of THz active devices utilizing printing technologies.

Keywords: π-conjugated material, solution process, terahertz, metamaterial, terahertz time-domain spectroscopy

1. Introduction

Wide range of electromagnetic waves from radio waves, microwaves to infrared, visible, and ultraviolet has been widely utilized in wide variety of applications such as lightings, displays, information and communications technology (ICT), spectroscopies, and microscopes. Among these frequency ranges, terahertz (THz) frequency range has not been explored much compared to other frequency ranges. However, researches on THz science and technologies have made significant progress in recent years [1, 2]. THz frequency range lies in between microwave and infrared as schematically shown in **Figure 1** and can be utilized for various types of applications such as spectroscopy, nondestructive inspection, security, and ICT. For wider spread usage of THz technologies, development of useful optical devices is demanded.
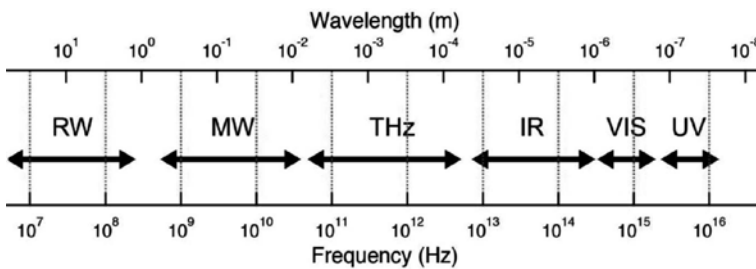

Figure 1. Frequency ranges of electromagnetic waves. RW, MW, THz, IR, VIS, and UV stand for radio waves, microwaves, terahertz, infrared, visible, and ultraviolet, respectively.

To develop active THz devices such as active filters, modulators, and imagers, numerous attempts have been made to modulate THz radiation by external stimuli such as optical, electrical, and thermal stimuli [2–4]. For such purposes, inorganic semiconductor substrates, such as Si [5–8], GaAs [9], and InSb [10], have been widely used since sufficient amounts of free carriers for modulation of THz transmission can easily be obtained by light irradiation (**Figure 2(a)**) or thermal heating. Recently, Yoo et al. reported that depositing a thin layer of organic π-conjugated material, copper phthalocyanine (CuPc) on Si substrate is quite effective to enhance an efficiency of the photo-induced modulation of the THz transmission through it [11–13]. The molecular structure of CuPc is shown in **Figure 2(b)**. They have shown that the THz transmission through CuPc-coated Si substrate decreases under low-power (tens of mW) continuous-wave (CW) laser light irradiation (**Figure 2(c)**) [11]. When only Si substrate was used, or when CuPc was deposited on a quartz substrate instead of on Si, no remarkable modulation was obtained [11]. The authors infer that this is caused by a charge transfer from Si to CuPc. It is impossible to create free charge carriers in CuPc directly via photo-excitation. This is because Frenkel-type tightly bound electron–hole pairs (excitons) are formed, which cannot be dissociated easily due to the strong exciton binding energy typical in organic π-conjugated materials with low dielectric permittivity. Therefore, the interface between organic and inorganic semiconductors should play a crucial role in the modulation mechanism. Free charge carriers should be created in Si by laser light irradiation, and these charge carriers move into thin layer of CuPc. Yoo et al. also showed that optical THz modulation could be induced
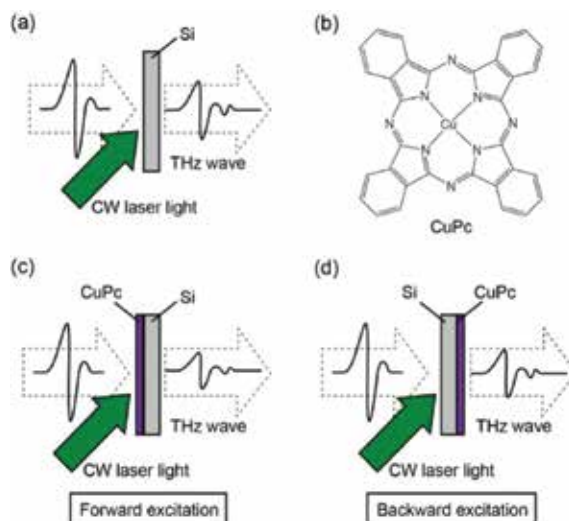
Figure 2. Schematic representation of optical modulation of THz transmission. (a) in Si substrate and (b) molecular structure of CuPc. Efficient optical modulation of THz transmission in Si substrate coated with thin layer of CuPc in (c) forward and (d) backward excitation configurations.

by backward excitation, that is, excitation from the Si substrate (**Figure 2(d)**) [12]. This technique is suitable for materials that show strong absorption at the wavelength of exciting laser light.

Here, we show that the thickness of the organic semiconductor thin film is the crucial parameter for obtaining a high carrier density for metallization and a higher THz transmission modulation [14].

To utilize metamaterials, which show exotic functionality not found in natural materials, is also actively studied for use in developing active THz devices [15–18]. The subwavelength resonant structures such as split-ring resonators (SRRs) can resonantly interact even with magnetic field of electromagnetic waves and give various types of novel functionalities. We also demonstrated that the CuPc/Si system could be used to efficiently control THz resonant responses of SRR array metamaterials that is also fabricated by printing technology [14].

Several groups showed that other types of π-conjugated materials could be used instead of CuPc such as pentacene and C60 [19], poly[2-methoxy-5-(2-ethylhexyloxy)-1,4-phenylenevinylene] (MEH-PPV) [20], various phthalocyanine compounds [21], and 6,13-bis(triisopropylsilylethynyl) pentacene (TIPS-pentacene) [22]. Zhang et al. also succeeded in obtaining highly efficient optical modulation using organometal halide perovskite deposited on Si [23]. Here, we show that various types of organic semiconductors with solution processability can also be utilized for the optical modulation of THz radiation [24]. In this study, the following four soluble organic π-conjugated materials were investigated. Molecular structures of these materials are summarized in **Figure 3**. Two of them were low molecules: a well-known fullerene derivative electron acceptor, [6,6]-phenyl-C61-butyric acid methyl ester (PCBM)
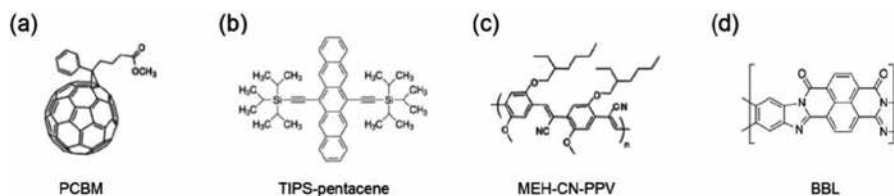
Figure 3. Molecular structures of π-conjugated materials used in this study. (a) [6,6]-phenyl-C61-butyric acid methyl ester (PCBM), (b) 6,13-bis(triisopropylsilylethynyl) pentacene (TIPS-pentacene), (c) poly[5-(2-ethylhexyloxy)-2-methoxycyanoterephthalyliden] (MEH-CN-PPV), and (d) poly(benzimidazobenzophenanthroline) (BBL).

(**Figure 3(a)**) [25–27], and 6,13-bis(triisopropylsilylethynyl) pentacene (TIPS-pentacene) (**Figure 3(b)**), which is extensively studied as an active layer of organic thin-film transistors [28, 29]. The other two materials were π-conjugated polymer materials: n-type semiconductor, poly[5-(2-ethylhexyloxy)-2-methoxycyanoterephthalyliden] (MEH-CN-PPV) (**Figure 3(c)**) [30], and poly(benzimidazobenzophenanthroline) (BBL) (**Figure 3(d)**), which is known as a π-conjugated double-stranded (ladder) polymer with quite a high electron mobility of 0.1 cm^2 V^{-1} s^{-1} [31, 32]. Efficient optical modulation of THz transmission in these solution-processable π-conjugated materials may open the way for printed THz electronics and photonics.

2. Experiment

2.1. Sample preparation

We used a 540-μm-thick, highly resistive Si (>2.0 × 10^4 Ωcm, Optostar Ltd.) that is transparent to THz wave as a substrate. We purchased copper(II) phthalocyanine (β-form powders) from Sigma-Aldrich and used without purification. A thin film of CuPc was deposited by thermal evaporation and subsequently annealed at 250°C to obtain highest modulation, as reported by Yoo et al. [13]. We also used another solution-processable π-conjugated materials, PCBM, TIPS-pentacene, MEH-CN-PPV, and BBL, and these four materials were purchased from Sigma-Aldrich and used without purification [24]. As solvents for solution processes, toluene was used for PCBM and TIPS-pentacene, and chloroform was used for MEH-CN-PPV. To form thin films, spin-coating were used and these films were subsequently thermally annealed at 250°C. BBL thin films were formed using methanesulfonic acid (MSA) as solvent. BBL thin films were spin-coated and immersed in deionized water to remove any remaining MSA solvent following a reported recipe to facilitate aggregation and crystallization [31, 32]. Since BBL thin films easily peel off from the substrate when they are immersed in water, special care has to be taken [24].

We also used printing technology to fabricate SRR array metamaterials. We have utilized a superfine inkjet printer (SIJ printer, SIJTechonology, Inc.) [33–36] to draw a silver SRR array. The sample was subsequently annealed at 240°C. An SRR array with a total area of 5 × 5 mm^2 was fabricated. The dimensions of each SRR meta-atom were designed following

the design of Padilla et al. such that they showed resonant responses in the THz region [16]; therefore, the period (Λ), side length (L), width (W), and gap (G) were made to be 100, 60, 12, and 6 μm, respectively, as shown in **Figure 4(a)**. Such SRRs are known to show electric–magnetic-coupled resonance (ω_0) and half-wave resonance (ω_1) around 1 THz as schematically shown in **Figure 4(b)**.

2.2. THz time-domain spectroscopy measurements

The optical characteristics in the THz range were investigated using typical THz time-domain spectroscopy (THz-TDS) [37–39]. Typical setup and principle of data acquisition are schematically summarized in **Figure 5**. In our setup, photoconductive antennas were used for both generation and coherent detection of THz radiation. The samples were placed in between of two off-axis parabolic mirrors, which are used to collect, collimate, and focus the THz radiation and such that the THz beam was normally incident on the sample surface. For normalization purposes, we also measure reference spectra without placing the samples in the THz beam path as shown in **Figure 5(b)**. A unique feature of the THz-TDS is that it allows for a direct measurement of the transient electric field, so that both amplitude and phase information are obtained simultaneously. Obtained time-domain transient photocurrent responses are Fourier-transformed to evaluate frequency responses as shown in **Figure 5(c)**. We obtain frequency-domain sample response $E_{sam}(\omega)$ and reference $E_{ref}(\omega)$ as follows.

$$E_{sam}(t) \xrightarrow{\quad FT \quad} \left| E_{sam}(\omega) \right| \exp\left\{ i\theta_{sam}(\omega) \right\} \tag{1}$$

$$E_{ref}(t) \xrightarrow{\quad FT \quad} \left| E_{ref}(\omega) \right| \exp\left\{ i\theta_{ref}(\omega) \right\} \tag{2}$$

By taking a ratio of these frequency-domain responses, transmission coefficient $t(\omega)$ should be evaluated as follows.
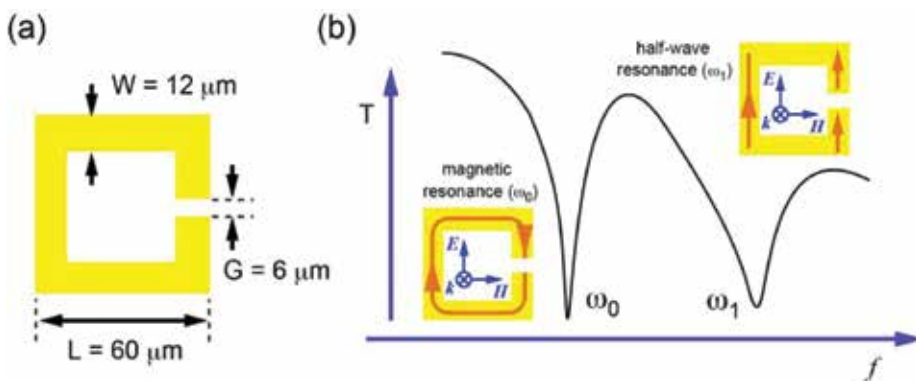

Figure 4. (a) Dimension of each SRR and (b) magnetic resonance and half-wave resonance of SRR array.
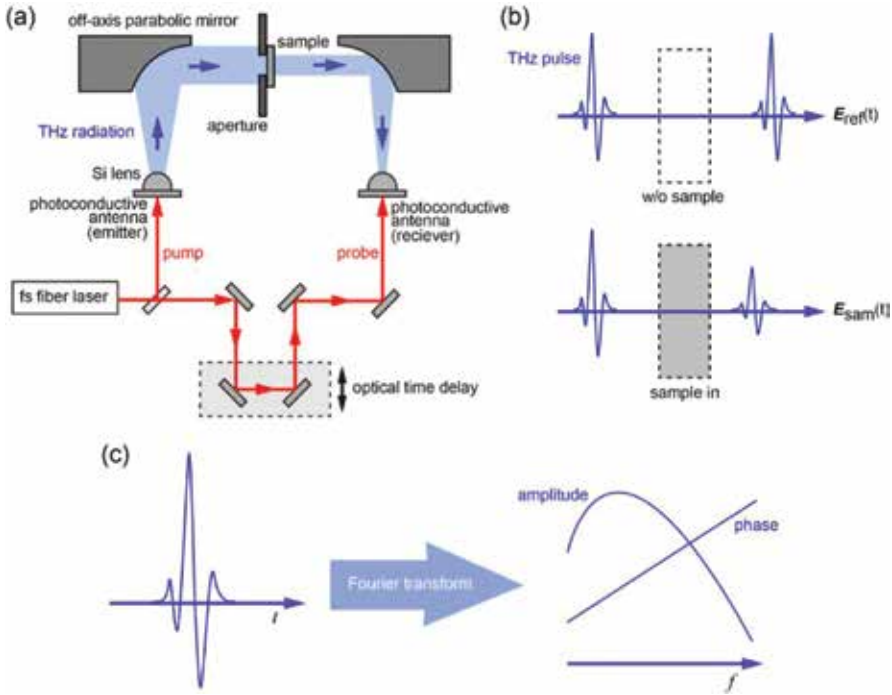
Figure 5. Schematic representation of THz-TDS measurements. (a) Typical setup, (b) time-domain measurements, and (c) retrieving frequency-domain responses by applying Fourier transform to time-domain signal.

$$t(\omega) = \frac{E_{sam}(\omega)}{E_{ref}(\omega)} = \frac{\left|E_{sam}(\omega)\right|}{\left|E_{ref}(\omega)\right|} \exp\left[i\left\{\theta_{sam}(\omega) - \theta_{ref}(\omega)\right\}\right] \tag{3}$$

The transmission coefficient $t(\omega)$ should also be written down with complex refractive indices; therefore, both real (n) and imaginary (κ) refractive indices spectra should be retrieved using amplitude and phase information in experimentally obtained transmission coefficiencies without the need for Kramers–Kronig analysis. We also obtained the complex dielectric constants and complex conductivities from known relations between them and the complex refractive index.

To perform the optical modulation experiment, a 532-nm CW laser (Spectra Physics, Millennia Vs) was used to optically generate free charge carriers in Si. At this wavelength, CuPc and PCBM do not show much absorption; thus, forward excitation configuration was employed, as shown in **Figure 2(c)**. In contrast, TIPS-pentacene, MEH-CN-PPV, and BBL show strong absorption at 532 nm; therefore, backward excitation configuration was used to avoid absorption in π-conjugated materials, as shown in **Figure 2(d)** [24]. A 3-mm-diameter aperture was placed in front of the sample to define the area illuminated by THz radiation.

To quantitatively evaluate the degree of optical modulation of THz transmission, we introduced following modulation factor (MF) of THz transmission:

$$MF = \frac{\int |E_{OFF}(\omega)|^2 d\omega - \int |E_{ON}(\omega)|^2 d\omega}{\int |E_{OFF}(\omega)|^2 d\omega} \tag{4}$$

where $E_{OFF}(\omega)$ and $E_{ON}(\omega)$ are the field amplitudes of the transmitted THz radiation when the CW laser is off and on, respectively. The integration in Eq. (4) was performed over a frequency range from 0.2 to 1.5 THz. A higher MF means a larger drop in THz transmission by CW laser light irradiation [14].

The photo-induced change of the THz responses of SRR array was investigated using the same THz-TDS system. The electric field of the linearly polarized THz radiation is made to be perpendicular to the SRR gap, so that magnetic resonance can be initiated as schematically shown in **Figure 4(b)** [16].

3. Results and discussions

3.1. Efficient optical modulation of THz transmission in Si substrate coated with thin layer of CuPc

In **Figure 6(a)**, the transmitted THz power spectra without laser light irradiation are shown for the bare Si substrate and Si coated with CuPc of different thicknesses of 50, 100, 200, 300, and 500 nm, respectively. There is no significant difference in transmitted power between the bare Si and CuPc-coated Si. In **Figure 6(b)**, the THz transmission spectra of the same samples under laser light irradiation with an intensity of 2.5×10^3 mW/cm^2 are shown. Upon laser light irradiation, the THz transmission decreases to almost zero, especially in CuPc thinner than 200 nm. However, the transmission modulation becomes smaller when the thickness of CuPc is further increased. In **Figure 6(c)**, the MF of the THz transmission is summarized as a function of CuPc film thickness. Without the CuPc film, MF is around 0.54. On the contrary, MF increases drastically to almost unity by depositing a CuPc film thinner than 200 nm. However, MF decreases again with further increasing CuPc thickness and becomes almost the same as without the CuPc film. The charge carrier transfer from Si to CuPc play a crucial role in the THz transmission modulation. Since the absorption coefficient of Si at 530 nm is 7850 cm^{-1} [40], the optical excitation of free charge carriers should occur at the surface (interface) of the Si to a skin depth of micrometers. The bended energy band relationship at the interface drives the free charge carriers to move towards the Si/CuPc interface and transfer into the CuPc layer. When the CuPc layer is thin enough, the charge carrier density increases after being transferred to the CuPc layer and shifts the plasma frequency to a frequency high enough to show metallic characteristics in the THz spectral range. This concentration effect of the transferred free charge carriers in the thin CuPc layer might be the major contribution in the metallization of CuPc, which agrees well with the CuPc thickness dependence of MF shown in **Figure 6(c)**. On the

contrary, when thicker CuPc films were deposited, the CuPc behaves as a dielectric due to the relatively low charge carrier density and therefore becomes more transparent and the MF decreases.

Figure 6(d) shows the transmitted THz power spectra through CuPc-coated Si under different laser light irradiances. The thickness of the CuPc film was 200 nm. With increasing laser light intensity, the THz transmission decreases gradually and drops to approximately zero at 2.5×10^3 mW/cm^2. **Figure 6(e)** shows the normalized transmission spectra under each laser light intensity. Each spectrum is normalized to those with no laser irradiation. The THz transmission modulation is more remarkable at lower frequencies. In **Figure 6(f)**, the MF in Si coated with 200-nm-thick CuPc and bare Si are summarized as a function of laser intensity. The MF is drastically enhanced by the deposition of a 200-nm CuPc film. These results clearly indicate that the THz transmission modulation can be enhanced easily by a simple deposition of a thin CuPc film.
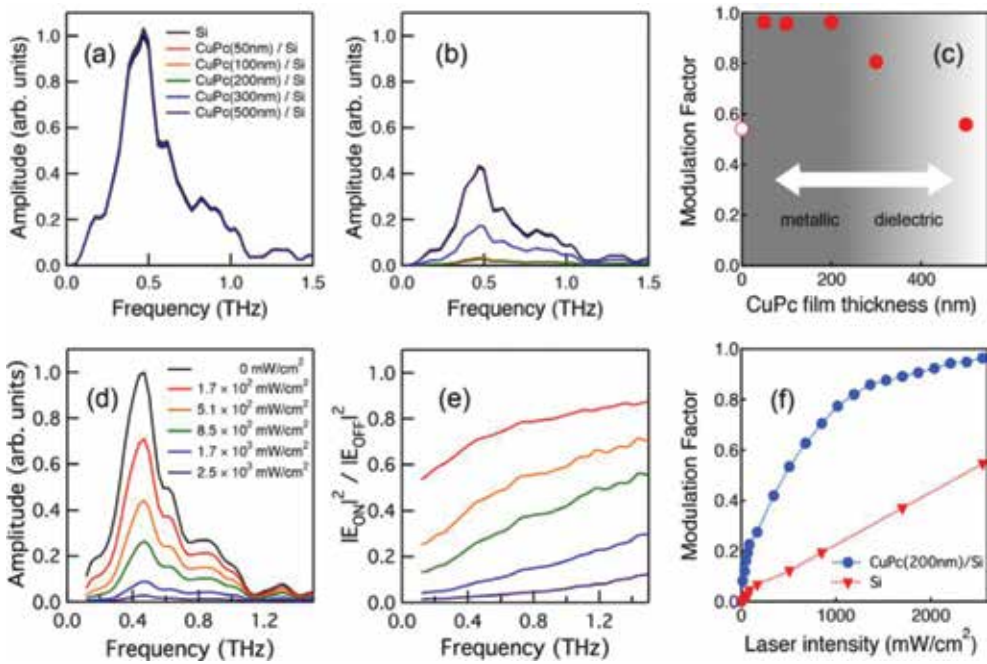

Figure 6. Summary of optical modulation of THz transmission experiment in CuPc-coated Si substrate. THz transmission spectra through a bare Si substrate and Si coated with thin CuPc films of different thicknesses (a) without and (b) with a laser light irradiation of 2.5×10^3 mW/cm^2. (c) CuPc film thickness dependence on the MF for THz transmissions. THz transmission spectra through a 200-nm CuPc film on a Si substrate (d) under different laser light irradiances and (e) those of normalized with THz transmission spectra without laser irradiation. (f) The laser intensity dependence of the MF for THz transmission through a bare Si substrate and Si coated with a 200-nm CuPc film.

In order to investigate further the underlying physical mechanism of the enhanced modulation efficiency of the THz transmission, we compare the dielectric properties of bare Si and CuPc-
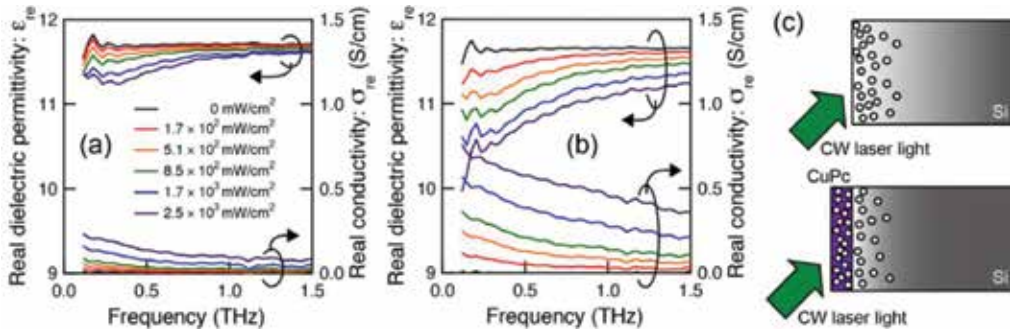
Figure 7. Real dielectric permittivity (ε_{re}) and real conductivity (σ_{re}) spectra under different laser light irradiances of (a) a bare Si substrate and (b) a Si substrate coated with a 200-nm CuPc film analyzed as a composite. (c) Schematic representation of photo-induced charge carrier distribution in a bare Si and a Si substrate coated with a 200-nm CuPc film under laser light irradiation.

coated Si under different laser light irradiation conditions. **Figure 7(a)** shows real dielectric permittivity (ε_{re}) and the real conductivity (σ_{re}) spectra of a bare Si substrate, and **Figure 7(b)** shows corresponding spectra for a 200-nm CuPc film on a Si substrate under different laser light irradiances. We have analyzed CuPc-coated Si as a single-layer composite material, because we think the THz dielectric characteristics of CuPc/Si two-layer system cannot be analyzed separately. In order to analyze them separately, we first need to have dielectric characteristics of bare Si with separate experiment. However, as schematically shown in **Figure 7(c)**, when Si is coated with thin layer of CuPc, the density of charge carrier in the Si upon CW laser light irradiation condition should be different from that of bare Si. Therefore, the THz response of the Si side of CuPc-coated Si should be different from that of the bare Si substrate. This is the reason why we have analyzed CuPc-coated Si as a single-layer composite material [14].

Without laser irradiation, the dielectric response shows almost no dispersion and almost the same value with and without the CuPc film as shown in **Figure 7(a)** and **(b)**. However, with increasing laser light intensity, the real dielectric permittivity decreases especially at lower frequencies, which can be attributed to a Drude-like metallic response. This may explain why higher modulation was obtained for lower frequencies as shown in **Figure 6(e)** [14]. Although the thickness of CuPc is <0.5% of that of Si, the change in the dielectric response by CW laser light irradiation is remarkable in CuPc-coated Si. This implies that the contribution from thin CuPc layer to the dielectric property is quite large; therefore, the change in the dielectric permittivity of the CuPc layer should be much larger than it appeared. It may be reasonable to expect that the permittivity drops to negative values, like in a Drude-like response. The change in real conductivity by CW laser light irradiation is also remarkable in CuPc-coated Si, and the real conductivity in CuPc layer should also be much higher than it appeared under laser light irradiation. The significant increase in conductivity by CW laser light irradiation also supports that CuPc-coated Si becomes more conductive [14].
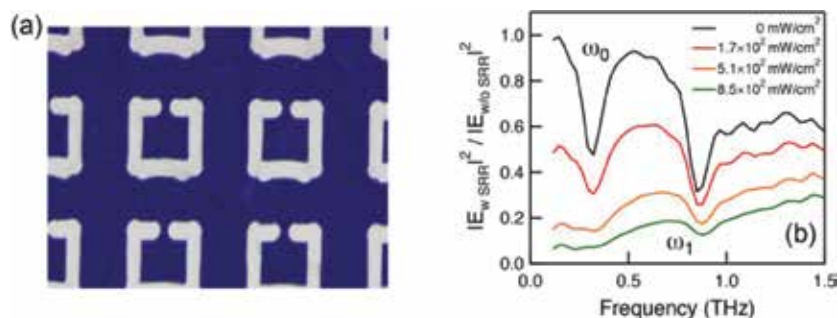
Figure 8. (a) Laser microscope image of the fabricated Ag SRR array on a 200-nm CuPc film on a Si substrate. (b) Normalized THz transmission spectra under different laser light irradiances through the SRR array fabricated on a 200-nm CuPc film on a Si substrate.

3.2. Efficient optical modulation of THz resonant responses in printed SRR array on Si substrate coated with thin layer of CuPc

We have applied efficient optical modulation of THz transmission through the Si substrate coated with thin film of CuPc to the optical modulation of SRR metamaterial responses. We fabricated SRR array on CuPc-coated Si by using superfine inkjet printer. **Figure 8(a)** shows a laser microscope image of the fabricated silver SRR array. **Figure 8(b)** shows the normalized THz transmission spectra of it under different laser light irradiances. When the laser light is off, sharp transmission dips induced by resonant interaction with the SRRs can be recognized. The dip in transmission at the lower (ω_0 ~0.32 THz) and higher (ω_1 ~0.85 THz) frequencies could be attributed to the electric–magnetic-coupled resonance and the half-wave resonance, respectively (**Figure 4(b)**) [16]. As the laser light intensity is increased, the transmission drops in all frequencies of interest and almost no features can be recognized at higher laser light intensities. The efficient metallization in CuPc-coated Si by CW laser light irradiation is enough to short the capacitive gap of the SRR and erase its resonant effect [14]. For more efficient modulation at particular frequencies, CuPc should be partially coated only on the capacitive gap of the SRR, for example.

3.3. Efficient optical modulation of THz transmission in Si substrate coated with thin layer of solution-processable π-conjugated materials

We have further investigated optical modulation characteristics of THz transmission in Si substrate coated with thin layer of solution-processable π-conjugated materials. In **Figure 9**, MF of the THz transmission through Si substrates coated with four different π-conjugated materials, PCBM, TIPS-pentacene, MEH-CN-PPV, and BBL, are summarized as a function of laser intensity. Those of CuPc are also shown for comparison. Since the modulation efficiency is not the same for different ways of excitations (forward or backward excitations) [12], in **Figure 9(a)** and **(b)**, we summarize our data separately for forward and backward excitations, respectively. In all the samples, a significant increase in MF was obtained upon illumination with the CW laser light. Among these, PCBM and TIPS-pentacene are more efficient than CuPc;
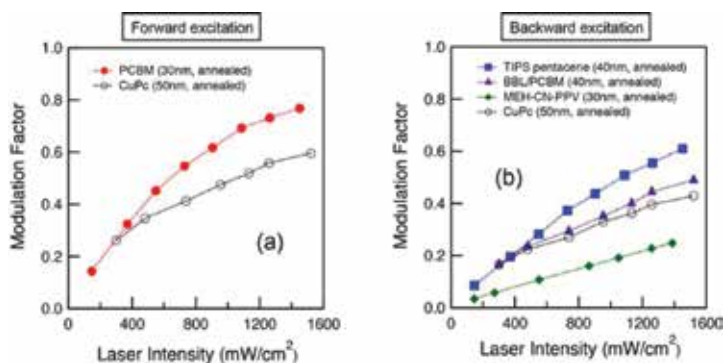
Figure 9. Summary of the laser intensity dependence of the MF of THz transmission in the (a) PCBM and CuPc with forward excitation and (b) TIPS-pentacene, BBL/PCBM, MEH-CN-PPV, and CuPc with backward excitation.

therefore, PCBM and TIPS-pentacene are more useful not only from the viewpoint of the fabrication process but also modulation efficiency. In these two materials, it was also found that thermal annealing was effective in further increasing MF (data are not shown).

4. Conclusions

In conclusions, we have analyzed the optical modulation characteristics of THz transmission in Si substrate coated with organic π-conjugated materials under various laser light irradiation conditions using THz-TDS. The charge carrier transfer from Si to organic π-conjugated materials plays crucial role for the photo-induced metallization of Si coated with organic π-conjugated materials, and it was shown that the thickness of the organic layer is a critical parameter to realize higher modulation efficiency. We have also fabricated SRR array metamaterial by using superfine inkjet printer on CuPc-coated Si and demonstrated efficient modulation of the resonant responses of SRR by laser light irradiation. We have also investigated optical modulation of THz transmission of Si coated with four types of π-conjugated materials: two low molecules PCBM and TIPS-pentacene, and two π-conjugated polymer materials MEH-CN-PPV and BBL. Among these materials, PCBM and TIPS-pentacene showed higher modulation efficiencies, even higher than that of CuPc. Utilizing these solution processable π-conjugated materials, various types of THz materials and devices could be fabricated by printing technologies.

Acknowledgements

Author details

Tatsunosuke Matsui[1,2*], Keisuke Takano[3], Makoto Nakajima[3] and Masanori Hangyo[3]

*Address all correspondence to: matsui@elec.mie-u.ac.jp

1 Department of Electrical and Electronic Engineering, Graduate School of Engineering, Mie University, Tsu, Japan

2 The Center of Ultimate Technology on Nano-Electronics, Mie University, Tsu, Japan

3 Institute of Laser Engineering, Osaka University, Suita, Osaka, Japan

References

[1] Tonouchi M. Cutting-edge terahertz technology. Nature Photonics. 2007;1:97–105. doi: 10.1038/nphoton.2007.3

[2] Hangyo M. Development and future prospects of terahertz technology. Japanese Journal of Applied Physics. 2015;54:120101-1–120101-16. doi:10.7567/JJAP.54.120101

[3] Rahm M, Li JS, Padilla WJ. THz wave modulators: a brief review on different modulation techniques. Journal of Infrared, Millimeter, and Terahertz Waves. 2013;34:1–27. doi:10.1007/s10762-012-9946-2

[4] Azad AK, O'Hara JF, Singh R, Chen HT, Taylor AJ. A review of terahertz plasmonics in subwavelength holes on conducting films. IEEE Journal of Selected Topics in Quantum Electronics. 2013;19:8400416. doi:10.1109/JSTQE.2012.2208181

[5] Kitoh Y, Yamashita M, Nagashima T, Hangyo M. Terahertz beam profiler using optical transmission modulation in silicon. Japanese Journal of Applied Physics. 2001;40:L1113–L1115. doi:10.1143/JJAP.40.L1113

[6] Rivas JG, Bolivar PH, Kurz H. Thermal switching of the enhanced transmission of terahertz radiation through subwavelength apertures. Optics Letters. 2004;29:1680–1682. doi:10.1364/OL.29.001680

[7] Hendry E, Garcia-Vidal FJ, Martin-Moreno L, Rivas JG, Bonn M, Hibbins AP, Lockyear MJ. Optical control over surface-plasmon-polariton-assisted THz transmission through a slit aperture. Physical Review Letters. 2008;100:123901-1–123901-4. doi:10.1103/PhysRevLett.100.123901

[8] Okada T, Tanaka K. Photo-designed terahertz devices. Scientific Reports. 2011;1:121-1–121-5. doi:10.1038/srep00121

[9] Chen Q, Jiang Z, Xu GX, Zhang XC. Near-field terahertz imaging with a dynamic aperture. Optics Letters. 2000;25:1122–1124. doi:10.1364/OL.25.001122

[10] Rivas JG, Janke C, Bolivar PH, Kurz H. Transmission of THz radiation through InSb gratings of subwavelength apertures. Optics Express. 2005;13:847–859. doi:10.1364/OPEX.13.000847

[11] Yoo HK, Kang C, Yoon Y, Lee H, Lee JW, Lee K, Kee CS. Organic conjugated material-based broadband terahertz wave modulators. Applied Physics Letters. 2011;99:061108-1–061108-3. doi:10.1063/1.3626591

[12] Yoo HK, Kang C, Lee JW, Yoon Y, Lee H, Lee K, Kee CS. Transmittances of terahertz pulses through organic copper phthalocyanine films on Si under optical carrier excitation. Applied Physics Express. 2012;5:072402-1–072402-3. doi:10.1143/APEX.5.072402

[13] Yoo HK, Lee SG, Kang C, Kee CS, Lee JW. Terahertz modulation on angle-dependent photoexcitation in organic inorganic hybrid structures. Applied Physics Letters. 2013;103:151116-1–151116-3. doi:10.1063/1.4825170

[14] Matsui T, Takagi R, Takano K, Hangyo M. Mechanism of optical terahertz-transmission modulation in an organic/inorganic semiconductor interface and its application to active metamaterials. Optics Letters. 2013;38:4632–4635. doi:10.1364/OL.38.004632

[15] Yen TJ, Padilla WJ, Fang N, Vier DC, Smith DR, Pendry JB, Basov DN, Zhang X. Terahertz magnetic response from artificial materials. Science. 2004;303:1494–1496. doi:10.1126/science.1094025

[16] Padilla WJ, Taylor AJ, Highstrete C, Lee M, Averitt RD. Dynamical electric and magnetic metamaterial response at terahertz frequencies. Physical Review Letters. 2006;96:107401-1–107401-4. doi:10.1103/PhysRevLett.96.107401

[17] Chen HT, Padilla WJ, Zide JMO, Gossard AC, Taylor AJ, Averitt RD. Active terahertz metamaterial devices. Nature. 2006;444:597–600. doi:10.1038/nature05343

[18] Chen HT, O'Hara JF, Azad AK, Taylor AJ, Averitt RD, Shrekenhamer DB, Padilla WJ. Experimental demonstration of frequency-agile terahertz metamaterials. Nature Photonics. 2008;2:295–298. doi:10.1038/nphoton.2008.52

[19] Yoo HK, Yoon Y, Lee K, Kang C, Kee CS, Hwang IW, Lee JW. Highly efficient terahertz wave modulators by photo-excitation of organics/silicon bilayers. Applied Physics Letters. 2014;105:011115-1–011115-5. doi:10.1063/1.4887376

[20] Zhang B, He T, Shen J, Hou Y, Hu Y, Zang M, Chen T, Feng S, Teng F, Qin L. Conjugated polymer-based broadband terahertz wave modulator. Optics Letters. 2014;39:6110–6113. doi:10.1364/OL.39.006110

[21] He T, Zhang B, Shen J, Zang M, Chen T, Hu Y, Hou Y. High-efficiency THz modulator based on phthalocyanine-compound organic films. Applied Physics Letters. 2015;106:053303-1–053303-5. doi:10.1063/1.4907651

[22] Park JM, Sohn IB, Kang C, Kee CS, Hwang IW, Yoo HK, Lee JW. Terahertz modulation using TIPS-pentacene thin films deposited on patterned silicon substrates. Optics Communications. 2016;359:349–352. doi:10.1016/j.optcom.2015.10.008

[23] Zhang B, Lv L, He T, Chen T, Zang M, Zhong L, Wang X, Shen J, Hou Y. Active terahertz device based on optically controlled organometal halide perovskite. Applied Physics Letters. 2015;107:093301-1–093301-4. doi:10.1063/1.4930164

[24] Matsui T, Mori H, Inose Y, Kuromiya S, Takano K, Nakajima M, Hangyo M. Efficient optical terahertz-transmission modulation in solution-processable organic semiconductor thin films on silicon substrate. Japanese Journal of Applied Physics. 2016;55:03DC12-1–03DC12-4. doi:10.7567/JJAP.55.03DC12

[25] Hummelen JC, Knight BW, LePeq F, Wudl F, Yao J, Wilkins CL. Preparation and characterization of fulleroid and methanofullerene derivatives. Journal of Organic Chemistry. 1995;60:532–538. doi:10.1021/jo00108a012

[26] Rispens MT, Meetsma A, Rittberger Brabec RCJ, Sariciftci NS, Hummelen JC. Influence of the solvent on the crystal structure of PCBM and the efficiency of MDMO-PPV:PCBM ‘plastic’ solar cells. Chemical Communications. 2003;17:2116–2118. doi:10.1039/B305988J

[27] Anthopoulos TD, de Leeuw DM, Cantatore E, Setayesh S, Meijer EJ, Tanase C, Hummelen JC, Blom PWM. Organic complementary-like inverters employing methanofullerene-based ambipolar field-effect transistors. Applied Physics Letters. 2004;85:4205–4207. doi:10.1063/1.1812577

[28] Anthony JE, Brooks JS, Eaton DL, Parkin SR. Functionalized Pentacene: improved electronic properties from control of solid-state order. Journal of American Chemical Society. 2001;123:9482–9483. doi:10.1021/ja0162459

[29] Sheraw CD, Jackson TN, Eaton DL, Anthony JE. Functionalized Pentacene active layer organic thin-film transistors. Advanced Materials. 2003;15:2009–2011. doi:10.1002/adma.200305393

[30] Ruderer MA, Wang C, Schaible E, Hexemer A, Xu T, Muller-Buschbaum P. Morphology and optical properties of P3HT:MEH-CN-PPV blend films. Macromolecules. 2013;46:4491–4501. doi:10.1021/ma4006999

[31] Babel A, Jenekhe SA. High electron mobility in ladder polymer field-effect transistors. Journal of American Chemical Society. 2003;125:13656–13657. doi:10.1021/ja0371810

[32] Alam MM, Jenekhe SA. Efficient solar cells from layered nanostructures of donor and acceptor conjugated polymers. Chemistry of Materials. 2004;16:4647–4656. doi:10.1021/cm0497069

[33] Murata K, Matumoto J, Tezuka A, Matsuba Y, Yokoyama H. Super-fine ink-jet printing: toward the minimal manufacturing system. Microsystem Technologies. 2005;12:2–7. doi:10.1007/s00542-005-0023-9

[34] Murata K, Masuda K. Super inkjet printer technology and its properties. E-Print Printable Electronics. 2011;1:108–111.

[35] Takano K, Kawabata T, Hsieh CF, Akiyama K, Miyamaru F, Abe Y, Tokuda Y, Pan RP, Pan CL, Hangyo M. Fabrication of terahertz planar metamaterials using the super-fine ink-jet printer. Applied Physics Express. 2010;3:016701-1–016701-3. doi:10.1143/APEX.3.016701

[36] Takano K, Chiyoda Y, Nishida T, Miyamaru F, Kawabata T, Sasaki H, Takeda MW, Hangyo M. Optical switching of terahertz radiation from meta-atom-loaded photo-conductive antennas. Applied Physics Letters. 2011;99:161114-1–161114-3. doi:10.1063/1.3654156

[37] Grischkowsky D, Keiding S, van Exter M, Fattinger C. Far-infrared time-domain spectroscopy with terahertz beams of dielectrics and semiconductors. Journal of Optical Society of America B. 1990;7:2006–2015. doi:10.1364/JOSAB.7.002006

[38] Hangyo M, Tani M, Nagashima T. Terahertz time-domain spectroscopy of solids: a review. International Journal of Infrared and Millimeter Waves. 2005;26:1661–1690. doi:10.1007/s10762-005-0288-1

[39] Lloyd-Hughes J, Jeon TI. A review of the terahertz conductivity of bulk and nano-materials. International Journal of Infrared and Millimeter Waves. 2012;33:871–925. doi:10.1007/s10762-012-9905-y

[40] Nakato Y, Shioji M, Tsubomura H. Photovoltage and stability of an n-type silicon semiconductor coated with metal or metal-free phthalocyanine thin films in aqueous redox solutions. Journal of Physical Chemistry. 1981;85:1670–1672. doi:10.1021/j150612a014

Design and Fabrication of Printed DNA Droplets Arrangement and Detection Inkjet System

Jian-Chiun Liou

Additional information is available at the end of the chapter

http://dx.doi.org/10.5772/63329

Abstract

This article describes the aims to establish a thermal bubble printhead with simultaneously driving multi-channel for DNA droplet arrangement. It proposed a monolithic CMOS/MEMS system with multi-level output voltage ESD protection system for protected inkjet printhead. High-voltage power, low-voltage logic, and CMOS/MEMS architecture were integrated in inkjet chip. It used bulk micromachining technology (MEMS). On-chip high-voltage electrostatic discharge (HV-ESD), protection design in smart power technology of monolithic inkjet chip is a challenging issue. The nozzle jets interleaving scanning sequence is controlled spatially on the elements to avoid the strong interference with DNA droplets caused by the excitation of the neighbor driven elements. A heating element, disposed on the substrate, includes a conductor loop which does not encompass the heating elements on the substrate. The configuration of the heater jet significantly reduces both electromagnetic and capacitance interference caused by the heating elements. The simulation and experience result have shown in the research. It is reduced nearly half the time compared to the case with traditional scanning sequence. This experiment develops new controlled structure designs of chip for inkjet printheads. A bubble inkjet(TIJ) device is designed, several of the architectures may be adjusted just a small microns to improve and optimize the DNA drop nucleation and generation efficiency. The DNA droplet ejection behavior of the multiplexer inkjet printhead within 60-μm orifice size has been measured beyond 5 kHz operation system, 12 pL capacity of ejected DNA droplet volume.

Keywords: DNA droplets, CMOS/MEMS, addressing

1. Introduction

An intelligence inkjet printhead includes a number of heater and nozzle devices formed on a silicon substrate. For reliable operation of the jet heater in a practical thermal ink-jet printhead chip [1–10], external sources of noise become an extremely important concern. It is desirable that the jet heater be disposed on the chip at a location as close as possible to the channels themselves for a most accurate reading of the actual temperature of the liquid ink just before a given ejector is fired. At the same time, the location of the jet heater must be rigorous designed because an additional requirement of a experiential bubble jet printhead is that the chip be as small as physically possible, yet still contain all the circuits required for valid operation [11–16].
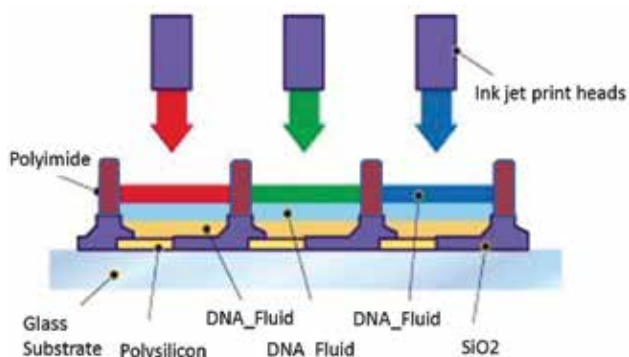
Figure 1. Inkjet printer heads system and multi-channel printhead jets.

The DNA droplet ejection of our addressing N bits jets elements switch multiplexer circuit system printhead has been measured of ejected DNA droplet behavior. There is up to 1024 and even a larger number of elements for a variety of printhead nozzle examinations. The jets interference and the power consumption for such a high-density system, however, make it difficult to achieve a high printing speed, low cost, economic, high-performance, and high-resolution device. In order to alleviate the low noise interference and low-power requirement of jets, a high-voltage driver and logic multiplexer are nowadays employed to match each nozzle of the printhead jet elements and therefore improves the printhead's overall power dissipation. **Figure 1** shows inkjet printer heads system and multi-channel printhead jets using novel encoding algorithm system. Addressing N bits jets elements switch circuit system is using in inkjet chip. Logic functions integrated, enabling TIJ-based products have become increasingly high-end market [17–23]. Inkjet printers can put small number of DNA droplets (usually only a few picoliters, 10–12 l) accurately sprayed on to DNA glasses media. Integrated circuit of the TIJ described transducer array to provide the 1024 ejection jets, includes a data interface, an DNA ink-jet treatment, short-pulse generation, and bidirectional method operation. The chip system also has an output function to manage of multi-chip electronic components into larger arrays. TIJ spray hole array chip design architecture allows less than

10 input lines op addressing 1024 nozzles. **Figure 2** shows printed DNA droplets "AGCT" arrangement and detection.
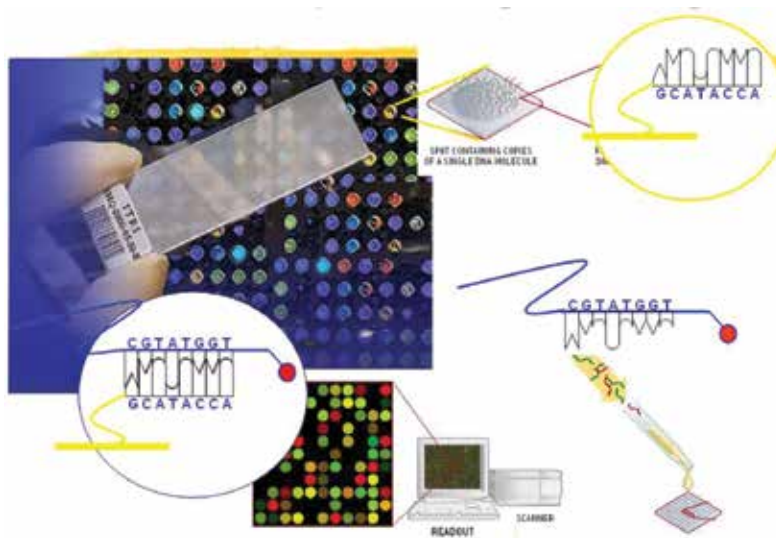

Figure 2. Printed DNA droplets "AGCT" arrangement and detection.

Human birth, old age, sickness and death process, and cellular changes are related to changes in the cell and turn machine in the DNA have been around for a round to be free from the disease, prevent aging dream, universally invested considerable manpower material, and finally solved the mystery of the human DNA code. However, the cause of the test, the correct dosage, and even tailored drugs are dependent on fast, accurate, simple, and inexpensive test technology.

Traditional testing methods, slow and time-consuming, difficult to control the accuracy and cost is very high, limiting the rapid development of biomedical science. Use Biomedical MEMS and microfluidic system technology developed in the biomedical wafer, for DNA sequencing, testing, screening, and development of new drugs, quantitative release of the drug, as well as food, environmental testing and other diseases, to provide a fast, accurate, large, and auto-mation platform. I believe will be able to promote the development of the next stage of biotechnology, provide a degree of contribution.

Biomedical wafer has to do trace detection, quantitative precision, automation, and fast parallel processing, and many other advantages, compared with the traditional biomedical detection, have tremendous advantages, and so far, it has also been a lot of breakthrough technological developments. But it must be said, biomedical wafer also faces many technical challenges, by scientists in different fields need to be overcome. The use of high-density microfluidic device similar to a color inkjet printer's thermal bubble inkjet and other key technologies, each has independent probe of the trace liquid tank, pipeline microfluidics, liquid discharge hole. Trace

Figure 3. Ejection chamber (firing chamber) and cavity geometry shapes.

each liquid tank filling oligonucleotide, after large pieces of DNA probe solution or sugars, can be more than one million droplets ejection.

We use liquid jetting method in addressing the DNA on the slide; it is a precise and rapid deployment of quantitative methods. Generating and physical aspects of the process model simulation of heat dissipated in the growing bubble. It is used thermal bubble nucleation theory (bubble nucleation theory) to simulate the physical mechanism of heat generated by the bubble. It is to discuss ejection chamber (firing chamber) and cavity geometry shapes to reach backfill mechanism of DNA as shown in **Figure 3**. Calculation procedure thermal bubble jet pump decline is a fluid field problem free surface, while the shape of the free surface of the flow field will change with those changes, so to understand the characteristics of injection, must respect the free surface Discussion of issues to be studied.

Numerical simulation of a need to calculate immiscible dominated by the surface tension of the free liquid surface control (free surface). This free surface on both sides and the physical properties of the fluid pressure has discontinuous nature of change; computer simulation program is the key to success lies in tracking the exact location of this discontinuous liquid level.

2. Single channel calculated injection cavity design of the simulation

Computer simulation is the traditional type of single channel for supplying a fluid ejection chamber (firing chamber) simulation. Injection cavity geometry is shown in **Figure 4**. Orifice diameter of 60 μm, the thickness of the orifice sheet is 50 μm, dry film thickness of 60 μm, the bottom area of the injection chamber is 120 μm × 120 μm, the area of the heater was 105 μm × 105 μm. **Figure 5** calculated result is for the injected fluid which is water to 5 kHz operating frequency, and the three-dimensional side view of a two-dimensional cross-sectional view in the XZ 10, 20, 30, 40, and 200 μs injection case.

Computer simulation is still the traditional type in a single passage of the fluid supplied to the injector chamber to simulate. **Figure 6** calculated result is for the injected fluid which is changed to DNA. It is 5 kHz operating frequency, three-dimensional, and three-dimensional side view view at 10, 20, 30, 40, and 200 μs injection scenario. Single-channel injection cavity is not for Z-axis direction completely symmetrical design. It is a droplet drag tail vulnerable asymmetrical flow field forces. It makes the deflection direction of flight. On a three-dimensional view,
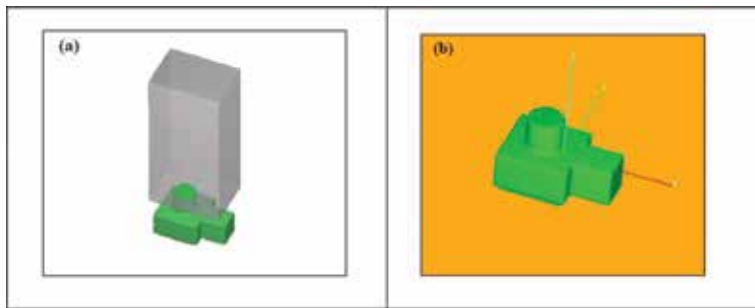
Figure 4. Computer simulation created by (a) calculation of regional, (b) three-dimensional map of the microfluidic single channel.
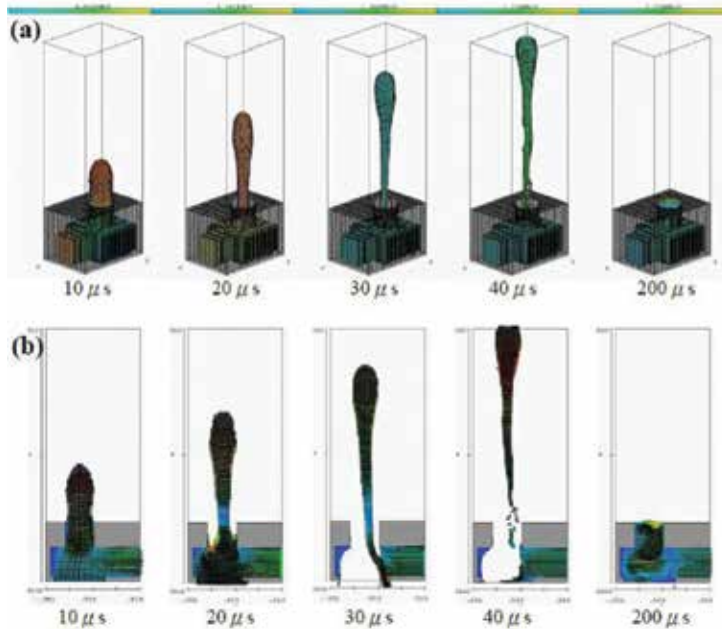

Figure 5. Computer simulation of water in the nozzle diameter 60 μm and 50 μm thickness of a single channel injection cavity, an operating frequency of 5 kHz, in (a) a three-dimensional side view (b) XZ sectional view of a two-dimensional, 10, 20, 30, 40 and 200 μs injection scenario.

it can be seen clearly. The fluid is water or gasoline, because both the geometry of the cavity injection asymmetry makes the tail dragging flight direction deflection. **Figure 7** for the two-dimensional calculation results X–Z sectional view. X–Z sectional view of the results in 200 μs moment, we can see that the liquid level of the fluid, although not yet fully reached the nozzle exit, but DNA is still almost complete backfill. The results also show the geometry of this injection cavity design, operating at a frequency of 5 kHz for, in terms of the DNA is the upper limit of the operating frequency. To further increase, the operating frequency may be less than

the ink supply phenomenon. **Figure 8** is compared with two-dimensional flow field inside the internal cavity of the injection X–Y sectional view of the results. It is the internal flow field vector and water, as shown in below. It is not much difference, showing backfill speed slower than the water.
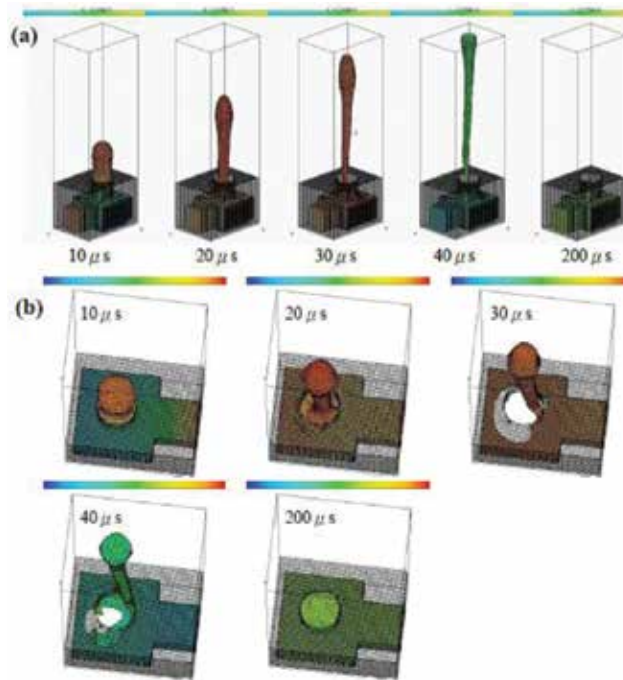

Figure 6. Numerical simulation of DNA in the nozzle diameter 60 μm and 50 μm thickness single-channel injection cavity to 5 kHz operating frequency, to (a) a three-dimensional side view (b) on a three-dimensional view, 10, 20, 30, 40 and 200 μs of injection scenario.
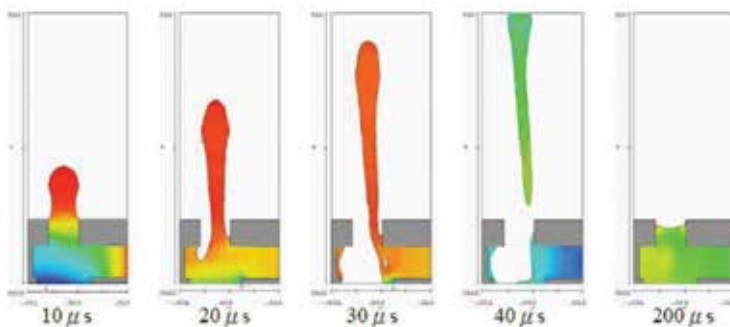

Figure 7. DNA computer simulation in the nozzle diameter 60 μm and 50 μm thickness of a single channel injection cavity to 5 kHz operating frequency, in the two-dimensional X–Z sectional view, at 10, 20, 30, 40 and 200 μs injection scenario.
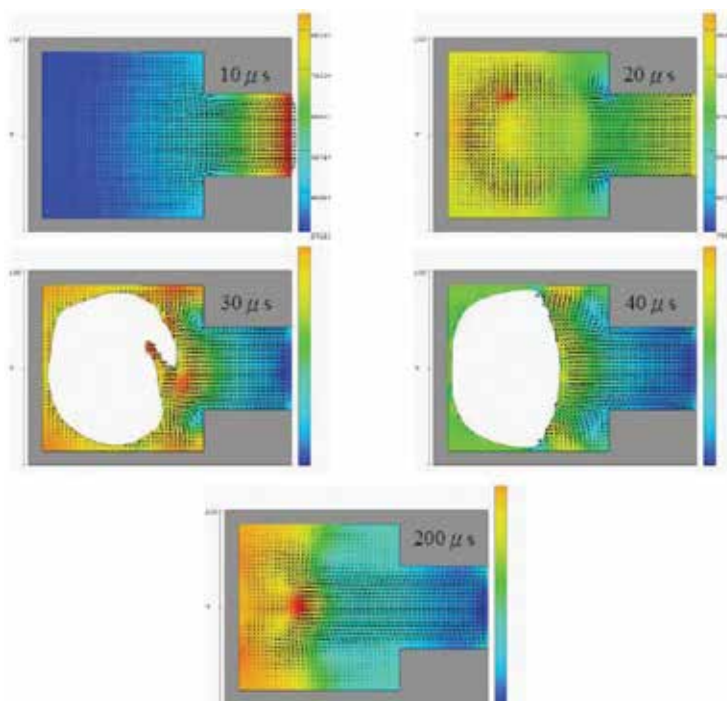
Figure 8. Numerical simulation of DNA in the nozzle diameter 60 μm and 50 μm thickness of the single-aisle jet cavity to 5 kHz operating frequency, the X–Y two-dimensional cross-sectional view, in 10, 20, 30, 40 and 200 μs injection scenario.

It is at the same voltage, the heating time, and other conditions. Because different working fluids (water and DNA), and for the same single injection but may result in different maximum flow. The cause of this problem, there are two possible reasons, the first is due to the poor design of single microfluidic channel, resulting in the flow of work done when the thermal bubble jet DNA monomer heater inlet to the push-back is greater than the flow path to the nozzle holes the launch of the top jet fuel. Thus, causing loss affects a large number of heater acting DNA spray flow. At the same time, due to differences in the physical properties of DNA and water, so that the DNA greater than water leakage, resulting in a smaller flow nozzle exit. Narrowing the channel inlet cross-sectional area is a method you can try, but this method also simultaneously increase the time required for DNA backfilling injection chamber, the mono-mer jet ejection frequency may therefore need to fall. In addition, since the monomer jet DNA to reduce the cooling effect is reduced, so cause DNA monomer generates heat accumulation effect and affect the efficiency of DNA spray, spray a vicious cycle that causes DNA not been apparent efficiency. Another possibility is due to the thermodynamic properties of water and DNA in the table. Temperature, the vertex (critical point) of the magnitude of the pressure is not the same. Even under the same operating conditions of voltage and time of heating, the heat generated bubble internal pressure is not the same size, that is, have different sizes of thrust. Thermal bubble pressure and water produced large thrust, the jet and the flow rate is also larger. In the same function and the same thrust geometric shape of micro-channel design,

the simulation by calculation, preliminary verification can launch jet monomer droplets, the difference volume flow (volume flux) of. Release of DNA volumetric flow rate is relatively low, due to the different physical properties of DNA inference with water, causing DNA to the channel inlet neck (neck channel entrance) the loss is greater than the flow rate of water flow loss. **Figure 9** is the volumetric flow rate of the working fluid through the top of the water and the DNA cross-sectional area of the calculated change with time in figure. This showed that both the volumetric flow rate is not much difference with the total volume of traffic resulting time integration. The inference from the above calculation results under the same operating conditions, hot water bubble pressure, and thrust generated by comparing DNA large, resulting in the ejection of the flow is also larger.
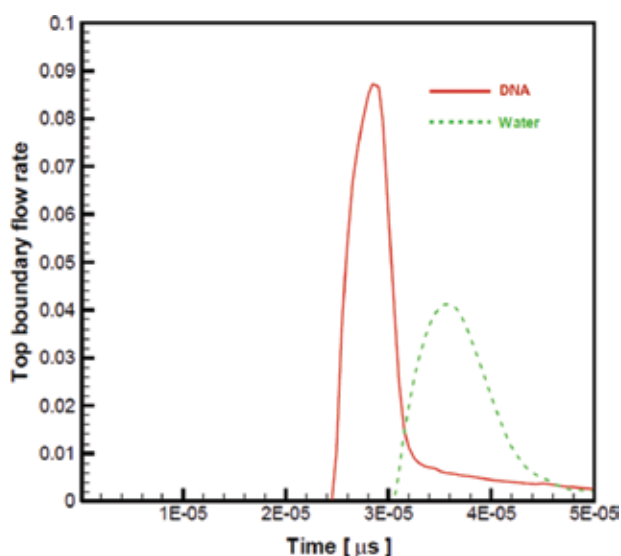

Figure 9. Volumetric flow rate of water through the top and DNA computing sectional area of change with time of the case.

A method for increasing the injection flow rate, in addition to increasing the frequency of injection outside, increasing the ejection orifice diameter of the cavity is also a method to try. But may have other negative effects such as fluid leakage orifice is easy to form puddles (puddling), the need for evaluation by computer simulation verification, in order to determine the negative impact is not the whole jetting performance. **Figure 10** evaluates to the orifice diameters ranging from 60 μm increased to 80 μm, when the injected fluid remains gasoline to 5 kHz ejection frequency, three-dimensional and three-dimensional side view at 10, 20, 30, 40, and 200 μs in the case of injection. With the results shown in **Figure 10**, comparison can be learned in the same circumstances thrust function, because the spray hole diameter increases, so the ejected droplet volume increases. In 40 μs results instantly show droplet flying speed quite significantly reduced. It is produced a relatively large volume of satellites and flying very slowly. **Figure 11** for the two-dimensional calculation results XZ section; at the moment of 40 μs results showed, as exports slow so that the droplet is not out of the nozzle holes with

respect to the results in **Figure 10** for spray when the hole is 60 μm, in an instant 40 μs, the droplet tail is already out of the nozzle holes. **Figure 12** is the result of the calculation of the X–Y two-dimensional section, due to the increase in the spray orifice diameter, relatively large volumes of a spray of droplets. In the cross-sectional area of the flow path, inlet same circumstances take longer to completely fill the internal cavity of the injection orifice until the surface, while the inner flow field to stabilize. Internal flow velocity vector field is still supplying single-channel direction of the fluid toward the discharge chamber in the direction of the moment of 200 μs.
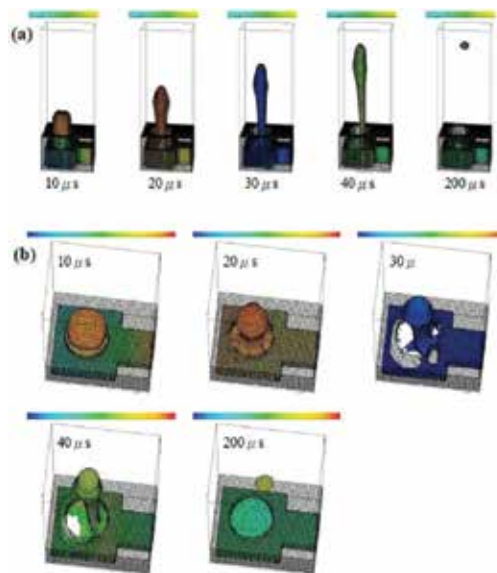

Figure 10. Numerical simulation of DNA in the nozzle diameter 80 μm and 50 μm thickness single-channel injection cavity to 5 kHz operating frequency, to (a) a three-dimensional side view (b) on a three-dimensional view, 10, 20, 30, 40 and 200 μs of injection scenario.
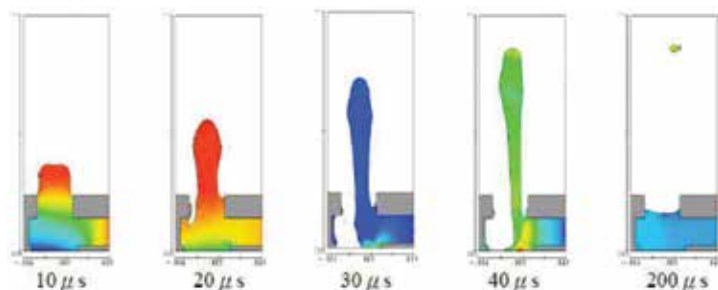

Figure 11. DNA computer simulation in the nozzle diameter 80 μm and 50 μm thickness of a single channel injection cavity to 5 kHz operating frequency, in the two-dimensional X–Z sectional view, at 10, 20, 30, 40 and 200 μs injection scenario.
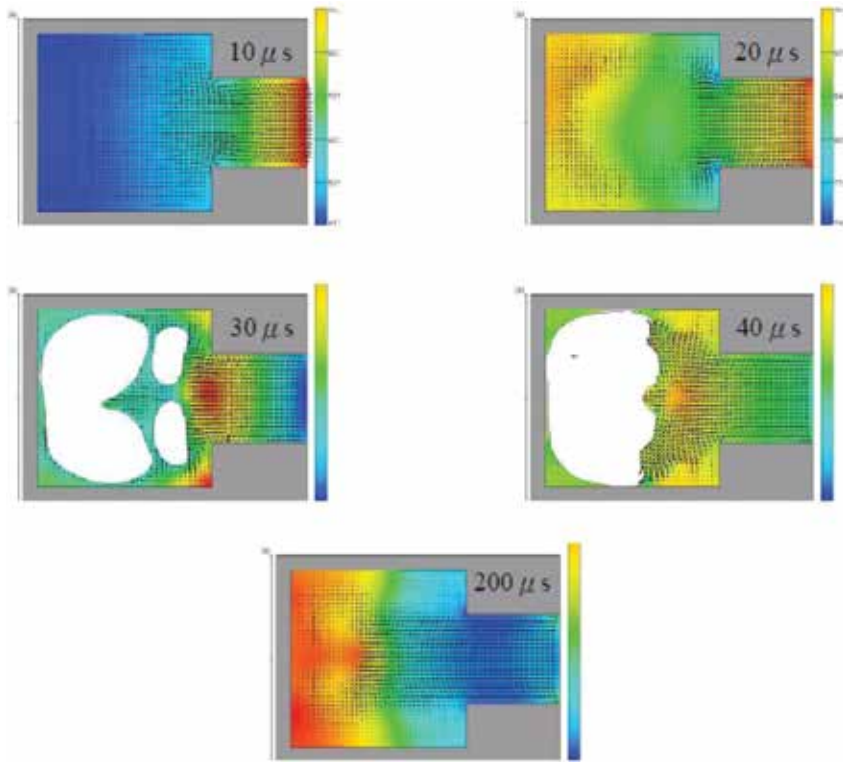
Figure 12. Numerical simulation of DNA in the nozzle diameter 80 μm and 50 μm thickness of the single-aisle jet cavity to 5 kHz operating frequency, the X–Y two-dimensional cross-sectional view, in 10, 20, 30, 40 and 200 μs injection scenario.

Increase the injection flow rate of the other direction of thinking in order to increase the volume inside the cavity injection, in order to that the injected volume of the droplet can be increased, so the study also hope that through computer simulation to verify its feasibility. **Figure 13** for the calculation of simulated gasoline nozzle diameter and 60 μm thickness of 50 μm, dry film (dry film layer) increases the height by 60 μm to 90 μm single-aisle jet chamber, which internal cavity volume 150% increases in operating frequency of 5 kHz, XZ dimensional, three-dimensional side view, and sectional view, in 10, 20, 30, 40, and 200 μs in the case of injection. The result of the calculation shows that the droplet flying speed and directivity of **Figures 3– 12** dry film 60 μm when the height of the result is not much difference, but when 40 μs has been out of the spray droplets hole; but 200 μs instantaneous results show that the fluid has reached the finish filling orifice surface, while the overflow orifice phenomenon is easy to form puddles phenomenon. Therefore, increasing the height of the dry film that is to increase the volume inside the cavity injection, although you can increase the flow rate of backfill raise, it is still possible because the backfill too fast, and out of the orifice puddles formed on the surface of the phenomenon, probably because last fluid left in the orifice surface, so that subsequent ejection of a droplet directionality poor is to increase the dry film thickness may be required to pay attention to the negative effects derived.
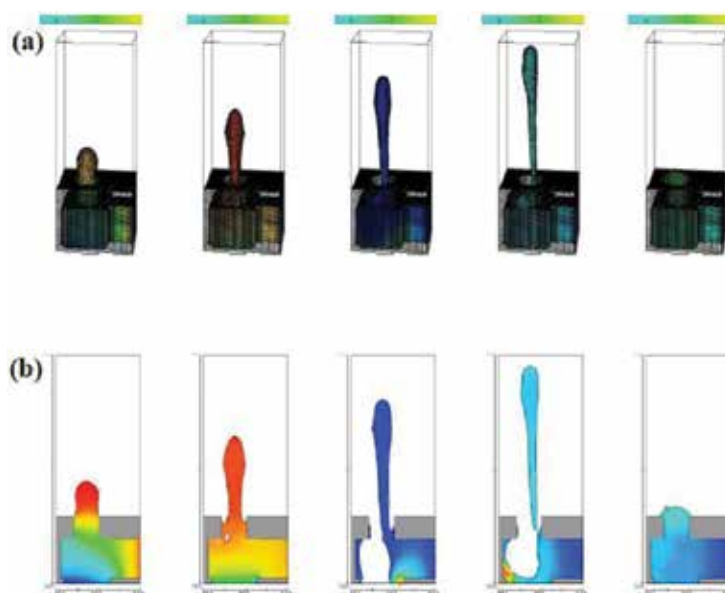
Figure 13. DNA computer simulation in the nozzle diameter 60 μm and a thickness of 50 μm, a height of 90 μm dry film of the single-channel injection cavity, an operating frequency of 5 kHz, in (a) a three-dimensional side view (b) XZ sectional view of a two-dimensional, in 10, 20, 30, 40 and 200 μs injection scenario.

3. Dual-tapered calculated injection cavity design of the simulation

It is an injection operation in various applications nozzle (ink jet head). It is a special micro-fluidic flow channel structure. Backfill fluid injection and two complementary action this period, to be injected fluid within the microfluidic flow path ilk field direction opposite directions. This phenomenon will seriously affect the speed of the fluid backfill supplement and seriously affect the operation frequency of jets. From the simulation result, the system is to solve the problem of liquid flow. It is a dual-type injection cavity design having a fluid passage. At the same time, the fluid has a single-flow direction. It is to reduce the resistance of the fluid, shortening the filling time of the fluid. It is possible to increase the operating frequency of the monomer injection, thereby increasing the maximum injection flow rate.

In this study, it is the geometry and design by microfluidic flow channel. It is a single-direction flow velocity field compared to the entire cycle of backfill fluid flow direction. Therefore, it is to enhance its complement backfill fluid velocity. When the nozzle operating frequency increases, the fluid flow to replenish backfill required for stabilization of fluid ejection chamber fluid level backfill added time will dominate the operating frequency of the jets. Therefore, reducing the time to replenish the fluid needed for backfill will greatly enhance the operating frequency of the jets. Since the droplet ejection but also take away a lot of heat generated by the water heater, a considerable cooling effect reduces the internal temperature of the wafer. So there is also always a considerable improvement in the service life of the wafer. To achieve
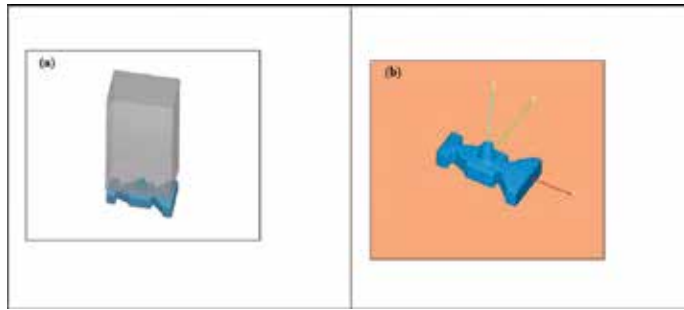
Figure 14. Computer simulation created by (a) calculation of regional scope, (b) a tapered three-dimensional map of the dual-channel microfluidic.

Figure 15. Numerical simulation of DNA in the nozzle diameter 30 μm and 50 μm thickness tapered dual channel injection chamber to 10 kHz operating frequency, three-dimensional side view, in 10, 20, 30, 40, 100, 110, 120, 130, injection of the case 140 and 200 μs.

the above purpose, it is designed to spray a tapered cavity structure of dual-channel microfluidic. **Figure 14** is the three-dimensional microfluidic tapered dual-channel region of a perspective view of the computing range. This type of gradual reduction for dual-channel microfluidic injection chamber numerical simulation conducted to assess the effectiveness of its injection. **Figure 15** for DNA to orifice diameter 30 μm and 50 μm thickness tapered dual-channel injection chamber to 10 kHz operating frequency, three-dimensional side view of 10, 20, 30, 40, 100 110, 120, 130, 140, and 200 μs injection scenario. 110, 120, 130, 140, and 200 μs belong to second injection stage. **Figure 16** is compared to the two-dimensional X–Y sectional view, in the case of injection 10, 20, 30, 40, 100, 110, 120, 130, 140, and 200 μs.
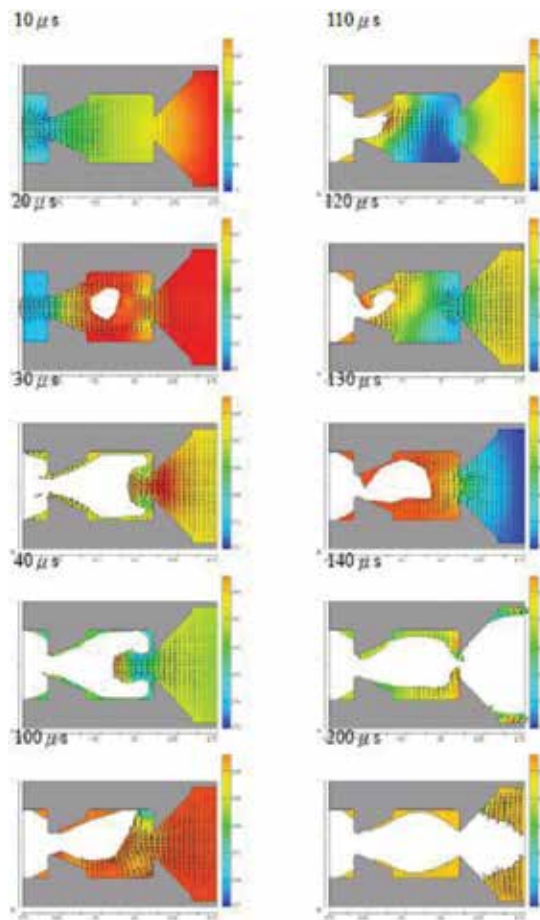
Figure 16. Numerical simulation of DNA in the nozzle diameter 30 μm and 50 μm thickness tapered dual channel injection chamber to 10 kHz operating frequency, the XY two-dimensional cross-sectional view, in 10, 20, 30, 40, 100, 110, 120, injection case 130, and 140 of 200 μs.

The XY two-dimensional cross-sectional view shows that the internal flow field this injection cavity does not have the speed of the flow field in a single direction, so it becomes counter-flow injection of small, but the volume of the second droplet ejection seems to be more for the first time the injection volume is slightly larger. The reason may be due to the tapered microfluidic injection chamber at the start of the two-channel state under stationary conditions. When the first injection, the injection inside the cavity and cannot be achieved immediately single-flow velocity flow field. It requires a certain number of jet action, or the need to increase the flow path style tapered angle, have a chance to achieve a single direction of flow velocity field.

Figure 17 is the result of the calculation of the initial conditions set for the injection inside the cavity has a single-class field direction of situations. DNA double-tapered channel in the injection chamber to 5 kHz operating frequency, three-dimensional and three-dimensional

side view on view at 10, 20, 30, 40 and 50 μs injection scenario. From the results shown that the results of the droplet ejection volume comparing **Figure 16**. There is an increasing convergence of big. Results indicate if the ejection velocity flow field inside the cavity having a single direction of the flow field. It is the ejection of flow convergence increase, while reducing the time required for the fluid filling the cavity of the injection, but also to simultaneously increase the ejection frequency. **Figure 18** is compared with the two-dimensional X–Y sectional view at 10, 20, 30, 40 and 50 μs injection scenario.
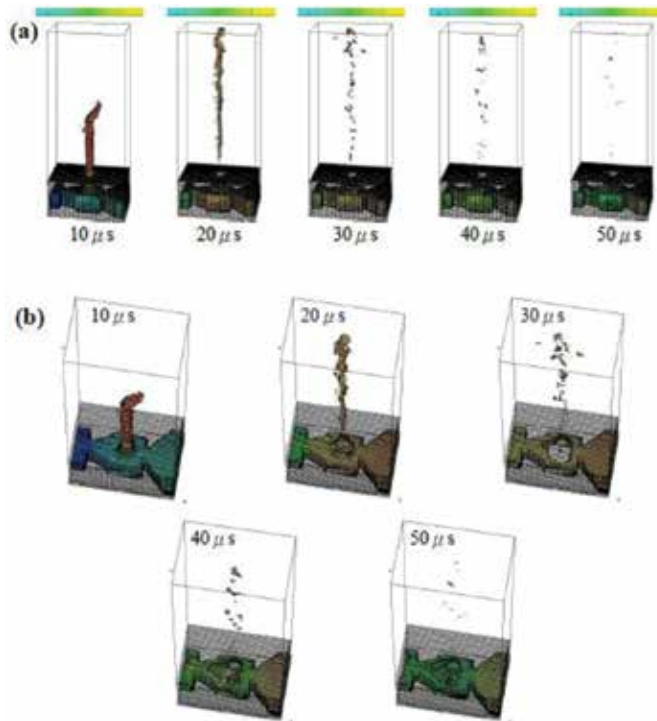

Figure 17. Numerical simulation of DNA in the nozzle diameter 30 μm thickness and tapered dual channel injection cavity 50 μm to 5 kHz operating frequency, to (a) a three-dimensional side view (b) on a three-dimensional view, 10, 20, 30, 40 and 50 μs injection case.

Because of the time course of planning this program, yet there is enough time for this can be tapered dual channel injection chamber, do computer simulation analyzes of various design parameters such as the angle of the tapered flow channel type, respectively to be few degrees preferred design. Application of the heater to produce instant hot bubble of high pressure jet thrust derived monomer. While allowing fluid flow velocity has a single field. Ejection frequency can be increased, and thus get the most traffic. It is currently unable to give details of the desired design dimensions apply to this program the best dual-channel injection tapered cavity to obtain maximum injection efficiency. Continue to be the future of the current simulation analysis to identify micro-injection monomer flow path design can operate at high operating frequencies.
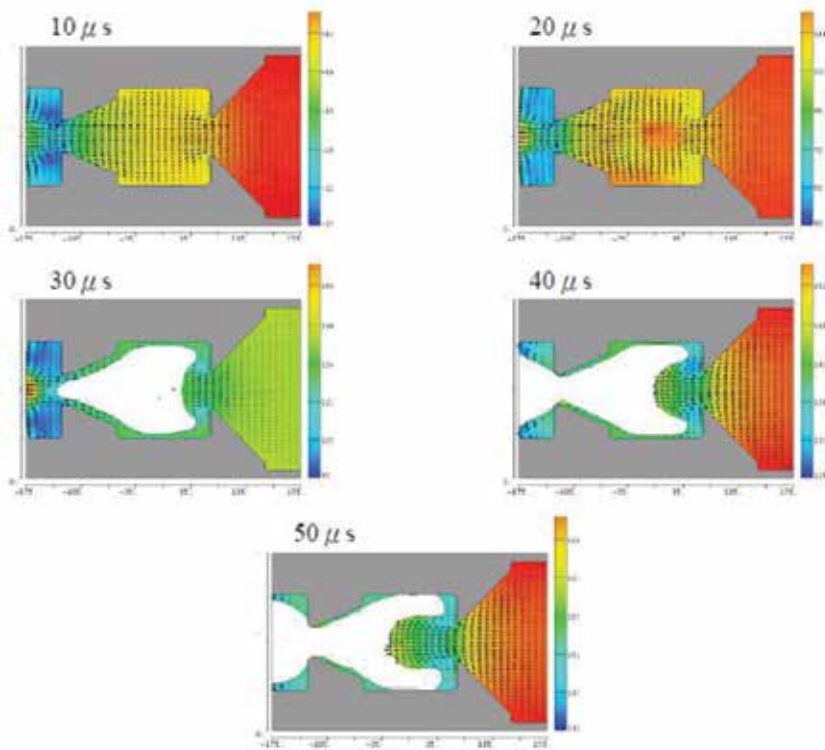
Figure 18. Numerical simulation of DNA in the nozzle diameter 30 μm thickness and tapered dual channel injection cavity 50 μm to 5 kHz operating frequency, the X-Y two-dimensional cross-sectional view, in 10, 20, 30, 40 and 50 μs injection case.

Printing method is the change comes from an inkjet printer, with the heated bubble manner nucleic acid probe is placed on a glass slide using a gene chip production to 30,000 points as shown in **Figure 19**.

Figure 19. DNA droplets profile.

4. Printed DNA droplets arrangement and detection

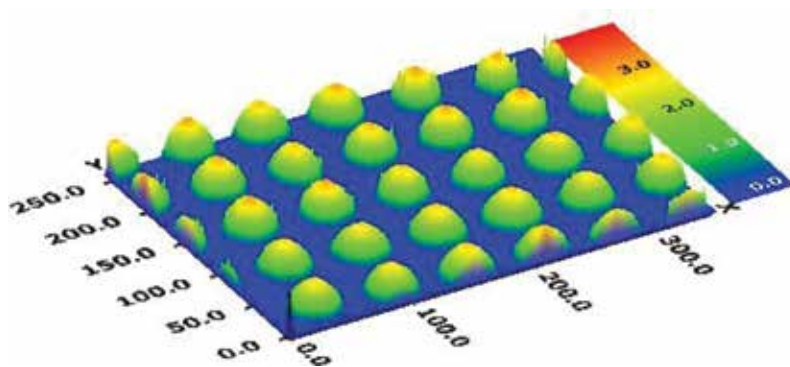Situ synthesis (in situ synthesised), the nucleotide sequence of molecules by using different methodologies to control chemical reactions forming a jieshangqu a nucleic acid sequence, the rapid production of precision (accurate positioning and orientation uniform), ultra-high density (1 million–200 million points) wafer. Synthesis There are two kinds, one is the use of liquid jet technology, such as nucleotide-like ink injected into a specific location subjected to solid phase synthesis (solid phase phosphoramidite chemistry). The whole chip layout is show in **Figure 20**.
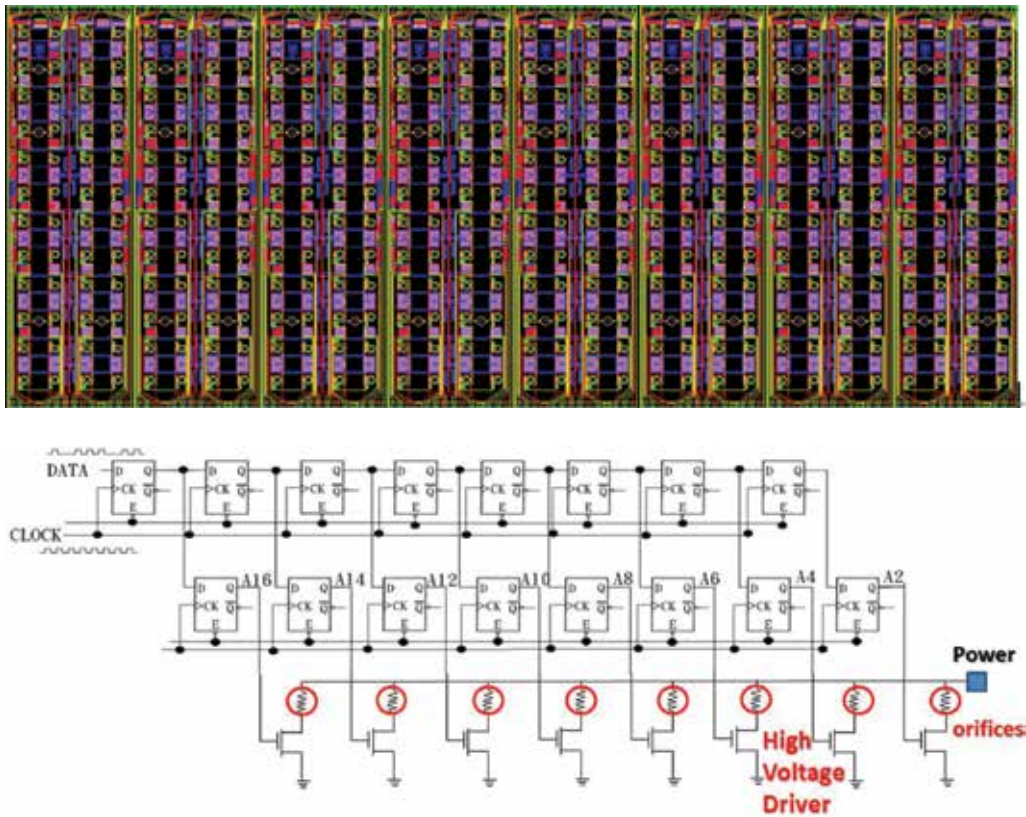
Figure 20. (a) The whole chip layout. (b) The detail circuit(DFF) diagram of chip.

System is to determine a DNA liquid printed head with two hundred orifices, each orifice to orifice distance is another 2000 μm. It is to select the drive mode, respectively, following several ways. The first is the direct voltage direct drive via Pad on the wafer, the drawback is the number of multi-Pad. The second drive element is a driving thin-film resistance element. It is the driving element has a variety of points. It is the n-type metal-oxide half effect transistor factory.

Figure 21. DNA droplet chip and module.

Figure 22. Multiplexer DNA solution jet part.

It is the use of an n-type metal-oxide plant halftime effect transistor to drive a thermal film. It is the thermal resistance of the film due to the long drive 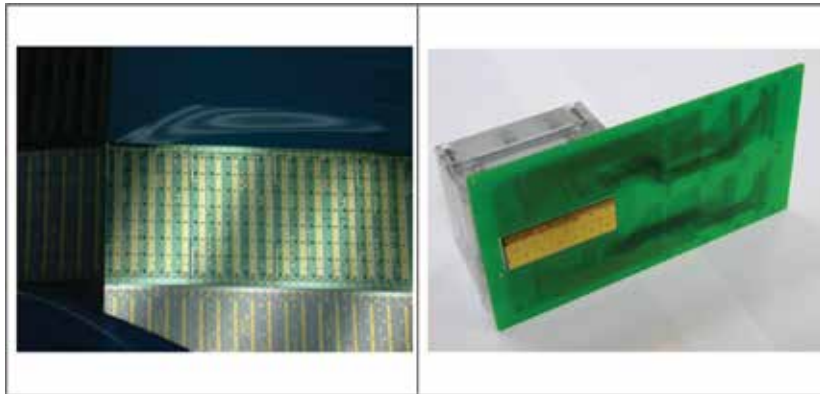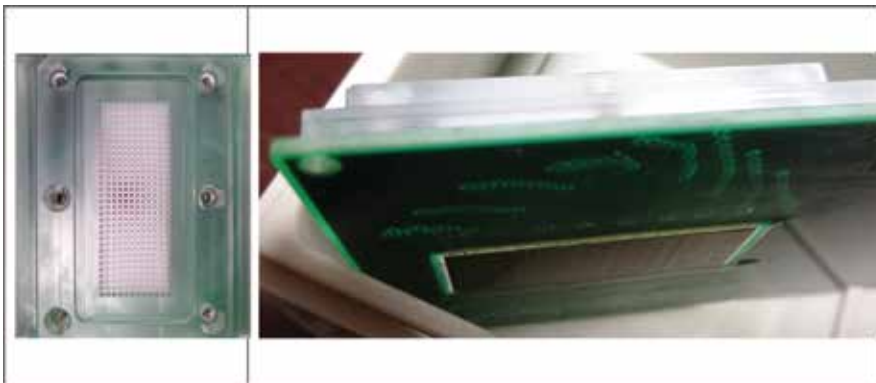driving the heat bubble reagent sprayed onto glass slides. Taking into account the upper and lower symmetrical design of the wafer, so we must first decide with each other and each of the driving elements thin-film resistance elements are arranged. It is the liquid discharge head of the wafer area is very large. We design each wafer map 384 orifices as shown in **Figure 20a**. Our first idea is to spray the wafer to contact aligner way DNA production. The entire wafer is DFF(D-Flip-Flop) data staging operation and high-voltage driver circuit as shown in **Figure 20b**. This circuit can be applied to one or more of the control input signal to change the state, and there will be one or two outputs. Flip-flop is the basic logic unit is configured to sequence logic circuit and a variety of complex digital systems. Flip-flops and latches are essential components used in computer, communications and many other types of systems in the digital electronic systems.

Integrated spray liquid infusion tube sheet and the card brake package as shown in **Figures 21** and **22**. It is the result of a special liquid jet architecture DNA cloth into the slide.

Since microarray dataset wafer has a very large number of the number of genes. It is based on grouping method to automatically discover biological modules (biological modules) is an important theme of the microarray chip analysis. It is a functional grouping (functional Clustering). It is a common occurrence frequency by corresponding functional gene annotations (functional annotation) between (co-occurrences) measurements for clustering. So it can make related genes and annotations easy reach of digital analysis to facilitate the subsequent establishment of the assumptions and experimental design.

The core principles behind the array hybridization between two strands of DNA, the complementary nature of the nucleic acid sequences specifically complementary pair hydrogen bonding between pairs of nucleotide bases to each other through the formation.

Within the liquid jet module integrated HV-ESD Clamp prospective multi-bit output integrated circuit, as shown in **Figure 22**, the DNA gene sequence of printing cards poured into 384 gates, such as nucleotide-like ink injected into specific the position of solid phase synthesis (solid phase phosphoramidite chemistry).
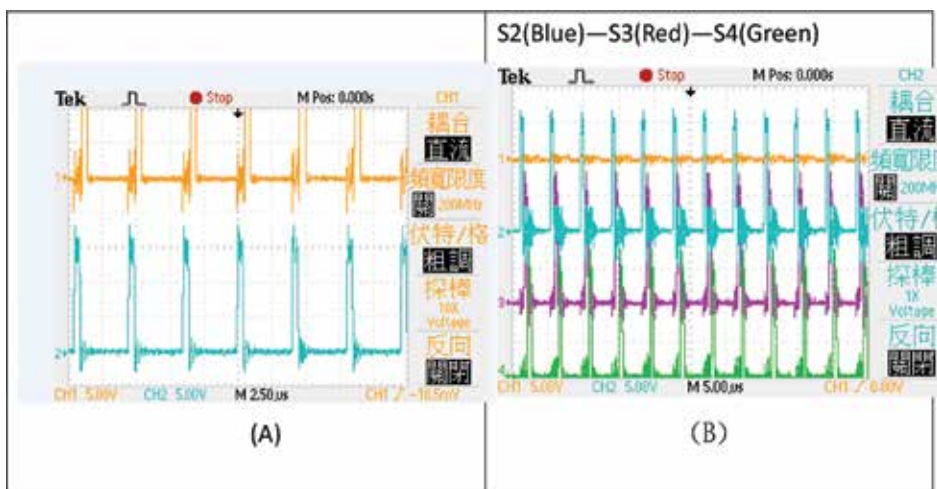
Figure 23. Two sets of data are by the AIP (PIN29) and BIP (PIN30).

The system will be open print dot DNA. It is the use of multi-circuit will print out the orifice of addressing DNA shown in **Figure 23**. There are two sets of data are by the AIP (PIN29) and BIP (PIN30) simultaneously into two 16 bits Register. With instructions sent switch control signal, each generating 384 thermal outputs. CK1 transfer instructions simultaneously send data, CK2 execute instructions simultaneously sending data to the thermal output.

ESD clamp circuit between the power (Power-Rail ESD Clamp Circuit) and inner circuit, when the electrostatic discharge protection device is used in the power supply ESD clamp device, under normal working operation, ESD protection essential element is closed. And the occurrence of electrostatic discharge when the electrostatic discharge protection device must be able

to quickly turn on to ground the electrostatic discharge current, in order to protect the internal circuit purposes as shown in **Figure 24**.

DNA droplets arrangement and detection are observation by high speed cameras. It is by the power supply, light source, liquid discharge frequency and synchronization signals to observe droplet trajectory as shown in **Figure 25**. It is modulated the observation flat-top building to a suitable position, to approve from droplet observation to catch droplet orbit phenomenon. The measurement system could calculate the droplet area、blob length、droplet injection position. **Figure 26** is shown in 5 kHz operating frequency at 30, 40 μs injection.

Figure 27 is printed chip module photo. 50 μm thickness of a single channel injection cavity to 5 kHz operating frequency at 10, 20, 30, 40 μs injection is shown in **Figure 28**.
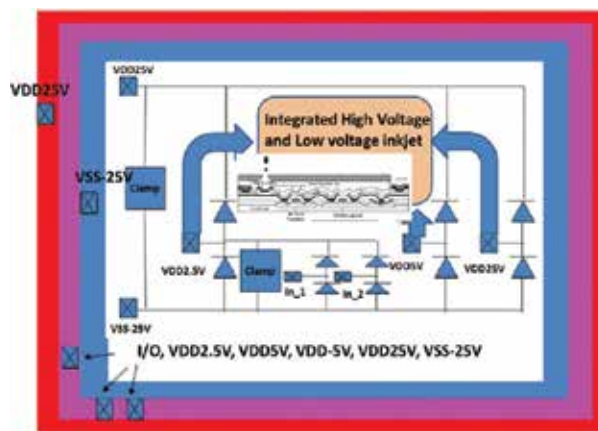

Figure 24. Thermal inkjet(TIJ) printhead with multi-level output voltage ESD protection system.
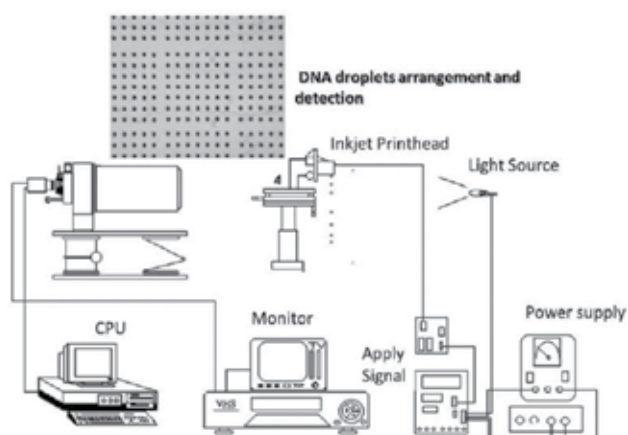
Figure 25. DNA droplets observation platform.
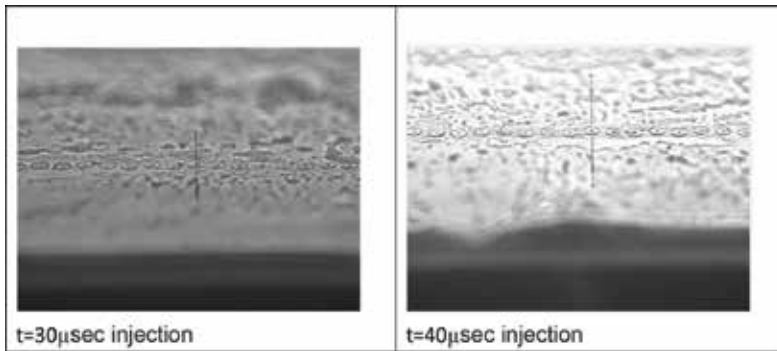
Figure 26. 5 kHz operating frequency at 30, 40 μs injection.
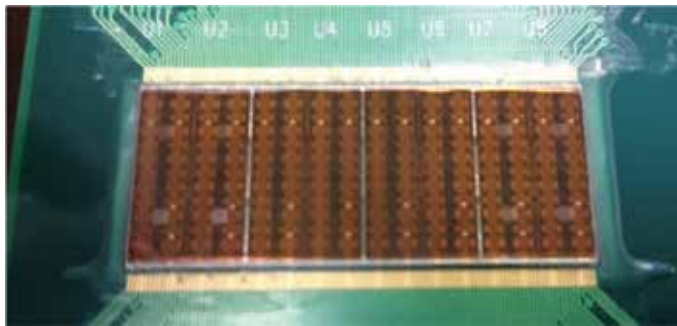
Figure 27. Printed chip module.
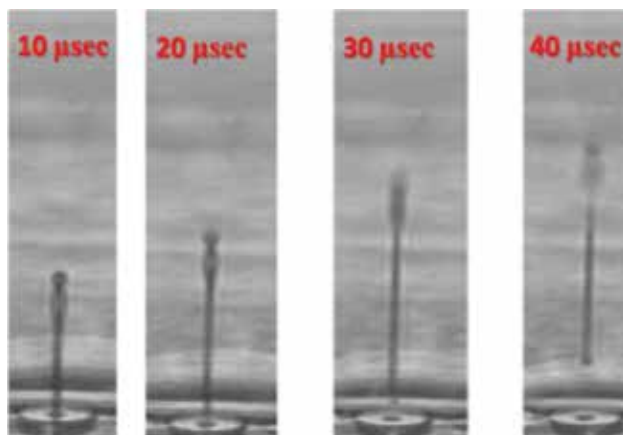
Figure 28. 5 kHz operating frequency at 10, 20, 30, 40 μs injection.

The heated bubble manner nucleic acid probe is placed on a glass slide using a gene chip production to 30,000 points as shown in **Figure 29**. The special printing architecture method is used in system. Among them DNA time interleaving scanning sequence droplets ejection with "even group" jets, DNA droplets ejection with an addressing of two elements on the same time period driving, and DNA droplets ejection with an addressing of three elements on the same time period driving were shown in **Figure 30**. The time interleaving scanning sequence is controlled spatially on the jet elements to avoid the strong interference with DNA droplets caused by the excitation of the neighbor driven elements.
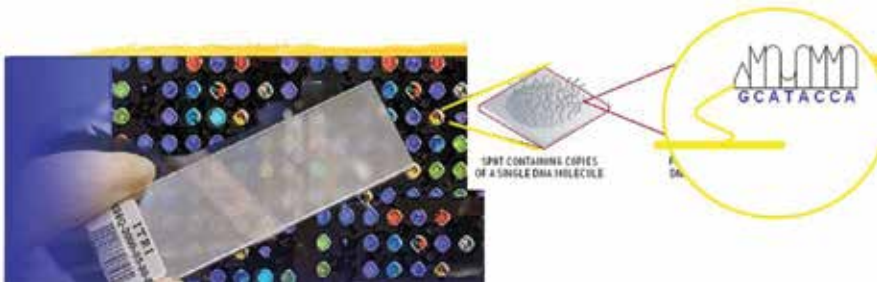
Figure 29. Nucleic acid probe placed on a glass slide.
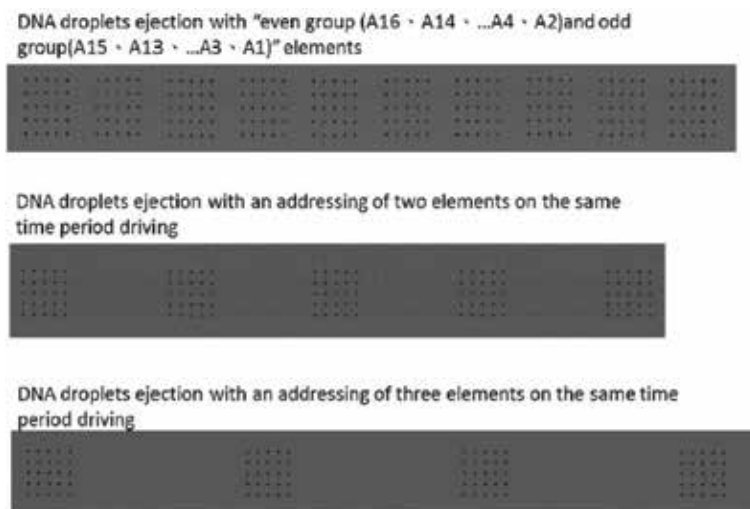
Figure 30. The special printing architecture method.

Acknowledgements

Author details

Jian-Chiun Liou[1,2*]

Address all correspondence to: jcliou@kuas.edu.tw

1 Department of Electronic Engineering, National Kaohsiung University of Applied Sciences (KUAS), Sanmin Dist., Kaohsiung City, Taiwan, R.O.C

2 Graduate Institute of Clinical Medicine, Kaohsiung Medical University, Taiwan, R.O.C

References

[1] Amol A. Khalate, Xavier Bombois, Robert Babuška, Herman Wijshoff, and René Waarsing: Optimization-based feedforward control for a Drop-on-Demand inkjet printhead, American Control Conference (ACC), pp. 2182–2187(2010).

[2] Jian-Chiun Liou, Fan-Gang Tseng: An Intelligent High-Speed 3D Data Registration Integrated Circuit Applied to Large Array Format Inkjet Printhead, NEMS '06. 1st IEEE International Conference on Nano/Micro Engineered and Molecular Systems (Zhuhai), pp. 368–372(2006).

[3] Amol Khalate, Beno Bayon, Xavier Bombois, Gérard Scorletti, and Robert Babuška: Drop-on-demand inkjet printhead performance improvement using robust feedforward control. 50th IEEE Conference on Decision and Control and European Control Conference (CDC-ECC) (Orlando, Florida), pp. 4183–4188(2011).

[4] S. J. Shin, K. Kuk, J. W. Shin, C. S. Lee, Y. S. Oh, and S. O. Park: Firing frequency improvement of back shooting inkjet printhead by thermal management, TRANS-DUCERS. 12th International Conference on Solid-State Sensors, Actuators and Micro-systems (Boston, USA), Volume: 1, pp. 380–383(2003).

[5] Jae-Duk Lee, Choon-Sup Lee, Ki-Chul Chun, and Chul-Hi Han: Two-dimensional nozzle arrangement in a monolithic inkjet printhead for high-resolution and high-speed printing, International Electron Devices Meeting, 1999. IEDM '99. Technical Digest (Washington, DC, USA), pp.127–130(1999).

[6] T. Goldmann and J. S. Gonzalez: DNA-printing: Utilization of a standard inkjet printer for the transfer of nucleic acids to solid supports, J. Biochem. Biophys. Methods, vol. 42, no. 3, pp. 105–110(2000).

[7] R. Teranishi, T. Fujiwara, T. Watanabe, and M. Yoshimura: Direct fabrication of patterned PbS and CdS on organic sheets at ambient temperature by on-site reaction using inkjet printer, Solid State Ion., vol. 151, no. 1–4, pp. 97–103(2002).

[8]   T. Courtney, R.E. Drews, V. I. Hull, D. R. Ims and M.P. O'Horo: Print Element for Xerox Thermal Ink Jet Print Cartridge, in Color Hard Copy AND Graphic Arts III, J. Bares (Editor), Proc. SPIE, Vol. 2171, pp.126–130(1994).

[9]   P.H. Chen, W. C. Chen, and S. H. Chang: Bubble growth and ink ejection process of a thermal ink jet printhead, Int. J. Mech. Sci., vol. 39, no. 6, pp.683–695(1997).

[10] Fan-Gang Tseng, Chang-Jin Kim, and Chih-Ming Ho: A high-resolution high-frequency monolithic top-shooting microinjector free of satellite drops—Part II fabrication, implementation, and characterization, J. of Microelectromech. Syst., vol. 11, no. 5, pp. 437–447(2002).

[11] Fan-Gang Tseng, Chang-Jin Kim, and Chih-Ming Ho, A high-resolution high-frequency monolithic top-shooting microinjector free of satellite drops—Part I: Concept, design, and model, J. Microelectromech. Syst., vol. 11, no. 5, pp. 427–436(2002).

[12] C. T. Pan, J. Shiea, and S. C. Shen: Fabrication of an integrated piezoelectric micro-nebulizer for biochemical sample analysis, J. Micromech. Microeng., vol. 17, no. 3, pp. 659–669, Mar. 2007.

[13] S. C. Tzeng and W. P. Ma: Study of flow and heat transfer characteristics and LIGA fabrication of microspinnerets, J. Micromech. Microeng, vol. 13, no. 5, pp. 670–679(2003).

[14] J.H. Park, and Y.S. Oh: Investigation to minimize heater burnout in thermal thin film print heads, Microsystem Technologies, vol. 11, Berlin: Springer, pp. 16–22(2005).

[15] C. M. Chang, I. D. Yang, R. J. Yu, Y. L. Lin, F. G. Tseng, and C. C. Chieng, Inkjet Printhead Arrays with No Separating Wall Between Bubbles: Solid-State Sensors, Actuators and Microsystems Conference (Lyon), pp. 175–178(2007).

[16] T. G. Kang et al.: A four-bit microinjector using microheater array for adjusting the ejected droplet volume, IEEE JMEMS, vol. 14, pp. 1031–1038(2005).

[17] Sheng-Chih Shen, Min-Wen Wang, and Chung-Jui Lee: Manufacture of an integrated three-dimensional structure nozzle plate using microinjection molding for a 1200-dpi inkjet printhead, J. Microelectromech. Syst., vol. 18, no. 1, pp. 52–63(2009).

[18] F. Takagi, R. Kurosawa, D. Sawaki, S. Kamisuki, M. Takai, K. Ishihara, and M. Atobe: Pico liter dispenser with 128 independent nozzles for high throughput biochip fabrication, 17th IEEE International Conference on Micro Electro Mechanical Systems, 2004. (MEMS) (Netherlands), pp. 276–279(2004).

[19] Ji-Hyuk Lim, Keon-Kuk, Seung-Joo Shin, Seog-Soon Baek, Young-Jae Kim, Jong-Woo Shin, and Yong-Soo Oh: Investigation of reliability problems in thermal inkjet printhead, IEEE International Reliability Physics Symposium Proceedings (Phoenix, Arizolia), pp. 251–254(2004).

[20] T. Lindemann, H. Ashauer, Ying Yu, D.S. Sassano, Roland Zengerle, and P. Koltay: One inch thermal bubble jet printhead with laser structured integrated polyimide nozzle plate, J. Microelectromech. Syst., vol. 16, pp. 420–428(2007).

[21] A. van der Bos, T. Segers, R. Jeurissen, M. van den Berg, H. Reinten, H. Wijshoff, M. Versluis, and D. Lohse: Infrared imaging and acoustic sizing of a bubble inside a micro-electro-mechanical system piezo ink channel, J. Appl. Phys., vol. 110, no. 3, pp. 034503–034503-7(2011).

[22] M. Einat, and M. Grajower: Microboiling Measurements of thermal-inkjet heaters, J. Microelectromech. Syst., vol. 19, no. 2, pp. 391–395(2010).

[23] S.J. Shin, K. Kuk, J.W. Shin, C.S. Lee, Y.S. Oh, and S.O. Park: Firing frequency improvement of back shooting inkjet printhead by thermal management, 12th International Conference on TRANSDUCERS, Solid-State Sensors, Actuators and Microsystems (Boston, USA), Volume: 1, pp.380–383 (2003).

Development Trends in Electronics Printed: Intelligent Textiles Produced with the Use of Printing Techniques on Textile Substrates

Wiesława Urbaniak-Domagała, Ewa Skrzetuska,
Małgorzata Komorowska and Izabella Krucińska

Additional information is available at the end of the chapter

http://dx.doi.org/10.5772/62962

Abstract

The authors concentrated their attention on the new area of research, concerning properties of electrically conductive textiles, produced by printing techniques. Such materials can be used for monitoring, for example, the rhythm of breathing. The aim of this study was to develop a sensor of strains for the needs of wearable electronics. A resistance-type sensor was made on a knitted fabric with shape memory, dedicated to monitor motor activity of human. The Weftloc knitted fabric shows elastic memory—thanks to the presence of elastomeric fibers. The dependence of sensoric properties of the Weftloc knitted fabric on the values of load, its increment rate, and its direction of action was tested. Mechanical parameters including total and elastic strain, elasticity degree, and strength were also assessed. The results indicate an anisotropic character of mechanical and sensoric behaviors of the sensor showing a particularly optimal behavior during diagonal loading. Electro-conductive properties have been imparted to the Weftloc fabric by chemical deposition of polypyrrole dopped with Cl ions. In addition, authors used as a carrier functional water dispersion of carbon nanotubes AquaCyl that was adapted in the Department of Material and Commodity Sciences and Textile Metrology for forming electrically conductive pathways by film printing method. It was assumed that the electrically conductive paths are sensitive to chemical stimuli. Studies of the effectiveness of the sensors for chemical stimuli were conducted for selected pairs of liquids. The best sensory properties were obtained for the methanol vapor—the relative resistance ($R_{rel.}$) at the level above 40%. In the case of nonpolar liquid vapor, the sensoric sensitivity of the printed fabric was much lower, with $R_{rel.}$ level below 29%. Properties of the electrically conductive materials, such as thermal conductivity, electrical conductivity, and resistance to chemicals, allow for widely using them nanotechnology.

1. Introduction

Intelligent textiles, also called active, interactive, and adaptive, become more and more popular, both in scientific area as well as in the companies producing highly specialized clothing and also consumers. Market analysis has shown that there is a strong interest in new textronic materials (smart textiles, e-textiles). The usage of smart textiles brings many possibilities of monitoring the reactions of the human body onto many incentives and factors, as well as their usage as decorations in the public space [1–5].

Intelligent materials have enabled the design and elaboration of a new generation of clothing with integrated sensors and built-in electrodes. The use of biopotential fiber sensors (BFS) allowed miniaturization of ECG sensors. It also granted elimination of the conductive gels, and therefore, the use of new receiving elements was possible. Typical fiber sensor, the registrant biopotential, also acts as a receiver, with electrodes and wire that are connected to the patient. Smart vests have been already used in a limited extent in health monitoring, which enables screening all daily activities. Moreover, they are simple to use and are not causing discomfort while wearing [6]. Fabrics with interleaved weft and knitwear with conductive yarn are widely used. Thus, prepared sensory detectors are sensitive to formability and are used in such areas of life as public safety, police, fire service, medical services and automotive industry [7–9].

Currently, intensive studies are carried out on widening the functions of clothing. Additional functions would consist of warning man about possible danger, monitoring the man's body motoric activity (position, kinematics of body parts) and physiological activities (skin temperature, respiration rate, pulse oximetry, electrocardiogram, electromyogram) [10–12]. In order to provide above functions, it is proposed to use fibrous structures, such as mono- and multi-filaments, or knitted and woven fabrics as elements integrated with clothing, the so-called electronic textiles (e-Textiles). Such type of fibrous structures, under the influence of stimuli, for example mechanical load, electric field, magnetic field, temperature, irradiation, chemical vapors, shows reversing changes in their properties: shape memory [13–16], piezoresistive [17–21], chemo-resistive [22–24], piezo-electrical [25–27], electro-chromic [28, 29], electro-luminescent [30–32] properties, etc. The last decade witnessed the development of e-Textiles prototypes based on functional textile materials: Modular Autonomous Recorder System for measurement of autonomic nervous system activity [33], Clothes for Tele-Assistance in Medicine [34], wearable health care system [35], life shirt (smart shirt for continuous ambulatory monitoring) [36]. A wide review of knowledge and developments in the field of e-Textiles, constructions, materials used and developmental trends has been presented in papers published by Rossi's team [19, 37, 38] and monographs [10, 11].

The monitoring of man's body movement activity is often performed with the use of fibrous materials as sensors of strains. The best results are obtained in the case of fibrous structures which have both elastic memory (e.g. elastomeric fibers) and piezoresistive properties. The elastic memory of elastomeric fibers is determined by their exceptionally high reversing deformability. However, elastomeric fibers being electro-insulating from their nature show the piezoresistive effect that is obtained only after a preliminary modification consisting in imparting electro-conductive properties. This modification is made by applying electro-conductive coatings (doped polypyrrole, polyaniline, polyacetylene), inorganic compounds (silver salts), or mass-doping with electro-conductive particles, for example carbon.

The fibrous structures based on elastomers are often modified with polypyrrole due to its stable physical properties (high resistances to thermal, atmospheric and chemical media) and relatively simple deposition process on the substrate surface [39–41]. Elastomer-polypyrrole systems are used as strain sensors 1D (bandages placed directly on knee or elbow joints) or 2D (shirts worn near body that monitor body movements, local changes in torso, arm etc.). In the second case, the stimuli of sensor integrated with clothing have a multi-directional character; hence, the sensoric properties of the sensor material will be strongly dependent on the direction of load and material structure. There are few studies that consider the effect of both factors on the properties of piezoresistive sensors. Increasingly popular are thick electrochemical sensors, ampherometric, and biosensors made by film printing and ink-jet printing using ink from carbon-derived content, ferrocyanide, by which one can assess the impact of deformation of clothing and monitor physiological functions. The future activities of such sensors will focus on the human body, as well as other health care systems; they will monitor not only soldiers but also other services that require this form of monitoring [15, 19]. In order to print on the textiles, various specific substances are used, for example dyes, various types of polymers, silver, carbon nanotubes, graphite or graphene. These components can also provide other established functions, for example anti-static or antibacterial [9, 42, 43]. Printed electronics produced so far primarily for use as the components of devices (computers, tablets, phones, etc.) currently take an advantage in the textile industry because of the prints on fibrous materials that can act as sensors or electrodes for electrical stimulation of muscles in the components of new functionalized garments [9, 42–46]. In published works, electrical con-ductivity was successfully given to materials by textile printing method [47, 48], but existing solutions are still being developed. The authors in their works concentrated their attention on new areas of research, conferring properties of electrically conductive textiles using printing techniques for monitoring, for example the rhythm of breathing. The major reason to start this kind of investigation was the need for developing reliable, handy health monitoring systems [5, 7, 9]. Non-invasive or minimally invasive physiological monitoring devices are also of great importance for defense purposes and applications for athletes. The integration of sensors and biosensors directly with clothing should be beneficial in the development of health care and monitoring systems of soldiers, as well as other civil servants. The integration of electronics with clothing opens up many possibilities in various fields [9, 42, 43]. The authors used the functional water dispersion of carbon nanotubes AquaCyl as a carrier that was adapted in the Department of Material and Commodity Sciences and Textile Metrology Lodz University of Technology for forming electrically conductive pathways by film printing method. It was

assumed that the resulting electrically conductive paths are susceptible to deformation. Modification of the water dispersion of nanotubes was supposed to result in a composition being bi-functional print—electrically and bacteriostatic, which is extremely important in applications of sensors in medical materials, in contact with the human body. In the present study, attention was focused on assigning specific functionality textiles printing techniques using carbon nanotubes, graphene and polypyrrole. Characteristic properties of the electrically conductive materials, such as thermal conductivity, electrical conductivity and resistance to chemicals, cause that they are widely used in nanotechnology.

2. Materials and methods

Taking into account the preparation of a textile strain sensor, textiles with high elasticity and reversibility of deformations were used. Such conditions are fulfilled by warp knitted fabrics of the Weftloc type. The elastic structure of Weftloc fabrics is formed by a system of elastomeric yarns (**Figure 1**) introduced in the mutually perpendicular directions by the three-needle bar, thanks to which the fabric is characterized by 2D deformability.
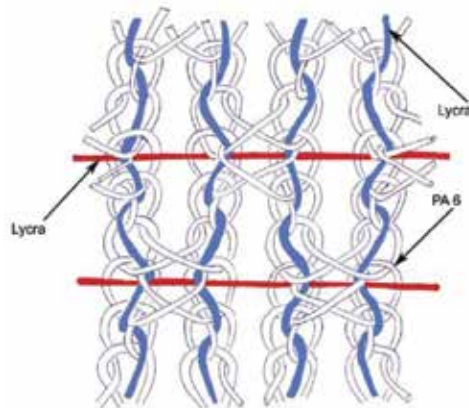
Figure 1. Weftloc PE warp knitted fabric.

Textile substrate	Surface weight,	Thickness	Surface electric resistivity ϱ_S	Raw material composition
	g/m^2	mm	Ωm/m	
knitted fabric Weftloc L (LIBA)	304	0.73 ± 0.01	1.8×10^{13}	PA6 -61% Elastan - 39%
knitted fabric Weftloc PE (PEN ELASTIC)	245	0.52 ± 0.01	6.2×10^{12}	PA6 -64% Lycra - 36%
cotton fabric	206	0.41 ± 0.01	8.7×10^{11}	Cotton-100%

Table 1. Metrological characteristics of textile substrate.

Two Weftloc knitted fabrics with a similar content of elastomeric yarns of different type of elastomer were used, having various surface weights and morphological structures (**Table 1**). Knitted fabrics also contained polyamide yarn that imparts a soft handle and comfort of fabrics in contact with skin. This type of bi-component knitted fabric is exploited in corset-making to make classic lingerie elements fitting to the body, sports and rehabilitation goods.

In addition, cotton fabric twill was also used (**Table 1**) as a reference of the sensitive material for chemical stimulus.

As a base for printing conductive work were used:

• water dispersion of carbon nanotubes trade name AquaCyl (AQ0101) and AquaCyl (AQ0301) from Nanocyl,

• polypyrrole in the form of a water dispersion of nanoparticles prepared in the process of polymerization of pyrrole doped, Sigma-Aldrich,

• flakes of graphene in the form of a dry powder from company Graphene-Supermarket.

Above materials are a well-established in the group of nanomaterials used in consumer printing electronics. The issue of its application is open in order to provide its toxicological safety, in permanent connection with the substrate and ensure the extreme sensitivity of the test stimuli in their minimum content sensory element.

The electrical properties of materials in the study were used by a team of the Department of Materials, Commodity and Textile Metrology Technical University of Lodz [7, 9, 42, 43, 47] to create a conductive printing on transparencies and printing techniques of textile materials.

2.1. Materials

AquaCyl 0101 AQ dispersion comprises from 0.5 to 1.5% MWCNT series Nanocyl®7000 characterized by a purity of approximately 90% with the average diameter of nanotubes 9.5 nm, and the average length of up to approx. 1.5 μm. It is characterized by surface tension approximately 57 N/m, the viscosity of 36 cP and a pH of 7. These parameters were determined in the temperature 25°C. Additionally dispersion comprises a dispersant in an amount of 0.1–3% [7, 9].

Polypyrrole in the form of a water dispersion of nanoparticles produced in the doped poly-merization of pyrrole. Pyrrole is a heterocyclic aromatic compound of the empirical formula C_4H_5N, having a 98% degree of purity. Its density is determined in temperature 25°C, was 0.967 g/mL, and the molecular weight of 67.09 g/mol. Pyrrole applied at the beginning was distilled under reduced pressure.

Graphene flakes in dry powder form under the trade name MO-1, a multilayer graphene flakes having a thickness of 5–30 nm in size with a 5–25 μm [43]. As auxiliaries to modify the water dispersions used: DBSA ($C_{12}H_{25}C_6H_4SO_3H$) solution 70 wt% in isopropanol (analytically pure from Sigma Aldrich) and Ebecryl 2002 (Aliphatic urethane acrylate from Cytec, water com-patible, UV curable system) and Esacure DP250 (water dispersion of photoinitiators from Lamberti SPA).

2.2. Characteristics of inks

The obtained printing paste having the sensory properties based on graphene and carbon nanotubes was introduced to the dispersion AquaCyl AQ0301, 3% by weight of flakes of graphene MO-1. This kind of compiled printing composition was placed in an ultrasonic bath for 15 min. Then, the so-prepared printing composition as well as the dispersion of AquaCyl AQ0101, auxiliary agents in the form of aliphatic urethane acrylate (Ebecryl 2002), and the photoinitiator (Esacure DP250) were added and stirred for 30 min using a magnetic stirrer.

The polypyrrole layer was formed chemically by the in situ polymerization of pyrrole in an aqueous solution of ferric chloride, in which the sample to be coated was immersed. A molar ratio of pyrrole and ferric chloride was 1:2.5. The polymerization was performed at the temperature of 4°C for 2 h. The acidic character of the process medium was maintained by means of an addition of HCl solution. The samples were taken out after 2 h, rinsed repeatedly with distilled water and dried in a desiccator at room temperature.

Knitted fabrics and elastomeric weft yarns used in knitted fabrics were modified under the above given conditions.

2.3. Investigation methods used

2.3.1. Research on electrical resistivity

2.3.1.1. Testing the current-voltage characteristics of textile substrate

The resistance properties of textile substrate were tested before and after coating with electro-conductive polypyrrole, carbon nanotube and graphene. The surface resistance of fabric samples was measured with the use of a two-electrode system and stabilized voltage sources (type 4218 from RTF and type 55121 from Unitra) and a Keithley's electrometer, type 610C. Samples with a width of 2.5 cm were tested under a constant load of 400 kPa, with the inter-electrode distance being 1 cm. The uncoated samples were tested under a voltage of 500 V in a Faraday cage. In case of the samples coated with polypyrrole, carbon nanotube and graphene their current-voltage characteristics were determined within the voltage range from 1 to 20 V, increasing the voltage from smaller to higher values.

2.3.1.2. Testing sample resistance under mechanical load

Changes in the electric resistance of samples were examined simultaneously with sample load using Instron machine, recording the elongation of samples as a function of load F(λ). The changes in load as a result of changing resistance had a dynamic character, which required an automated measuring system.

A sample in the form of a strap, cut out in the assumed direction, was fixed in Instron clamps set up within a distance of 50 mm. The sample in clamps were equipped with elastic electro-conductive electrodes from 3M (R < 1Ω), which provided two-sided contact with the sample.

The electrodes were isolated from the clamp surfaces with a polyester film. Similarly, the samples of elastomeric yarns were fixed.

The electrodes were connected to a multimeter, type Metex KN DMM M-3890DT, coupled with a computer (**Figure 2**). Results in the form of R = f(t) files were sent to computer through USB by means of Metex software.
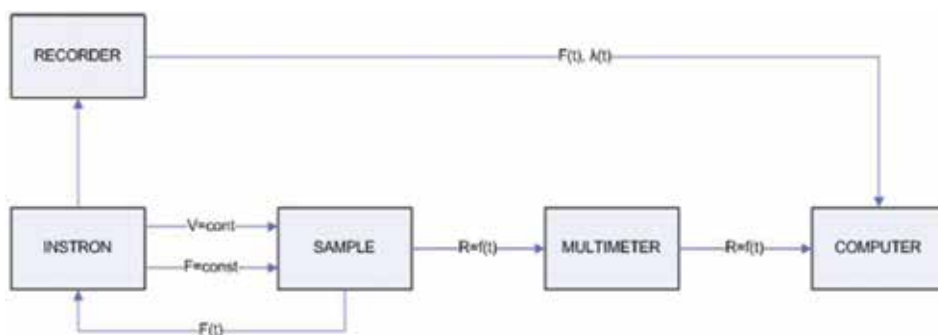

Figure 2. Schematic diagram of the measurement stand for testing the electric resistance of knitted fabrics and elasto‐meric yarn.

The examination of the resistance behavior of samples consisted of recording the changes in resistance in the process of sample loading and relaxing and examining the repeatability of resistance under the given load and a constant frequency of loading.

The resistance sensitivity of the system was calculated according to the formula:

$$Ss = \frac{\Delta R}{R_0 * \varepsilon_{elast}}$$

(1)

where Ss — strain sensitivity, $\Delta R = R_{max} - R_0$, R_{max} — the value of resistance at the point where the sample is loaded with the maximal force F, R_0 — initial value of resistance, ε_{elast} — relative elastic strain, %.

2.3.1.3. Research on electrical resistivity of samples exposed to chemical stimulus

Sensory tests for the presence of solvent vapor were performed in a laboratory measuring system [49]. The equipment allows measurements of the humidity and temperature of the atmosphere prevailing in the system as well as creation and introduction of a system measuring

liquid vapor at a given concentration (**Figure 3**). The measurement technique is described in [43].
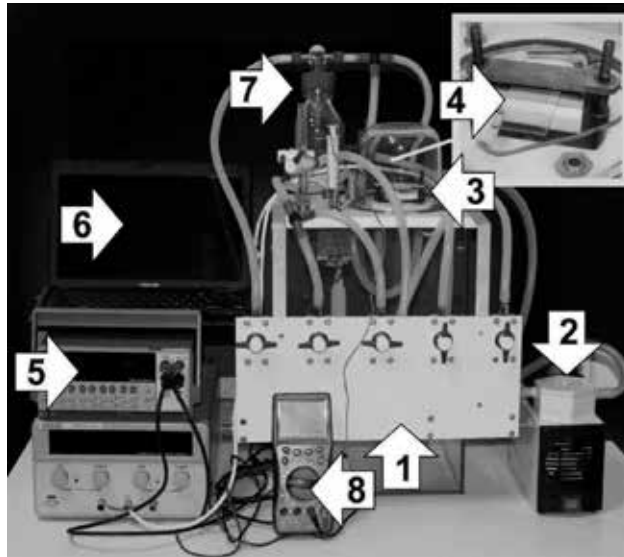

Figure 3. Measuring system for investigating the vapor textile sensors: (1) gaseous chamber with the volume of 0.024 m^3, (2) pump, (3) measurement chamber, (4) measuring electrodes, (5) Keithley multimeter, (6) computer, (7) system ensuring proper humidity of the environment, (8) thermometer [49].

2.3.1.4. Microscopic observations of knitted fabrics

The structure and surface of the tested samples were observed using two microscopic techniques. The morphological structure of yarn and fabrics was examined by the optical microscopy, observing the deformation of fabric structure under the influence of loads. The reflected light microscope coupled with the camera and image analysis system "Lucia" was used for morphological evaluation of tested fabrics.

The surfaces of fibers and knitted fabrics were observed by scanning electron microscopy (SEM), using a JSM-520 LV microscope from Jeol (Japan). The technique of specimen preparation is described in paper [50].

3. Results and discussion

3.1. Morphological properties of deposits conductive layers

Figure 4A–F shows the results of the PPy deposition on the multifilaments forming knitted fabrics, and on knitted fabrics, **Figure 4G–I** shows the results of the deposition of carbon
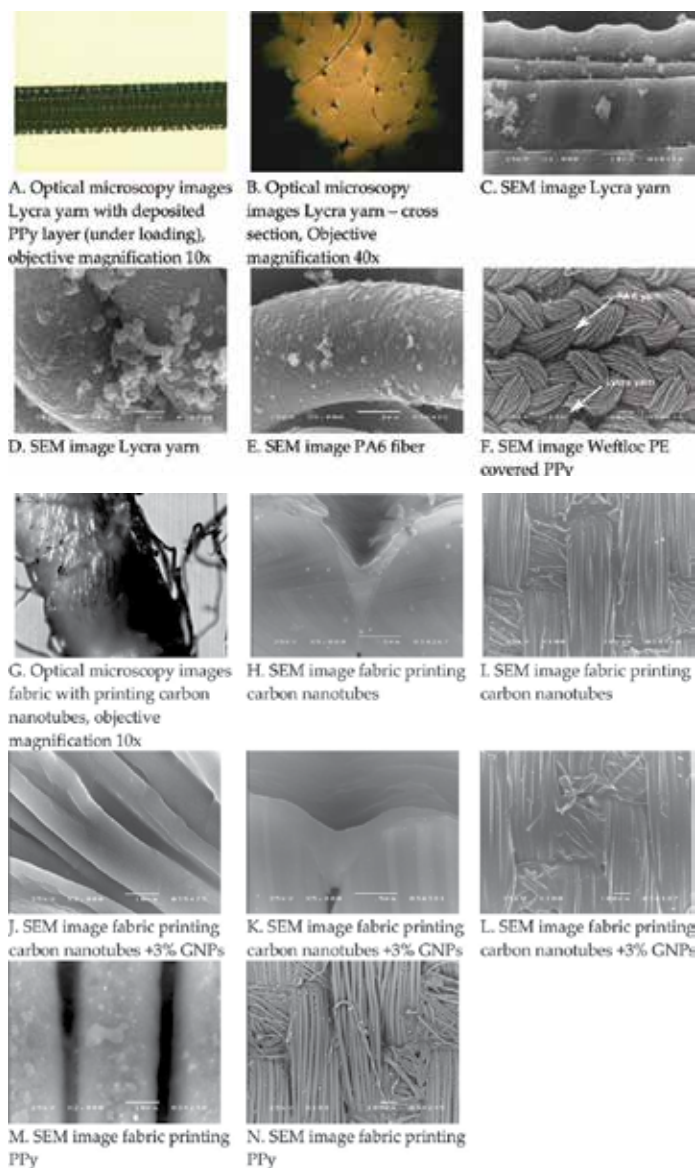
A. Optical microscopy images Lycra yarn with deposited PPy layer (under loading), objective magnification 10x

B. Optical microscopy images Lycra yarn – cross section, Objective magnification 40x

C. SEM image Lycra yarn

D. SEM image Lycra yarn

E. SEM image PA6 fiber

F. SEM image Weftloc PE covered PPy

G. Optical microscopy images fabric with printing carbon nanotubes, objective magnification 10x

H. SEM image fabric printing carbon nanotubes

I. SEM image fabric printing carbon nanotubes

J. SEM image fabric printing carbon nanotubes +3% GNPs

K. SEM image fabric printing carbon nanotubes +3% GNPs

L. SEM image fabric printing carbon nanotubes +3% GNPs

M. SEM image fabric printing PPy

N. SEM image fabric printing PPy

Figure 4. SEM and optical microscopy images of: (A–F) PPy coating on Lycra and PA6 yarns and Weftloc PE knitted fabric, (G–I) AquaCyl AQ3001 + cross-linking compound printed on fabric, (J–L) AquaCyl AQ3001 + 3% GNPs + cross-linking compound printed on fabric, (M–N) Polypyrrole + cross-linking compound printed on fabric.

nanotubes, and **Figure 4J–L** shows the results of the deposition of graphene with carbon nanotubes. The cross-section and longitudinal view of Lycra multifilament (**Figure 4B**, **C**) indicate a strong integration of elastomeric filaments in yarn, which are locally stuck together and deformed at interlacements. In the *in situ* polymerization of pyrrole, PPy layers on both surfaces of the knitted fabrics were formed with the average thickness of 68 nm on Weftloc PE

fabric and 192 nm on Weftloc L fabric. The combination of PPy with the fiber surface in Weftloc knitted fabrics is durable and resistant to washing what was confirmed by appropriate tests. The formed PPy layer consists of PPy micro-spheres with a grain diameter of approximately 1 μm (**Figure 4D**, **E**). **Figure 4B**, **C** indicates a limited penetration across the micro-spheres in the elastomeric multifilament.

Analysis of microscopic images also allowed for determination of the average thickness of the applied layers of ink compositions on fabric, using an image analyzer Luccia. Microscopic examination showed that the thickness of the layer applied to the textile printing technique film contained within 18.5–20.0 μ (**Figure 4H**, **K**). Moreover, analysis of microscopic images shows that the ink compositions are applied in a uniform manner on the textile substrate. Not observed, the resulting thickening of a significant size.

3.2. Electric properties of PPy layers on Weftloc knitted fabrics

The samples of Weftloc knitted fabrics coated with PPy show conductive properties in the electrostatic field. The PPy layer has created conditions for the percolation flow of charge carriers reducing the fabric resistance by about eight orders of magnitude from TrΩ (**Table 1**) to kΩ. The current intensity of the surface conductivity increases proportionally to voltage (**Figure 5**). The above linear behavior with high correlation coefficients ($R^2 \sim 1$) has been found for all knitted fabric samples under conditions of directed action of electric field (in the direction of wales $\varrho_S = 158 \pm 20$ Ωm/m, courses $\varrho_S = 170 \pm 15$ Ωm/m and diagonally $\varrho_S = 160 \pm 30$ Ωm/m). One can state that in the mechanically unloaded condition, PPy layers show isotropic electric conductivity.
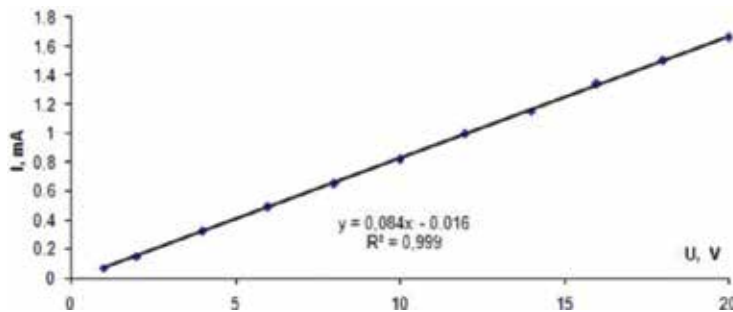
Figure 5. Characteristics of $I_{surface} = f(U)$ of Weftloc PE fabric (diagonal field direction to wales).

3.3. Mechanical properties of elastomeric yarns used in Weftloc fabrics

Weftloc knitted fabrics are characterized by a high content of elastomeric yarn that imparts elastic memory to the material. In order to present the full picture of electro-mechanical properties, both fabrics and elastomeric yarns of these fabrics were tested (100% Lycra and 100% Elastan).

The yarns are characterized by a high degree of elasticity that does not significantly depend on the load value within the range of loads used (up to 0.4 N). However, the relative elastic and total strains strongly increase during load increase (**Figure 6** shows the results for Lycra yarn).

The PPy coating deposited on the fiber surface insignificantly decreases the tensile strength and breaking strain of yarn (**Table 2**). No significant effect of PPy on the degree of yarn elasticity was found (**Table 2**; **Figure 6**).

Type of indicator	Lycra yarn	
	without PPy	with PPy
Degree of elasticity S_{elast}, %	93.6 ± 1.0	94.32 ± 0.9
Elastic strain l_{elast}, %	160.6 ± 4.7	159.1 ± 7.1
Total strain l_{total}, %	171.3 ± 4.6	166.0 ± 8.9
Breaking strain l_{break}, %	574.2	469.3
Tensile force at break F, N	0.85	0.58

Table 2. Effect of PPy on mechanical behavior of Lycra yarn in Weftloc PE (P = 0.4 N).
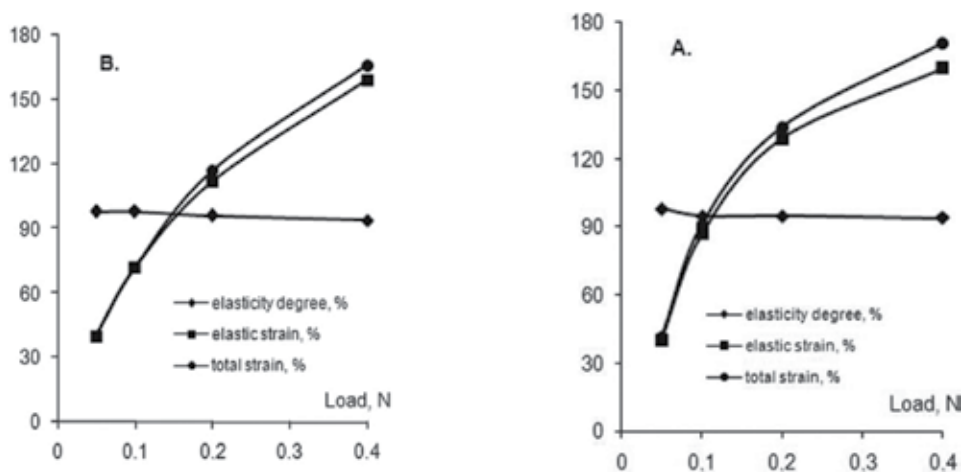
Figure 6. Effect of load on mechanical parameters of Lycra yarn (A) before and (B) after coating with PPy.

3.4. Mechanical properties of Weftloc knitted fabrics

3.4.1. Strength of knitted fabrics

The tensile strength of Weftloc knitted fabrics was tested using forces directed along wales, courses and diagonally. The strength of knitted fabrics without the elastomeric yarn worked-in along courses was also tested to find out how it affects the directional strength at break

(**Table 3**). The removal of the course yarn decreases the directional strength and strain at break. One can assume that the mechanical stability is determined to a large extent by the stitch structure of knitted fabrics.

Type of knitted fabrics	Direction of force	Breaking force, N	Breaking strain, %
Weftloc L	Wales	240.0 ± 2.0	450.0 ± 3.0
	Diagonal	135.0 ± 1.2	482.0 ± 2.5
	Courses	122.5 ± 1.0	607.6 ± 2.6
	Courses, without weft	113.1 ± 1.0	535.7 ± 9.0
Weftloc PE	Wales	161.8 ± 4.0	400.0 ± 1.0
	Diagonal	114.0 ± 1.0	434.5 ± 1.0
	Courses	160.1 ± 4.0	558.1 ± 20.0
	Courses, without weft	116.6 ± 3.0	500.1 ± 8.0

Table 3. Strength parameters of Weftloc knitted fabrics before coating with PPy.

Under the conditions of directional loading, knitted fabrics show the anisotropy of strength and strain (**Table 3**; **Figure 7**). The maximal mechanical parameters are obtained during the course-wise loading. The directional strain of Weftloc PE fabric is, in each case, higher than that of Weftloc L fabric.
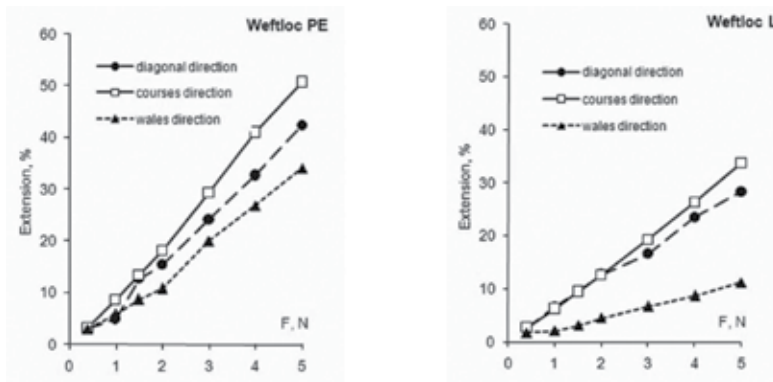

Figure 7. Directional strain of Weftloc fabrics coated with PPy (loading rate: 50 mm/min).

3.4.2. Elasticity of Weftloc fabrics

Weftloc knitted fabrics containing Lycra elastomeric fibers in PEN ELASTIC fabrics are characterized by a higher contribution of elastic strains in comparison with LIBA knitted fabric. The values of elastic strains created during diagonal loading are shown in **Figure 8**. The deposited PPy layer has decreased the elastic strain within the whole load range (0.4–5.0 N).
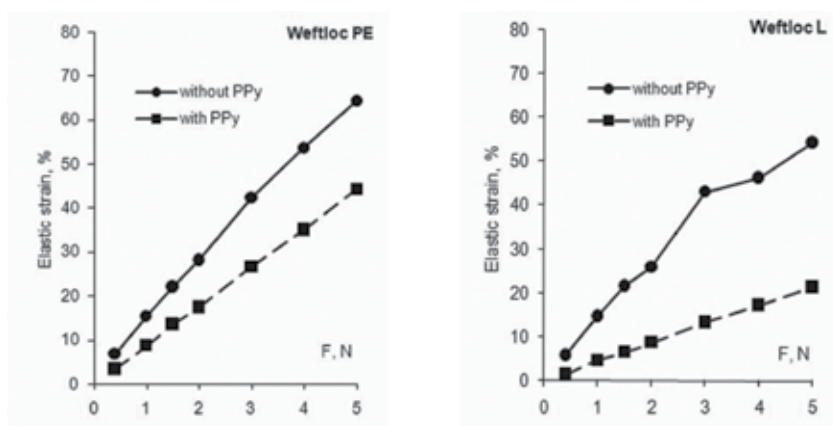
Figure 8. Effect of PPy on the elastic strain of Weftloc knitted fabrics in the diagonal direction (loading rate: 200 mm/min).

3.5. Resistance responses of elastomeric yarns during straining

In order to assess the repeatability of electromechanical behavior of elastomeric yarns, their temporal changes in electric resistance during axial mono- and multi-cyclic tension at a constant rate of load increase in each cycle were examined. **Figure 9A** shows resistance response, R/R_0, (instantaneous values of resistance R of the yarn being loaded in relation to the initial resistance R_0) during the single cycle of tensioning. The resistance increases linearly during the linear load build-up (and the strain proportional to it); after yarn relaxation the resistance returns nonlinearly to the initial condition. The delay in resistance return of the yarn under relaxation indicates processes of stress relaxation in the elastomer. The strain sensitivity Ss of Lycra yarn is at a level of 200. The yarn resistance changes during load build-up are characterized by good repeatability and a high degree of correlation between resistance and strain, which was confirmed also in the multi-cyclic yarn loading (**Figure 9B**).
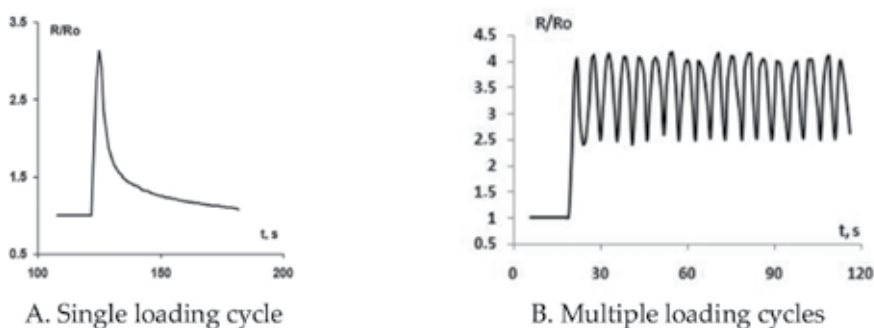

A. Single loading cycle   B. Multiple loading cycles

Figure 9. Resistance responses of Lycra weft yarn tensioned axially, tensioning rate 50 mm/min, load 8cN. (A) Single loading cycle, (B) multiple loading cycles.

3.6. Resistance responses of Weftloc knitted fabrics during straining

The knitted fabrics coated with PPy and directionally strained (**Figures 7** and **8**) show an increase in electric resistance with increasing strain. The value and character of resistance changes depend on the value of load and its build-up rate and direction (resistance anisotropy). In **Table 4**, exemplary resistance responses of PEN ELASTIC knitted fabric loaded in the direction of weft at a loading rate of 50 mm/min are listed. In **Table 4**, **A–D** show relative changes in the electric resistance of a knitted fabric loaded in four single cycles followed by a
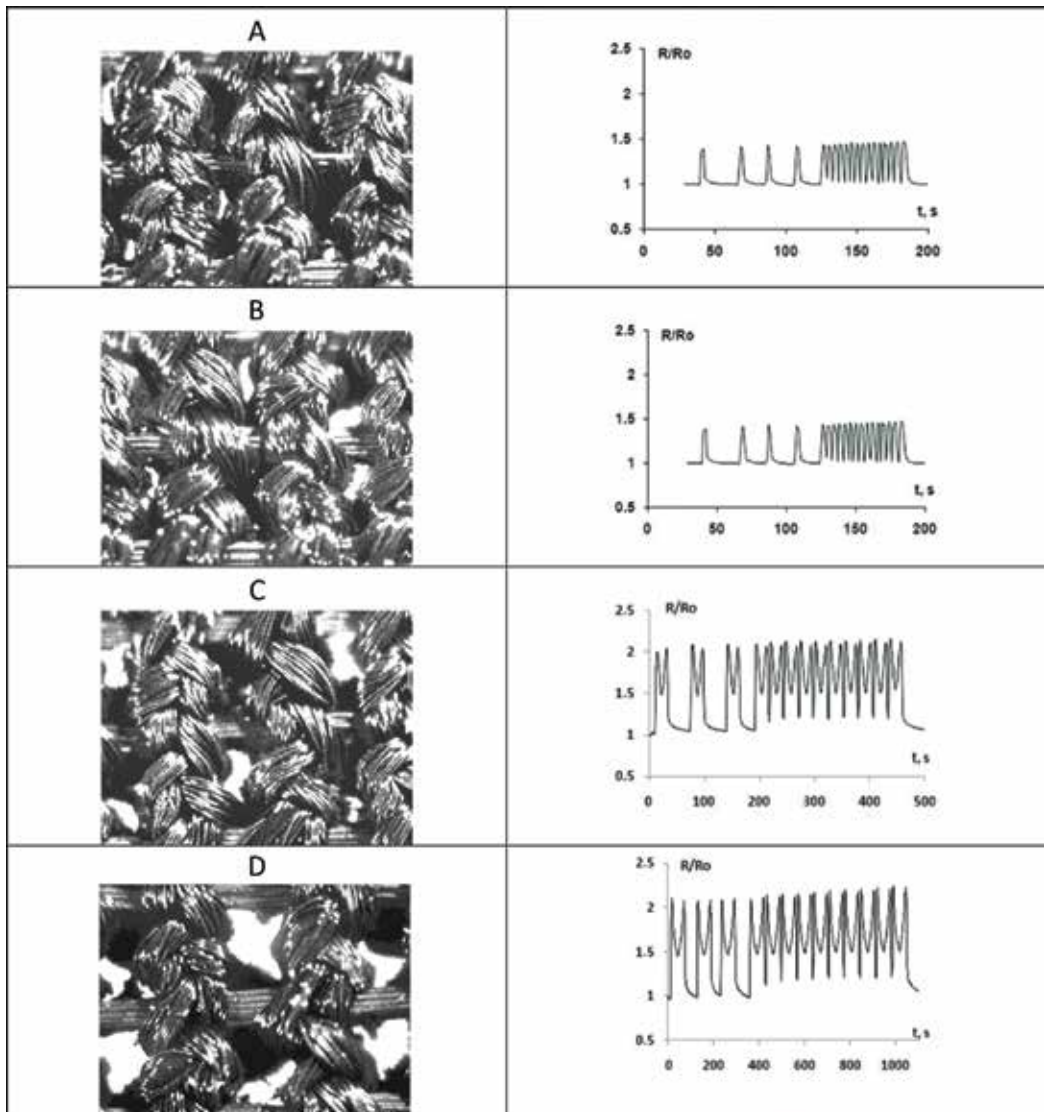

Table 4. Weftloc PE fabric—images during straining and the accompanying changes of fabric surface resistance in loading time (loads: 0.4; 1; 2 and 5 N; loading rate 50 mm/min).

dozen or so cycles succeeding with a higher frequency. In cases A–D, maximal loads were use: 0.4, 1, 2 and 5 N, respectively. The diagrams confirm the repeatability of resistance changes during sample loading in both single and multiple cycles. The resistance increases with increasing sample load. For low loads, the process is of a linear character, while for higher loads, after exceeding about 0.8 N the resistance is decreased ("saddle point"), which may indicate disturbances of charge carrier flow on percolation paths formed by polypyrrole. This effect was found for three loading directions in both knitted fabrics (in the direction of knitting, perpendicular and diagonal directions). This effect is reversible. To illustrate this phenomenon, microscopic simulations of tensioning Weftloc PE loaded in the weft direction at a load rate of 50 mm/min were performed. (**Table 4A–D**). The images show that with the increase in load the distances between wales increase and multifilaments relocate in the knitted fabric loops, which results in the resistance change of mutual contact and consequently in reduced resistance of the knitted fabric. Xue et al. [51] previously indicated the importance of the resistance of fiber contact in knitted fabric loops for the electromechanical properties of knitted fabrics. As far as woven fabrics are concerned, these authors believe that a higher influence on the electromechanical behavior is exerted by the crimp of the weave and density of the fabric. The appearance of the "saddle" phenomenon in the electromechanical response of Weftloc fabrics limits the range of linear behavior of the sensor based on these fabrics.

3.7. Strain sensitivity of Weftloc knitted fabrics

Based on the resistance responses and corresponding strains of Weftloc fabrics loaded successively in three directions: along wales, courses and diagonally, the strain sensitivity (Ss) of these fabrics were calculated. The results of Ss of electro-conductive knitted fabrics are shown in **Figure 10A–C**. The comparison of the behavior of Weftloc fabrics indicates beneficial parameters of the sensor based on Weftloc PE. This fabric, with a similar content of elastomeric yarn and wale density, is characterized by a slightly higher course density (**Table 2**). As far as the metrological parameters are concerned, Weftloc PE is characterized by lower surface weight and thickness, but higher elastic strain in comparison with Weftloc L. The differences in fabric physical parameters have brought different conditions of the PPy micro-sphere diffusion on the fiber surface and in the fabric structure. On Weftloc PE fabric, a thinner PPy layer is formed. During the loading of this fabric, with its higher strain, one could observe considerably greater changes in resistance in comparison with Weftloc L fabric, which resulted in a higher strain sensitivity.
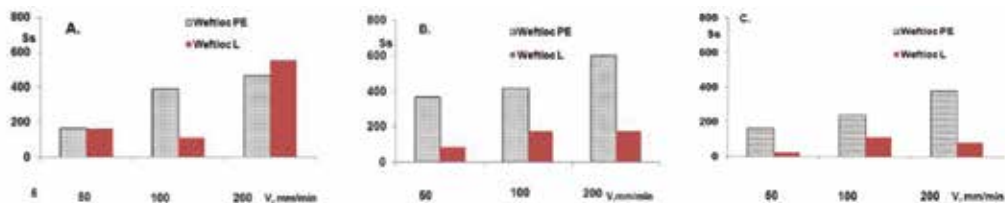

Figure 10. Effect of tensioning rate on the strain sensitivity (Ss) of Weftloc knitted fabrics during loading in the direction of: (A) courses, (B) diagonal, (C) wales.

The sensitivity of both Weftloc fabrics has an anisotropic character. One can assume that it results from the anisotropy of fabric strainability as well as from the anisotropy of the contact resistance of fibers deformed in fabric loops.

The strain sensitivity of Weftloc knitted fabrics increases with the increasing tensioning rate. This behavior results from the fabric strainability and the changes in PPy layer resistance with shortening the loading time, that is increasing the tensioning rate. For both knitted fabrics, it was observed that the increase in load build-up rate was accompanied by twofold reactions: increase in the fabric strainability or unchanged values. The clear increase in the fabric sensitivity with increasing loading rate (**Figure 10**) allows one to state that changes in resistance have a predominant influence of the phenomenon. It has been previously found that the fiber electric resistance considerably increases with increasing rate of loading in the process of drawing PA6 fibers coated with PPy [27].

Based on the results obtained, one can conclude that beneficial operating conditions of the sensor based on Weftloc knitted fabrics can be obtained at higher load build-up rates and short relaxation times. From among the knitted fabrics tested, Weftloc PE shows optimal piezoresistive properties and the best strain sensitivity in the diagonal direction.

3.8. Electrical properties of conducting layers on cotton fabric

The samples of fabrics coated with conductive ink compositions exhibit the electrostatic conductive properties. The conductive layers have created conditions for the percolation flow of charge carriers reducing the fabric resistance by about 10 orders of magnitude from $Tr\Omega$ (**Table 1**) to Ω for ink compositions based on carbon nanotubes **and graphene,** and approximately six orders of magnitude for the ink compositions based on polypyrrole.

The **Table 5** summarizes the results of the electrical conductivity of the printed textile substrates [7, 9, 43].

Composition of ink	Type substrate	Surface electrical resistivity [Ωm/m] (RH = 25%, t = 23°C)	
		Before the washing	After the washing (25 cycles)
AquaCyl AQ3001 + cross-linking compound	cotton fabric	12.0	129.0
AquaCyl AQ3001 + 3% GNPs + cross-linking compound	cotton fabric	4.7	79.0
Polypyrrole + cross-linking compound	cotton fabric	6.6×10^5	8.8×10^6

Table 5. The test results of electric conductivity of the printed textile substrates [7, 9, 43].

Commercial AquaCyl character shows worse electrical conductivity than the prints obtained with addition of graphene. The composition of the print based on polypyrrole results in the weakest conductivity.

In the course of the experiment, there was no significant effect observed on grapheme-based ink properties taking in account the amount of added graphene, uniformity of obtained paste before and after printing.

It has been found that the presence of auxiliary agents in the form of aliphatic urethane acrylate and the photoinitiator has no effect on the properties of the conductive ink compositions tested, but significantly improves the durability of prints.

3.9. Responses resistive printed fabrics treated with chemical stimulus

Table 6 and **Figure 11A–C** summarize the results of testing the functionality of the textile resulting in a film printing technology.

As an indicator of quantitative sensory properties assumed as the relative resistance changes, R_{rel} expressing the relative changes in electrical resistance in the surface of the printed fabrics induced chemical stimulus of a given type, calculated in accordance with the formula (2).

$$R_{rel} = \frac{R - R_o}{R_o} 100\%$$ (2)

where R_{rel}—relative resistance

R_0—initial value of resistance

R—final value of resistance.

Composition of ink	Concentration, ppm	Relative resistance, %		
		Acetone	Methanol	Toluene
AquaCyl AQ3001 + cross-linking compound	200	15	50	13
	300	19	57	18
	400	27	68	25
AquaCyl AQ3001 + 3% GNPs + cross-linking compound	200	27	78	23
	300	31	86	29
	400	36	123	34
Polypyrrole + cross-linking compound	200	15	38	6
	300	19	41	9
	400	21	47	11

Table 6. Results of R_{rel} of liquid vapor to prints obtained from compositions based on graphene and carbon nanotubes on a textile substrate [43].

Analyzing the test results summarized in **Table 6** and **Figure 11**, it can be seen that the addition of 3% graphene improves the sensitivity of the reaction liquid to vapor tested. It was also observed that the superior sensory stimuli properties are characterized by the chemical compositions of the sample printed based on carbon nanotubes. The increased concentration of tested liquid vapors has a significant impact on the response sensitivity of printed textile substrates. Research on sensory sensitivity to the chemical stimuli indicates that printed textiles retain sensitivity to cyclical impact, which is presented at **Figure 12**. Essential, however, is the relaxation time of the sample on exposure to vapors of organic liquids.

The test results of sensory sensitivity of the printed textile substrates, compositions based on polypyrrole on the chemical stimuli in the form of liquid indicates that the sensory response to polar liquids is stronger than non-polar liquids. This is probably related to the presence in the structure of polypyrrole-conjugated bonds that markedly enhanced its polarity.

The examinations show that the change of vapor concentrations varies proportionally to the sensory properties. This phenomenon allows the use of so-printed textiles as sensors measuring the changes in concentrations of the relevant vapors in the surrounding they are located in.

The obtained results indicate the potential possibility of using printing methods designed to production of the textile sensors that will be used as components of protective technical clothing, that is fire services and mining industry.
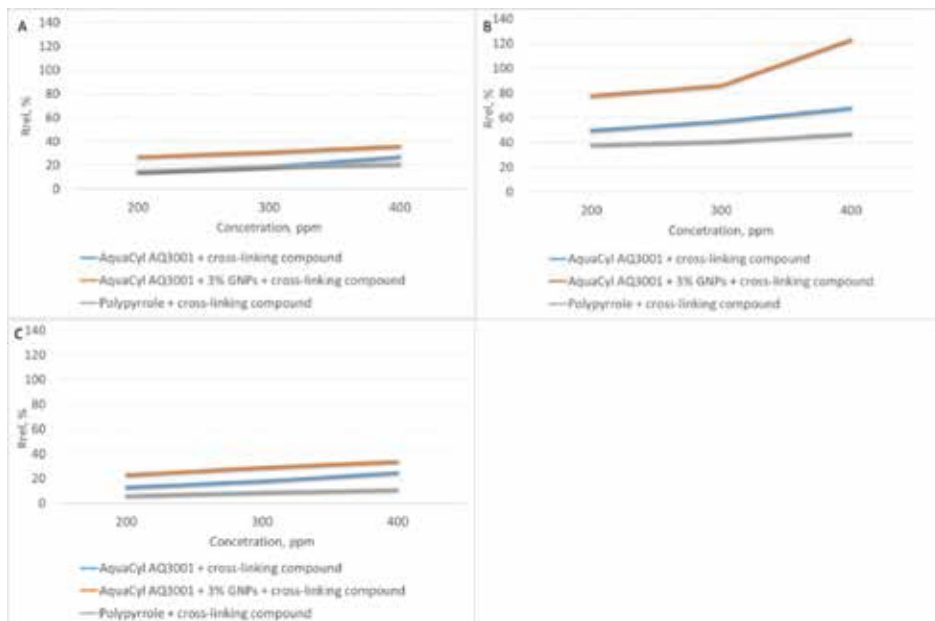

Figure 11. Summary of the sensory properties of the presence of vapor (a) acetone, (b) methanol, (c) toluene.
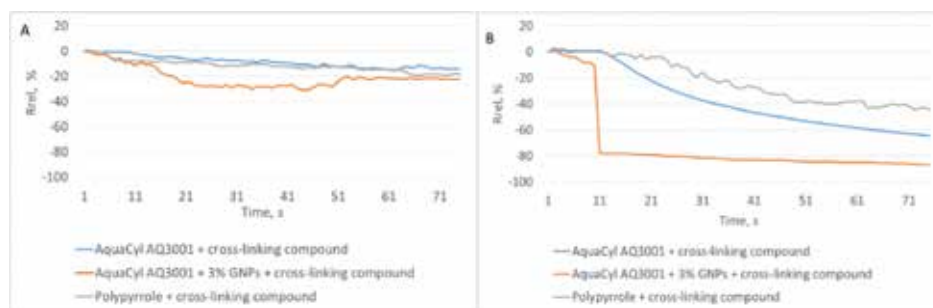
Figure 12. Features of the sensory properties the presence of: (a) the vapor of acetone with a concentration of 200 ppm, (b) methanol vapor at a concentration of 300 ppm.

4. Conclusions

Two Weftloc knitted fabrics from LIBA and PEN ELASTIC companies have been selected as potential strain transducers. These fabrics are characterized by similar raw material composi‐ tion and content: elastomeric fibers and PA6 fibers, while the existing differences concern the type of elastomeric fibers, surface weight of fabrics, their thickness and structure filling degree. The properties of both fabrics are atypical due to the elastomeric yarn introduced additionally in the course direction, which imparts a high strainability 2D to the fabrics. The surface of fabrics has been chemically coated with a layer of electro‐conductive polypyrrole. Thus, Weftloc knitted fabrics as highly strainable and electro‐conductive materials can be used as piezoresistive sensors. The electro‐mechanical tests of Weftloc fabrics prove their high strain sensitivity. The reaction of the fabrics as piezoresistive sensors is of an anisotropic character. For the sake of the construction of strain sensor, it is particularly beneficial to load the piezoresistive element in the diagonal direction in relation to knitting direction. The piezore‐ sistive effects recorded are repeatable during loading Weftloc fabrics in both single and multiple cycles. They have a linear character to a specified limit for the given fabric. Weftloc PE which characterizes specific structure and content of elastomeric yarns has shown a better performance as a piezoresistive sensor.

The studies support the use of ink compositions for modification of textile substrates, as sensors for mechanical and chemical stimulus. By using printing methods for modifying the surface of textiles can be inexpensive and fast way to create RTDs.

Textile sensors presented in the paper have potential application in health care, in the area endangered of chemical explosions, military and sporting applications.

Author details

Wiesława Urbaniak-Domagała, Ewa Skrzetuska*, Małgorzata Komorowska and Izabella Krucińska

*Address all correspondence to: ewa.skrzetuska@p.lodz.pl

Department of Material and Commodity Sciences and Textile Metrology, Lodz University of Technology, Lodz, Poland

References

[1] Atamana, C., Kinkeldeib, T., Mattanaa, G., et al. (2013) A robust platform for textile integrated gas sensors. Sensors and Actuators B, Vol. 177, pp. 1053–1061, ISSN: 0925-4005.

[2] Wei, Y., Torah, R., Yang, K., Beeby, S., Tudor, J. (2013) A screen printable sacrificial fabrication process to realise a cantilever on fabric using a piezoelectric layer to detect motion for wearable applications. Sensors and Actuators A, Vol. 203, pp. 241–248, ISSN: 0924-4247.

[3] Häntzsche, E., Matthes, A., Nocke, A., Cherif, C. (2013) Characteristics of carbon fiber based strain sensors for structural-health monitoring of textile-reinforced thermoplastic composites depending on the textile technological integration process. Sensors and Actuators A, Vol. 203, pp. 189–203, ISSN: 0924-4247.

[4] Paul, G., Torah, R., Beeby, S., Tudor, J. (2015) Novel active electrodes for ECG monitoring on woven textiles fabricated by screen and stencil printing. Sensors and Actuators A, Vol. 221, pp. 60–66, ISSN: 0924-4247.

[5] Yang, K., Freeman, C., Torah, R., Beeby, S., Tudor, J. (2014) Screen printed fabric electrode array for wearable functional electrical stimulation. Sensors and Actuators A, Vol. 213, pp. 108–115, ISSN: 0924-4247.

[6] Yang, Y.L., Chuang, M.C., Lou, S.L., Wang, J. (2010) Thick-film textile-based amperometric sensors and biosensors. Analyst, Vol. 135, pp. 1230–1234, ISSN: 0003-2654

[7] Furtak, N.T., Skrzetuska, E., Krucińska, I. (2013) Development of screen-printed breathing rate sensors. Fibres and Textiles in Eastern Europe, Vol. 21, No. 6(102), pp. 84–88, ISSN: 1230-3666

[8] Zięba, J., Frydrysiak, M. (2006) Textronics-electrical and electronic textiles. Sensors for breathing frequency measurement. Fibres and Textiles in Eastern Europe, Vol. 14, No. 5, pp. 43–48, ISSN: 1230-3666

[9] Krucińska, I., Skrzetuska, E., Urbaniak-Domagała, W. (2012) Prototypes of carbon nanotube-based textile sensors manufactured by the screen printing method. Fibres and Textiles in Eastern Europe, Vol. 20, No. 2, pp. 79–83, ISSN: 1230-3666

[10] Lymberis, A., de Rossi, D. (2004) Wearable eHealth Systems for Personalised Health Management, State of the Art and Future Challenges IOS Press Amsterdam: Netherlands, Vol. 108, ISBN: 978-1-58603-449-8

[11] Tao, X. (2005) Wearable electronics and photonics. The Textile Institute, Woodhead Publishing Ltd: Cambridge, England, ISBN: 1 85573 605 5

[12] Merritt, C.R., Nagle, H.T., Grant, E. (2009) Textile-based capacitive sensors for respiration monitoring. IEEE Sensors Journal, Vol. 9, pp. 71–78, ISSN: 1424-8220

[13] Liu, X., Hu, J., Babu, K.M., Wang, S. (2008) Elasticity and shape memory effect of shape memory fabrics. Textile Research Journal, Vol. 78(12), pp. 1048–1056, ISSN: 0040-5175

[14] Liang, C., Rogers, C.A., Malafeew, E. (1991) Investigation of shape memory polymers and their hybrid composites. Proceedings of Second Joint Japan/US Conference on Adaptive Structures, Nagoya, Japan, November 12–14.

[15] Liem, H., Yrung, L.Y., Hu, J.L. (2007) A prerequisite for the effective transfer of the shape-memory effect to cotton fibres. Smart Materials and Structures, Vol. 16, pp. 748–753, ISSN: 0964-1726

[16] Lendlein, A., Jiang, H., Junger, O., Langer, R. (2005) Light-induced shape memory polymers. Nature, Vol. 434, pp. 879–882, ISSN: 0028-0836

[17] Zhang, H., Tao, X., Wang, S., Yu, T. (2005) Electro-mechanical properties of knitted fabric made from conductive multi-filament yarn under unidirectional extension. Textile Research Journal, Vol. 75/8, pp. 598–606, ISSN: 0040-5175

[18] Leung, M.Y., Tao, M., Cheng, X.Y., Tsang, J., Yuen, M.C.W. (2005) Polpyrrole-coated conductive fabrics as a candidate for strain sensors. Journal of Materials Science, Vol. 40, pp. 4093–4095, ISSN: 0022-2461

[19] De Rossi, D., Della Santa, A., Mazzoldi, A. (1999) Dressware: wearable hardware. Materials Science and Engineering C, Vol. 7, pp.31–35, ISSN: 0928-4931

[20] Spinks, G.M., Zhou, D., Liu, L., Wallace, G.G. (2003) The amounts per cycle of polypyrrole electromechanical actuators. Smart Materials and Structures, Vol. 12, pp. 468–472, ISSN: 0964-1726

[21] Okuzaki, H., Funasaka, K. (2000) Electromechanical properties of a humido sensitive conducting polymer film. Macromolecules, Vol. 33, pp. 8307–8311, ISSN: 0024-9297

[22] Iwaki, T., Covington, J.A., Gardner, J.W. (2009) Identification of different vapours using a single temperature modulated polymer sensor with a novel signal technique. IEEE Sensors Journal, Vol. 9, pp. 314–328, ISSN: 1424-8220

[23] deMelo, C.P., Neto, B.B., de Lima, E.G., de Lira, L.F.B., de Souza, J.E.G. (2005) Use of conducting polypyrrole blends as gas sensors. Sensors and Actuators B, Vol. 109, pp. 348–354, ISSN: 0925-4005

[24] Ruangchuay, L., Sirivat, A., Schwank, J. (2004) Electrical conductivity response of polypyrrole to acetone vapor: effect of dopant anions and interaction mechanisms. Synthetic Metals, Vol. 140, pp. 15–21, ISSN: 0379-6779

[25] Wegener, M., Wirges, W., Gerhard-Multhaupt, R., Dansachmuller, M., Schwodiauer, R., Bauer-Gogonea, S., Bauer, S., Paajanen, M., Minkkinen, H., Raukola, J. (2004) Controlled inflation of voids in cellular polymer ferroelectrets: optimizing electromechanical transducer properties. Applied Physics Letters, Vol. 84, pp. 392–394 ISSN: 0003-6951

[26] Wirges, W., Wegener, M., Voronina, O., Zirkel, L., Gerhard-Multhaupt, R. (2007) Optimized preparation of elastically soft, highly piezoelectric, cellular ferroelectrets from nonvoided poly(ethylene terephthalate) films. Advanced Functional Materials, Vol. 17, pp. 324–329, ISSN: 1616-3028

[27] Wegener, M., Wirges, W., Gerhard-Multhaupt, R. (2005) Piezoelectric polyethylene terephthalate (PETP) foams—specifically designed and prepared ferroelectret films. Advanced Engineering Materials, Vol. 7, pp. 1128–1131, ISSN: 1527-2648

[28] Rossiensky, D.R., Mortimer, R.J. (2001) Electrochromic systems and prospects for devices. Advanced Materials, Vol. 13, pp. 783–793, ISSN: 1527-2648

[29] Argun, A.A.., Aubert, P.H., Thompson, B.C., Schwendeman, I., Gaupp, C.L., Hwang, J., Pinto, N.J., Tanner, D.B., MacDiarmid, A.G., Reynolds, J.R. (2004) Multicolored electrochromism in polymers: structures and devices. Chemistry of Materials, Vol. 16, pp. 4401–4412, ISSN: 0897-4756

[30] Andersson, M.R., Heeger, A.J., Yu, G. (1997) Photoluminescence and electroluminescence of films from soluble PPV-polymers. Synthetic Metals, Vol. 85, pp. 1275–1276, ISSN: 0379-6779

[31] Sutherland, D.G.J., Carlisle, J.A., Elliker, P., Fox, G., Hagler, T.W., Jimenez, I., Lee, H.W., Pakbaz, K., Terminello, L.J., Williams, S.C., Himpsel, F.J., Shuh, D.K., Tong, W.M., Jia, J.J., Callcott, T.A., Ederer, D.L. (1996) Photo-oxidation of electroluminescent polymers studied by core level photoabsorption spectroscopy. Applied Physics Letters, Vol. 68, pp. 2046–2048, ISSN: 0003-6951

[32] Perepichka, D.F., Zperepichka, I.G., Meng, H., Wudl, F. (2005) Light-emitting polymers. Advanced Materials, Vol. 17, pp. 2281–2305, ISSN: 1521-4095

[33] Dittmar, A., Axisa, F., Delhomme, G. (2003) Smart clothes for the monitoring in real time and conditions of physiological, emotional and sensorial reactions of human. 25th Annual International Conference IEEE-EMBS, Cancun, Mexico, September 17–21

[34] VTAMN Project: Bioclothes for ambulatory telemonitoring (Vetement de Teleassistan-ceMedicaleNomade), RNTS 2000, French Ministry of Research and new technologies (France).

[35] WEALTHY Project, http://www.wealthy-ist.com

[36] Vivometrics: LiveShirt System, USA, http://www.vivometrics.com

[37] De Rossi, D., Capri, F., Lorussi, F., Scilingo, E.P., Tognetti, A. (2005) Electroactive fabrics and wearable man-machine interfaces. In: Tao, X., Wearable electronics and photonics, The Textile Institute, Woodhead Publishing Ltd: Cambridge, England, ISBN: 1 85573 605 5

[38] Capri, F., de Rossi, D. (2005) Electroactive polymer-based devices for e-textiles in biomedicine. IEEE Transactions on Information Technology in Medicine, Vol. 9, pp. 295–318, ISSN: 2168-2194

[39] Li, Y., Leung, M.Y., Tao, X.M., Cheng, X.Y., Tsang, J., Yuen, M.C.W. (2005) Polypyrrole-coated conductive fabrics as a candidate for strain sensors. Journal of Materials Science, Vol. 40, pp. 4093–4095, ISSN: 0022-2461

[40] Wu, J., Zhou, D., Too, C.O., Wallace, G.G. (2005) Conducting polymer coated lycra. Synthetic Metals, Vol. 155, pp.698–701, ISSN: 0379-6779

[41] Ohn, K.W., Park, H.J., Kim, S.H. (2003) Stretchable conductive fabric for electrotherapy. Journal of Applied Polymer Science, Vol. 88, pp. 1225–1229, ISSN: 1097-4628

[42] Krucińska, I., Urbaniak-Domagała, W., Skrzetuska, E. (2010) The printing of piezore-sistive sensors on textiles with the use of carbon nanotubes. Sensor devices 2010, Venice-Italy.

[43] Skrzetuska, E., Puchalski, M., Krucińska, I. (2014) Chemically driven printed textile sensors based on graphene and carbon nanotubes. Sensors, Vol. 14, pp. 16816–16828, ISSN: 1424-8220

[44] Krucińska, I., Urbaniak-Domagała, W., Skrzetuska, E. (2011) The use of carbon nanotubes in textile printing. Journal of Applied Polymer Science, Vol. 121, pp. 483–490, ISSN: 1097-4628

[45] Seeberg, T.M., Royset, A., Jahren, S., Strisland, F. (2011) Printed organic conductive polymers thermocouples in textile and smart clothing applications. Engineering in Medicine and Biology Society, EMBC, 2011 Annual International Conference of the IEEE, pp. 3278–3281.

[46] Castro, H.F., Sowade, E., Rocha, J.G., Alpuim, P.A., Machado, V.R., Baumann, R., Lanceros-Méndez, S. (2015) Degradation of all-inkjet-printed organic thin-film transis-tors with TIPS-pentacene under processes applied in textile manufacturing. Organic Electronics, Vol. 22, pp. 12–19, ISSN: 1566-1199

[47] Rogala, M., Własny, I., Dąbrowski, P., et al. (2015) Graphene oxide overprints for flexible and transparent electronics. Applied Physics Letters, Vol. 106(4). doi: 10.1063/1.4906593, 041901, E-ISSN: 1077-3118

[48] Chauraya, A., Whittow, W., Vardaxoglou, C., et al. (2013) Inkjet printed dipole antennas on textiles for wearable communications. IET Microwaves, Antennas and Propagation, Vol. 7, No. 9, pp. 760–776, ISSN: 1350-2417

[49] Skrzetuska, E., Urbaniak-Domagała, W., Lipp-Symonowicz, B., Krucinńska, I. (2012) Giving functional properties to fabrics containing polyester fibres from poly (ethylene terephthalate) with the printing method. Polyester, Dr. Hosam El-Din Saleh (Ed.), ISBN: 978-953-51-0770-5, InTech.

[50] Wrzosek, H. (2000) The use of digital technique in mapping and interpreting electron microscope images of fibres and other polymer objects. Proceedings of Conference IMTEX 2000, łódz, Poland, pp. 293–301

[51] Xue, P., Tao, X., Leung, M.Y., Zhang, H. (2005) Electromechanical properties of conductive fibres, yarn and fabrics. In: Tao, X., Wearable electronics and photonics. The Textile Institute, Woodhead Publishing Ltd: Cambridge, England, pp. 81–104, ISBN: 1 85573 605 5
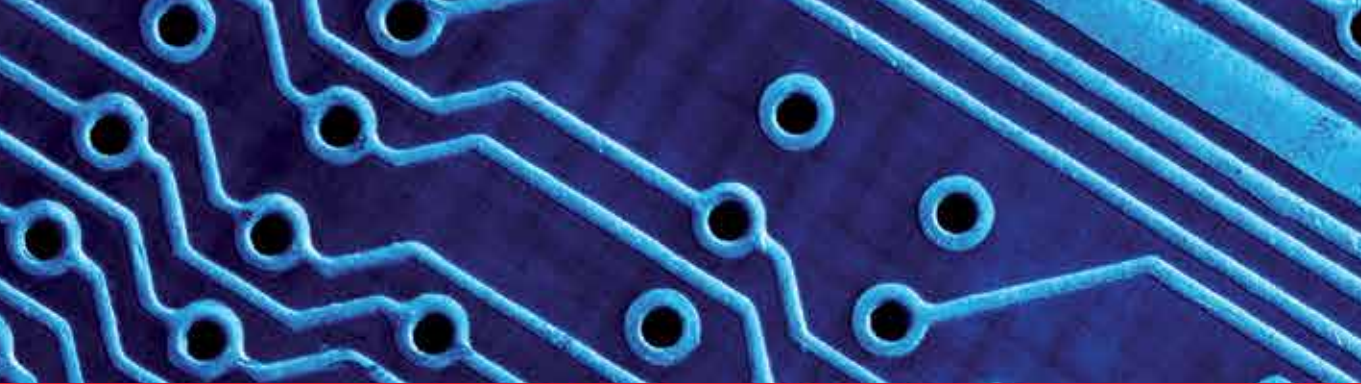
Edited by Ilgu Yun

This book contains a collection of latest research developments on the printed electronics from the material-related various processes to the interdisciplinary device applications. It is a promising new research area that has received a lot of highlights for low-cost and high-volume manufacturing in recent years. Here, you will find interesting reports on currently progressed science- and technology-related materials, fabrication processes, and various recent applications, including organic/inorganic semiconductor, textile, and biomedical engineering for the printed electronics. I hope that the book will provide the fundamental backgrounds of printed electronics to lead you for the creation of new research field and further promotion of future technology of the printed electronics.

IntechOpen